THESIS

INVESTIGATION ON THE STRUCTURAL, MECHANICAL AND OPTICAL PROPERTIES OF AMORPHOUS OXIDE THIN FILMS FOR GRAVITATIONAL WAVE DETECTORS

Submitted by

Samuel Castro Lucas

Department of Electrical and Computer Engineering

In partial fulfillment of the requirements

For the Degree of Master of Science

Colorado State University

Fort Collins, Colorado

Spring 2024

Master's Committee:

Advisor: Carmen Menoni

Jorge Rocca
Justin Sambur

ABSTRACT

INVESTIGATION ON THE STRUCTURAL, MECHANICAL AND OPTICAL PROPERTIES OF AMORPHOUS OXIDE THIN FILMS FOR GRAVITATIONAL WAVE DETECTORS

Amorphous oxide thin films grown through physical vapor deposition methods like ion beam sputtering, play a crucial role in optical interference coatings for high finesse optical cavities, such as those used in gravitational wave detectors. The stability of these atomically disordered solids is significantly influenced by both deposition conditions and composition. Consequently, these enable the tuning of structural, mechanical, or optical properties.

The sensitivity of current gravitational wave interferometric detectors at the frequency range of around 100 Hz is currently limited by a combination of quantum and coating thermal noise (CTN). CTN is associated with thermally driven random displacement fluctuations in the high reflectance amorphous oxide coatings of the end-test masses in the interferometer. These fluctuations cause internal friction, acting as an anelastic relaxation mechanism by dissipating elastic energy. The dissipated internal elastic energy can be quantified through the mechanical loss angle (Q^{-1}). These unwanted fluctuations associated with mechanical loss can be reduced through modifications of the atomic network in the amorphous oxides. Specifically, the combination of two or more metal cations in a mixed amorphous thin film and post-deposition annealing are known to favorably impact the network organization and hence reduce internal friction.

The first study of this thesis reports on the structural modifications between amorphous TiO_2 with GeO_2 and with SiO_2. High-index materials for gravitational wave detectors such as amorphous TiO_2:GeO_2 (44% Ti), have been found to exhibit low mechanical loss post-annealing at 600°C. Reaffirming annealing to be a major contributor to reducing mechanical loss this thesis

examines: a) cation interdiffusion between amorphous oxides of TiO_2 with GeO_2 and with SiO_2 and b) the modifications to the structural properties, both after annealing. The annealing temperature, at which this interdiffusion mechanism occurs, is key for pinpointing structural rearrangements that are favorable for reducing internal friction. Furthermore, to determine whether diffusion occurs into SiO_2 after annealing is also important, given that the multi-layer mirrors of gravitational wave detectors utilize SiO_2 as a low-index layer. The study of cation interdiffusion used nanolaminates of TiO_2, SiO_2 and GeO_2 to identify cation diffusion across the interface. The results show Ge and Ti cation interfacial diffusion, at temperatures above 500°C. Instead, Si cations diffuse into TiO_2 at a temperature around 850°C and Ti into SiO_2 at around 950°C. These temperatures correspond to an average of 0.8 of the glass transition temperature (Tg), with Tg=606℃ for GeO_2 and Tg=1187℃ for SiO_2. These findings support previous research by our group in amorphous GeO_2, which showed that elevated temperature deposition and annealing at 0.8 Tg, leads to favorable organization of the atomic network which is associated with low mechanical loss.

The second study of this thesis investigates the structural, mechanical, and optical properties of amorphous ternary oxide mixtures following post-annealing. These mixtures consist of TiO_2:GeO_2 combined with SiO_2 and ZrO_2, as well as TiO_2:SiO_2 combined with ZrO_2. Candidate high index layers, such as amorphous TiO_2:GeO_2 (44% Ti), and TiO_2:SiO_2 (69.5% Ti) exhibit low mechanical loss after post-annealing at 600°C, and 850°C, respectively. The inclusion of a third metal cation is shown to delay the onset of crystallization to temperatures around 800°C. The addition of a third metal cation also modifies the residual stress of the ternary compared to the binary materials. There is an indication of densification when annealing past 600°C. The reduction in residual tensile stress, combined with the higher crystallization temperature of the ternary mixtures, present attractive properties. These properties will expand the parameter space for post-deposition processing, mainly of the TiO_2:GeO_2 -based mixtures, to further reduce mechanical loss. This advancement paves the way for amorphous oxide coatings for gravitational wave detectors with lower mechanical loss, aligning with plans for future detectors.

ACKNOWLEDGEMENTS

I would like to acknowledge my advisor, Carmen Menoni, for all of her support and leadership in this research. Acknowledge my group members, Aaron Davenport, for his feedback, and mentorship on different topics. Maxwell Weiss, for his support with the deposition system and good discussions. Ela Jankowska, for her positivity and good advice. Other people who assisted me along the way, Emmet Randel, Ruth Osovsky, and Sangita Bhowmick. Le Yang, for her initial mentorship in the program. I would like to thank the LIGO collaborators, Ashot Markosyan from Stanford University, for his help with different measurements, as well as Martin Fejer, and Riccardo Bassiri from Stanford University for their advice. I would like to acknowledge the National Science Foundation Grants No. PHY 2110101 and 2309297 (Center for Coatings Research). In addition, I want to thank my family members for their moral support. I would like to thank God above else, for wisdom and strength.

TABLE OF CONTENTS

LIST OF TABLES

LIST OF FIGURES

Chapter 1

Introduction

Amorphous oxides grown via ion beam sputtering are the preferred coating material in highly reflective mirrors that act as test masses for gravitational wave interferometric detectors. Reducing the dominant thermal noise from these amorphous coatings is crucial to increase the sensitivity of detecting minute spacetime strains and capture complete astrophysical events. Thermal noise results from random displacement fluctuations in the coating, which experience internal friction, causing an anelastic relaxation mechanism by dissipating elastic energy. The dissipated internal elastic energy can be quantified through the mechanical loss angle (Q^{-1}). It has been shown that the high-index layer contributes the most to coating thermal noise (CTN). Consequently, research efforts have focused on mitigating the CTN of current implemented amorphous coatings, consisting of TiO_2:Ta_2O_5 (22.5% Ti), with potential candidates for future upgrades including TiO_2:GeO_2 (44% Ti), which lowers the CTN by approximately 32% in a multilayer stack with SiO_2 after annealing to 600°C, [62] with the goal of reducing it by 50%. Post-deposition annealing has been found to reduce mechanical loss, with concurrent studies linking it to atomic rearrangement leading to greater medium-range order in the amorphous structure, specifically observed for amorphous Germania annealed and deposited at temperatures of 0.8 of the glass transition temperature (Tg). [34] Furthermore, doping has been found to reduce mechanical loss, as observed in TiO_2:Ta_2O_5 (27% Ti), by creating a thermodynamically stable structure consisting of a ternary phase after

annealing to 600°C. [59] Interdiffusion between two distinct amorphous oxides, as observed between TiO_2 and Ta_2O_5 as nanolaminates after annealing to 650°C, has also shown a greater contribution to reducing mechanical loss.[94] Understanding the implications behind the structural rearrangements of these amorphous oxides after annealing is currently of interest to identify necessary steps to reduce mechanical loss.

This work investigates the interdiffusion mechanism between TiO_2 with GeO_2 and with SiO_2 to further understand when interdiffusion occurs and verify known structural changes occurring after annealing that would enable diffusion across the interface to a more thermodynamically favorable structure. Additionally, another study aims to investigate the addition of a third oxide into TiO_2:GeO_2 and TiO_2:SiO_2, both potential candidates for gravitational wave detectors, to determine if a more stable amorphous structure is created. Also, to study the structural integrity after annealing to check for failure such as due to stress, which is a current issue with certain amorphous coatings after annealing. All of this, in an effort to promote coating candidates to further lower mechanical loss.

In this chapter, Section 1.1 reviews the structure, properties, and fabrication methods of amorphous thin films. Section 1.2 introduces the application of the thin films that are studied and the motivation to the work. In section 1.3, the scope of the work is described.

1.1 Amorphous Thin Films

1.1.1 Structure, Properties, and Fabrication of Amorphous Thin Films

Amorphous thin films play a pivotal role in contemporary technology. The liquid-like random and disordered structure inherent in these solids imparts unique

characteristics that differentiate them from their crystalline counterpart. Noteworthy applications encompass flat screen displays, optical data transmission systems, optical windows and mirrors, as well as ion-conducting electrolytes essential for fuel cells and batteries. [1-4] The atomic structure of amorphous solids lacks long-range translational periodicity, a stark contrast to crystalline solids where atoms assume equilibrium positions within a translational periodic array. Generally, the structural ordering length scales of amorphous solids are categorized into Short-Range Order (SRO), Medium-Range Order (MRO), and Long-Range Structure (LRS). Short-Range Order (SRO) pertains to the arrangement of an atom concerning its nearest neighbors and is characterized by coordination, involving the number of atoms, bond length, and bond angle. Medium-Range Order (MRO), a subject of great interest, exhibits substantial variation depending on the type of amorphous solid structure. [5]

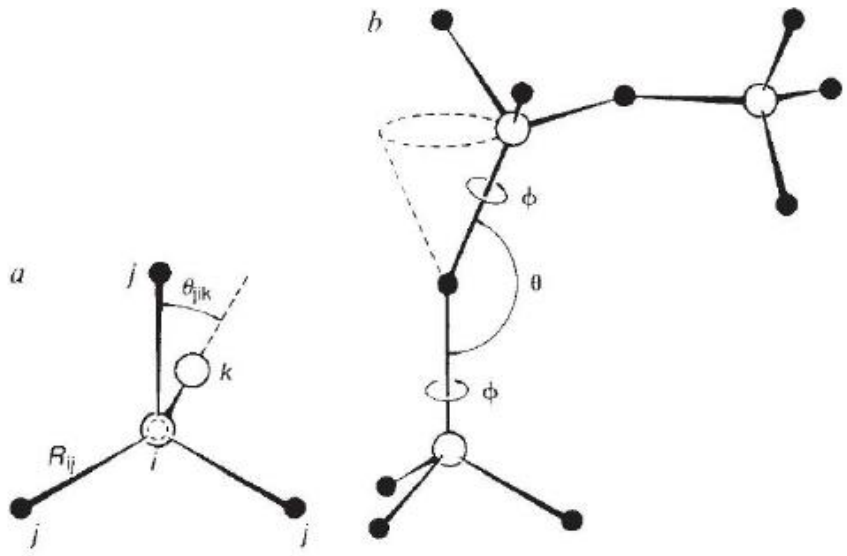

Figure 1.1 Illustration of short-range order; and (b) medium-range order and polyhedron connectivity. [6]

For covalent amorphous solids, SRO is defined within the 2-5 Å range, while MRO falls within the 5-20 Å range, with lengths beyond that considered LRS. As seen in figure 1.1, MRO represents an organized network arrangement past the SRO scale,

incorporating the type of angles (dihedral) and bond sharing to establish the next tier of local ordering, such as superstructural units consisting of a collection of connected polyhedra forming clusters and rings.[6] Both amorphous and crystalline phases may share commonalities in the SRO and MRO.

Amorphous metal oxides can be classified into three distinct types based on their network organization and structural roles: glass formers, intermediates, and modifiers. The glass-forming ability can be determined by key properties such as coordination number and bond strength. A glass former is usually characterized by a low coordination number, contributing to a stronger bond between a metal cation (M) and oxygen (O). In contrast, glass modifiers exhibit a high coordination number and weak M-O bonds. [7] For instance, the addition of alkali oxides dissociating in a-SiO_2 as modifiers results in the cleavage of M-O bonds due to the interaction with the electropositive alkali metal cation, leading to an increased presence of non-bridging oxygen and/or occupation of voids. [8] Intermediates occupy a structural position with their coordination number and bond strength values in between or similar to glass formers and modifiers. [7] A detailed examination of the atomic structure of amorphous metal oxides reveals a three-dimensional arrangement of metal-centers linked to oxygen atoms forming cages. (see Figure 1.2) Each polyhedron can connect through corner, edge, or face sharing (see Figure 1.2). According to Zachariasen [9], glass-forming ability is enhanced with a low coordination number, particularly when corner sharing involves at least three shared corners in a three-dimensional network. This results in a more open and less dense polyhedral structure. Amorphous GeO_2 and SiO_2 exemplify strong glass formers, characterized by a structural framework model widely acknowledged as a Continuous Random Network (CRN) with predominant covalent bonding [6,10].

The short-range order (SRO) manifests as a tetrahedral structure where each metal cation bonds to four bridging oxygens, forming GeO_4 and SiO_4. Meanwhile, medium-range order (MRO) adheres to the CRN model, comprising distorted interconnected corner-sharing tetrahedra that form rings of varying sizes. [11,12] (see figure 1.1) Techniques consisting of computational simulations paired with experimental techniques such as Raman spectroscopy, X-ray and Neutron Diffraction (total scattering), and so on, have been used to study the different ranges of these amorphous oxide structures. [11-14] Additionally, other models such as the Modified CRN, or Random Closed Packed (RCP) networks have been classified to other oxides mainly containing higher coordination number.[15]

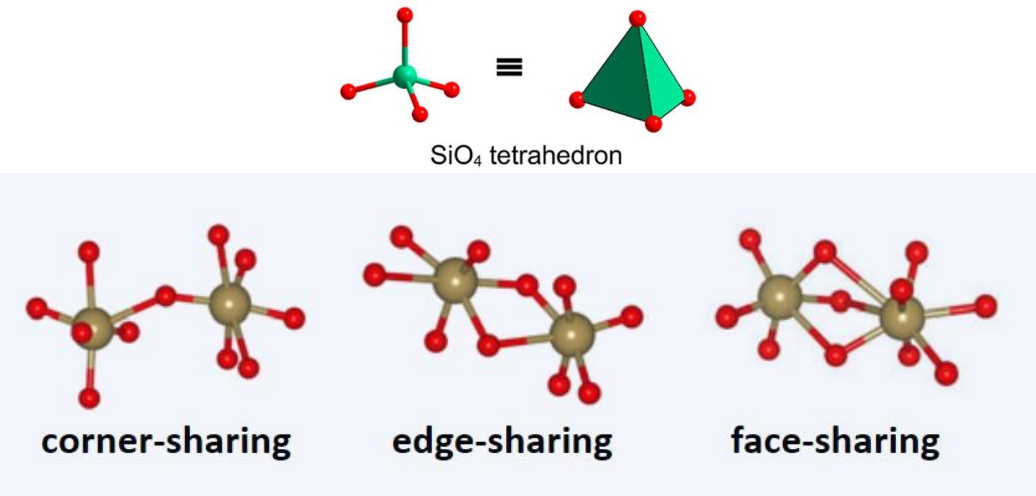

Figure 1.2: Schematic representation of (top) SiO4 tetrahedron, and (b) polyhedral connections through corner-sharing, edge-sharing, and face-sharing configurations. [40,128]

The random ring distribution of amorphous oxides is appealing for applications. Amorphous oxides can be produced with available techniques available techniques, such as physical vapor deposition methods, capable of producing large-scale homogeneous layers. Offering the flexibility to easily adjust composition and properties (i.e., refractive index for optical applications) [16,17]. In the broader context of

materials, intrinsic optical properties are influenced by physical processes, including electronic transitions, and lattice vibrations effects. In the case of amorphous semiconductors which can be oxides, high transmission occurs in the visible region, whereas in the UV region, optical absorption is induced by electronic transitions. Disordered fluctuations in atomic positions and impurities/dangling bonds give rise to a broad distribution of localized energy states within the bandgap, leading to the formation of a mobility gap (see Figure 1.3) and a broadening of the density of states. Consequently, this atomic disorder influences the emergence of an exponential 'Urbach' tail in the absorption coefficient edge [18,19].

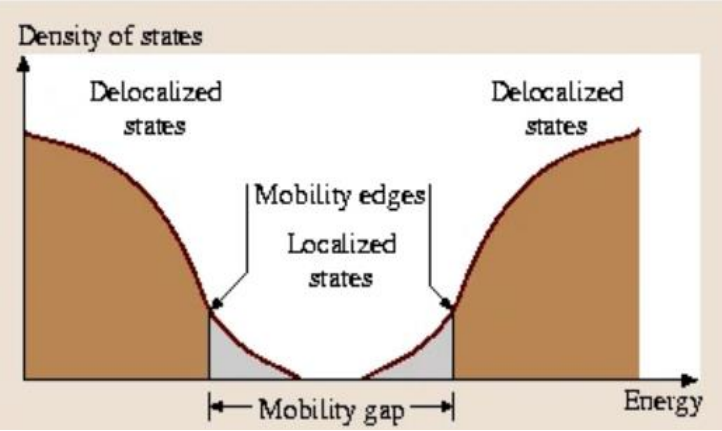

Figure 1.3: Schematic representation of the density of electronic states in amorphous semiconductors. [18]

In terms of mechanical properties, the examination of stress has been a focal point of investigation for amorphous thin films, and this subject is of current interest due to its profound implications for the usability, durability, and reliability of engineered devices. [21-22] Excessive tensile or compressive stress in the film is capable of inducing material failure, manifesting as phenomena such as cracking or buckling. Furthermore, stress exerts a notable influence on various other material properties, including conductivity, permittivity, etc. [21] Residual stress is recognized as the sum of intrinsic and thermal stresses. Intrinsic stress is commonly understood

to arise during the deposition process (such as sputtering, evaporation, etc.), and it is influenced by factors such as nucleation growth, deposition temperature, deposition rate, phase transitions, and other related parameters. A comprehensive understanding of intrinsic stress remains elusive, primarily due to the intricate nature of the plasma environment and deposition process. Conversely, thermal stresses are known to originate from disparities in the coefficients of thermal expansion between the thin film and substrate. [21-22]

Amorphous solids are traditionally fabricated through the rapid quenching of a liquid phase initially at a temperature above its melting point (Tm), utilizing fast cooling rates. This process bypasses the nucleation and growth of crystals, leading the material below its Tm to a supercooled liquid state until reaching low-temperature regions, also known as the glass transition temperature (Tg) range, where the viscosity becomes sufficiently high to be exhibited as a solid within observable time scales. Consequently, the supercooled liquid attains a metastable state as an amorphous solid or 'glass' due to insufficient relaxation of the atomic configuration. [16,23,24] The liquid to glass making technique is called melt quenching. Nonetheless, amorphous thin films ranging from angstroms to micron thicknesses can be effectively deposited using techniques associated with Physical Vapor Deposition (PVD). Commonly employed PVD methods utilize physical processes such as sputtering (ejection of atoms due to energetic collisions with ions) and evaporation (vapor phase generation due to thermal energy transfer). Within a vacuum chamber, a vapor flux is generated by either sputtering or evaporating a solid material target. The extracted supersaturated vapor, composed of energized atoms or clusters of atoms, is then directed onto a cold substrate. The sticking probability at the substrate induces atom-by-atom condensation, forming a thin film [23, 25]. PVD grows a different more stable amorphous structure,

unattainable through melt-quenching, due to its extremely rapid cooling.

Amorphous solids exist in a nonequilibrium metastable state, meaning that, for liquid-quenched glasses (LQG), structural differences can develop over a long time, resulting in undesired properties. The extent of structural rearrangement for stability upon cooling from liquid state has been characterized by the fragility (degree of viscosity near Tg) of the material. On the other hand, PVD has been recognized for its ability to form stable amorphous packing structures, a process that would otherwise take many years using physical aging techniques regarding LQG [16,24,38]. PVD has a long history of use in growing both organic [26,27] and inorganic [28-30] materials for various applications. Moreover, the intriguing ability of PVD to create stable glasses has sparked considerable interest and remains somewhat under debate. [38] As a result, extensive investigation has been undertaken to comprehend the factors contributing to the excellent thermodynamic and kinetic stability found in some vapor-deposited amorphous materials. One notable recognition of vapor deposition is attributed to the equilibration mechanism, involving enhanced atomic mobility on the less constrained free surface. It is believed that this enhanced mobility leads to more energetically favorable positions in the amorphous packing structure, where atoms have sufficient time to reach these positions before being buried by other atoms. [24,38,39] However, this is not a concluding observation as it has yet to be generalized between organic and inorganic materials.

Kinetic stability can be characterized by examining the onset of devitrification with respect to Tg (parameter linked to LQG processes) upon reheating. If the onset is shifted to higher temperatures, it indicates greater kinetic stability, as more thermal energy is required to rearrange atoms from their amorphous state [16,24,38]. As shown in Figure 1.4, the concept of stability in amorphous materials is popularly discussed

with regards to the potential energy landscape (PEL) paradigm (see Figure 1.4). PEL consists of a hypersurface representation (cross sectioned in 2D for simplicity) of the total potential energy of the system as a function of all coordinates of the atomic system. Kinetic stability would then correspond to the height of barriers between basins. Conversely, thermodynamic stability can be assessed by observing the fictive temperature (T_f), the temperature at which either the enthalpy or volume of a glass state point intersects with the extrapolated equilibrium supercooled liquid. [16,24,38] Stability is related to lower enthalpy values for the vapor deposited amorphous state as compared to the LQG. In the PEL, a state would be more thermodynamically stable the deeper it is in the potential energy. Reaching close to an equilibrium position. [16,24,38] As seen in Figure 1.4, vapor deposited amorphous states reach more stable packing structures than aged glasses, whereas the 'ideal glass' state corresponds to a theoretical limiting factor of amorphous packing at deep levels corresponding to a configurational entropy in similar magnitude as the crystalline state. [16,24]

However, there is ongoing investigation into the universal applicability of these stability criteria, particularly in the context of organic and inorganic amorphous structures, where the majority of research has covered organic materials [16]. Studies showing stability characteristics in vapor deposited metals [31,32], semiconductors [33], and oxides [15,34,35], to mention a few, have been studied. Vapor deposited Zr-based amorphous metals showed an increase in crystallization onset and Tg with low deposition rates and substrate temperatures below the Tg. [31,32] Similarly, the deposition of amorphous Si and GeO_2 at high substrate temperatures (~0.8 Tg) induces structural reorganization alongside a reduction in low-energy excitations. The relaxation mechanism is associated with coating internal friction, contributing to noise in the context of highly sensitive gravitational wave detection [33,34,36,37]. In addition,

post-deposition annealing also causes a reorganization in amorphous GeO_2, similarly, a restructuring can be seen with the ratio change of corner-shared to edge-shared polyhedral in ZrO_2:Ta_2O_5 leading to lower mechanical loss. [34,129] Nevertheless, substrate temperature, deposition rate, or post-deposition annealing are shown to play a role in changing the configuration of amorphous structures that are thermodynamically favorable in either organic or inorganic materials, however much research still needs to be done on amorphous oxides.

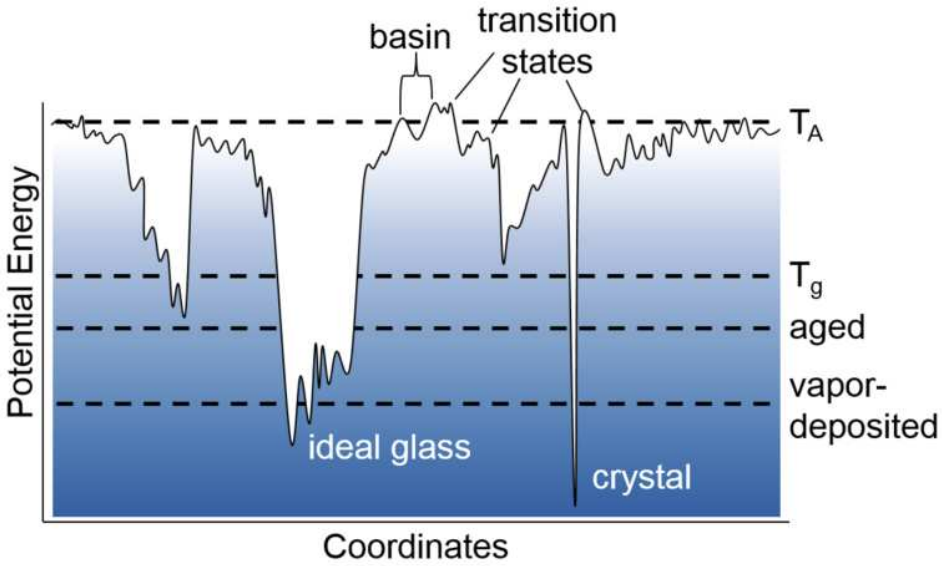

Figure 1.4: Schematic representation of the potential energy landscape (PEL) for glass forming systems. Depicting the potential energy as a function of configurational coordinates of the atomic system.[24]

1.2 Motivation

The work described in this thesis is dedicated to the structural, mechanical, and optical investigation of physical vapor deposited amorphous oxide thin films intended for application in the engineering of high reflection multilayer stacks for high finesse mirrors of the intermediate and end-test masses in laser interferometer gravitational wave detectors. A critical factor limiting the sensitivity of distance changes between these mirrors is thermal Brownian noise, primarily induced by coating fluctuations

resulting from the random motion of particles during operation. The intensity of this noise is defined by the internal friction within the coating, quantifiable through the measurement of the mechanical loss angle. The advancement of current and future detector upgrades and concepts hinges on the development of novel mirror coating materials aimed at mitigating Brownian thermal noise.

1.2.1 Gravitational Wave Detection

Gravitational waves emerged as a consequence of Einstein's general theory of relativity, proposed in 1916 [41]. In this theory, gravity is conceptualized as the curvature of spacetime caused by the presence of energy and mass of great magnitude. Consequently, gravitational waves (GW) are generated when masses undergo acceleration, propagating as ripples in spacetime at the speed of light. [42] Larger distances or smaller source events of astrophysical origin result in a weakening of the amplitude and hence a smaller strain effect (fractional length change) of GW as detected on Earth. Gravitational waves travel perpendicular to their propagation direction (z-axis), causing a deformation of space in a quadrupolar form, involving stretching and compressing of spacetime along the x, y, and z-axis. [42,43] GW detection poses a significant challenge due to their extreme sensitivity. The estimated strains influencing on the arms of GWD from astrophysical events to be detected are on the order of ~10^{-18} m or less. To put this into perspective, the radius of a proton is approximately~$8x10^{-16}$ m. [44]

Laser interferometers play a crucial role in addressing this challenge by enabling the detection of minute strain changes between the interferometer arms. The interferometers achieve this by measuring the phase change of the laser beam circulating in the cavity of one arm versus the other as a gravitational wave passes, causing destructive or constructive interference effects in the signal at the detector.

This can be translated into strain measurements represented as $(\Delta L_x - \Delta L_y)/L$, where L is the absolute distance of both arms, and ΔL_{x-y} is the distance change sum in the x and y direction. [42,43,44] Current ground detectors utilize a Michelson interferometer with Fabry-Perot cavities (see Fig. 1.5). Some of these GW detectors have arm lengths of 4 km because longer arm lengths result in more significant absolute strain changes caused by the weak GW. The 4 km length in each arm involves a Fabry-Perot cavity, which enhances sensitivity by allowing a high intensity beam through the arm. Additionally, it provides the flexibility to extend the arm lengths if needed. [45]

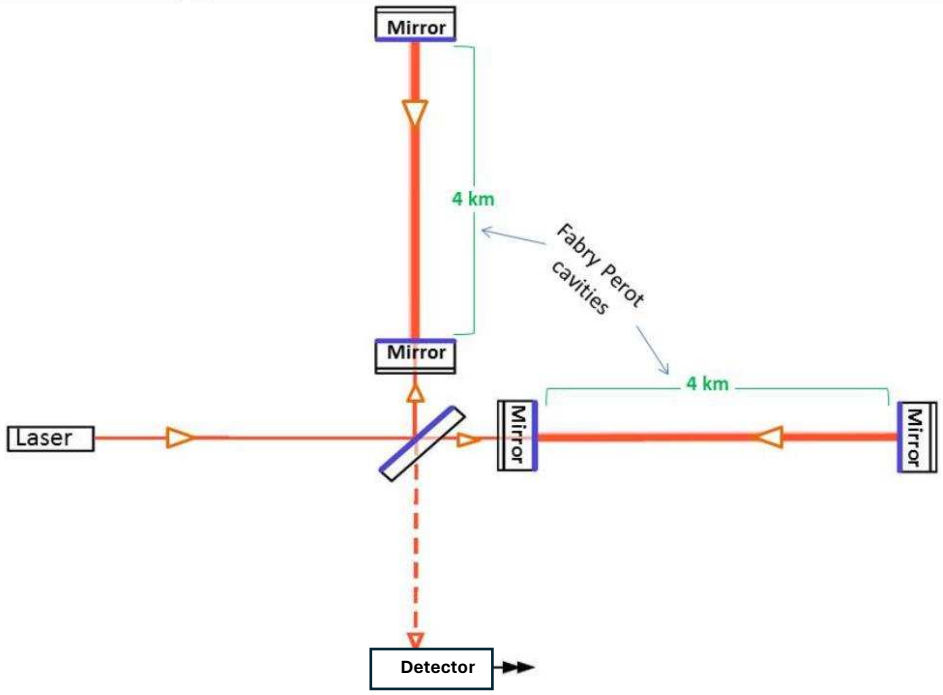

Figure 1.5: Schematic representation of a basic Michelson interferometer with Fabry Perot cavities. (Caltech/MIT/LIGO Lab)

On September 14, 2015, a groundbreaking moment occurred as the two Advanced LIGO (Laser Interferometer Gravitational Wave Detector) interferometers, situated in Hanford, WA, and Livingston, LA, successfully detected the presence of gravitational waves for the first time [46]. These gravitational waves originated from the collision of two black holes, positioned approximately 1.3 billion light-years away from

Earth. This historic event marked a significant milestone in the field of astrophysics, confirming the direct observation of gravitational waves as predicted by Albert Einstein's general theory of relativity.

1.2.2 Thin Film Coatings in the Test Masses of Gravitational Wave Detectors

Current detectors, such as the Advanced LIGO, consist of suspended highly reflective test mass mirrors placed at the end of the Fabry Perot cavity within the interferometer. These Bragg mirrors weigh 40 kg with a diameter of 34 cm. The substrate is made of fused silica and the coating consists of a multilayer stack of amorphous thin films with alternating high (n_H) and low (n_L) refractive index to create the interference for high reflectivity. Maximizing reflectivity at a specific wavelength (λ) at normal incidence can be calculated by tuning the thicknesses ($t_{H\text{-}L}$) as the following:

$$t_H = \lambda/(4n_H) \qquad (1.1)$$

$$t_L = \lambda/(4n_L) \qquad (1.2)$$

Noting that the bilayer has the high refractive index material on the top. In this way, at every interface in the stack a part of the beam is reflected. The reflected beam has a phase shift of π, between the low index to high index interface, causing multiples of 2π as the relative phase difference of reflected beams causing constructive interference. Furthermore, assuming a bilayer stack with thicknesses as shown above, the reflectivity of a multilayer coating in air or vacuum can be approximated:

$$R_{even} = \left(\frac{n_s(n_H/n_L)^{2N}-1}{n_s(n_H/n_L)^{2N}+1}\right)^2 \qquad (1.3)$$

$$R_{odd} = \left(\frac{n_H^2(n_H/n_L)^{2N}-n_s}{n_H^2(n_H/n_L)^{2N}++n_s}\right)^2 \qquad (1.4)$$

where R_{even} and R_{odd} are the reflectivity for even or odd number of layers, n_s is the

refractive index of the substrate and N is the number of bilayers in the stack. The ideal quarter wave thickness may vary depending on the bandwidth of the design target.

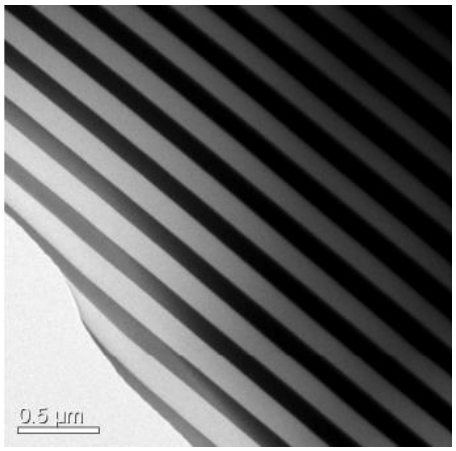

Figure 1.6: Bright field TEM of a multilayer stack of amorphous Ti-doped Ta_2O_5 (darker layers) and SiO_2. [47]

To meet the rigorous standards for optical performance, mirror coatings must demonstrate both high reflectivity and extremely low optical absorption loss at the operational wavelength (λ = 1064 nm). The current configuration of the Advanced LIGO detector employs amorphous SiO_2 and Ti-doped Ta_2O_5 as the low and high index layers, respectively. This shift from pure Ta_2O_5, chosen for its enhanced optical properties, is illustrated in Figure 1.6, showcasing a mirror coating with exceptional optical absorption loss measuring below 1 ppm [47]. The measured average absorption loss for the mirror coating at λ = 1064 nm was 0.14 ± 0.05 ppm [48]. It is noteworthy that in the field of amorphous oxide thin films, absorption loss can be associated with oxygen deficiency [49] and defects. Post-deposition annealing serves as a valuable tool to eliminate such defects and reduce absorption loss. [30]

1.2.3 Coating Brownian Thermal Noise

Various noise sources impact the displacement sensitivity of gravitational wave observatories. Figure 1.7. illustrates the noise budget of the Advanced LIGO interferometer during the third observing run (O3), which concluded in March 2020. [45] Thermal noise emerges as a significant factor in the middle frequency range (~50 to 450 Hz), predominantly attributed to Brownian noise in the optical coatings. Consequently, this has implications for the observatory's ability to detect GW within that frequency range.

Coating thermal noise originates from thermally driven random displacement fluctuations, commonly referred to as Brownian motion, within the coatings. This phenomenon impacts the coherence of the reflected or transmitted beam. Brownian noise is associated with a damping mechanism in the coatings, which is manifested through internal friction and is governed by the fluctuation-dissipation theorem. [50] Furthermore, internal friction, causing an anelastic relaxation mechanism by dissipating elastic energy in amorphous coatings, must be minimized to reduce Brownian noise. The anelastic behavior observed deviates from Hooke's Law, which describes a linear stress-strain relationship.

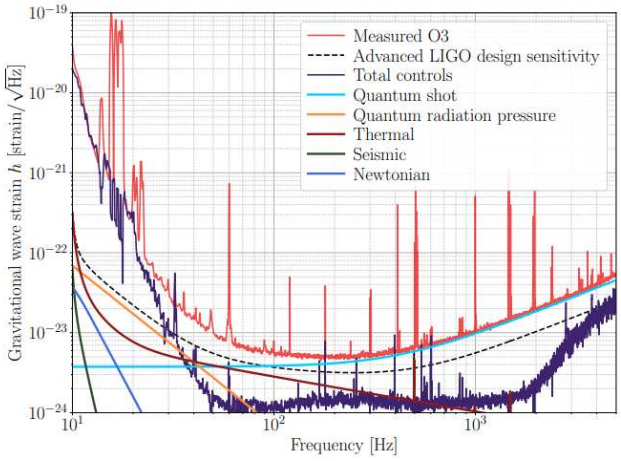

Figure 1.7: Simplified gravitational wave noise budget for O3 observation of LIGO Hanford.[45]

Equilibrium in strain is achieved after a certain period following the application or removal of stress. A periodic stress and its lagged equilibrium strain can be formulated as:

$$\sigma = \sigma_0 e^{i\omega t} \qquad (1.5)$$

$$\varepsilon = \varepsilon_0 e^{i(\omega t - \emptyset)} \qquad (1.6)$$

where σ is the applied stress and ε is the resulting strain with a phase lag of $\emptyset$, also known as the loss angle, to reach equilibrium. σ_0 and ε_0 are the amplitudes and ω the frequency. By further relating periodic stress and strain to complex elastic modulus (Y) [51],

Y = $\left|\frac{\sigma_o}{\varepsilon_o}\right| [1 + i\emptyset(f)]$, $(\emptyset \ll 1)$, one is able to further represent the mechanical loss angle:

$$\emptyset(f) = \frac{P}{2\pi f E} = \frac{1}{Q} \qquad (1.7)$$

where P is the energy dissipated per cycle of oscillation, E is the total energy stored in the oscillating system, f is the frequency and Q is the mechanical quality factor. Thus, the determination of internal friction intensity involves employing experiments such as coating ring-down methods to quantify the reciprocal of the quality factor (Q^{-1}). [52] Subsequent investigations conducted by Levin et al. [53] have advanced an analytical formalism that correlates the fluctuation-dissipation theorem with interferometer readout (displacement of test masses under internal thermal equilibrium). The theorem states that a system characterized by higher damping, when subjected to an external force, will exhibit increased thermal noise. This facilitates the computation of the power spectral density distribution of thermal noise. The primary objective is to establish a relationship between mechanical loss angle measurement and Brownian thermal noise. This association is realized through the application of a hypothetical oscillating pressure on the test masses' surface, mimicking the intensity distribution of the incident laser

beam (i.e. Gaussian profile). Thus, the power spectral density of thermal displacement becomes:

$$S_b(f) = \frac{2k_B T}{\pi^2 f^2} \frac{P}{F_0^2} \qquad (1.8)$$

where k_B and T are the Boltzmann's constant and the temperature of the mirror, respectively. F_o is the amplitude of the oscillating force distributed over the surface, and P is the elastic power dissipation of the test masses, which contains the loss angle as seen in equation 1.7. The dissipation term can be further evaluated by numerical analysis of the integrated force through the volume of the mirror, considering the elastic properties and mechanical dissipation at each point. The Brownian thermal noise power spectral density for a coating on a half-infinite substrate can be approximated as:

$$S_c = \frac{2k_B T}{\pi^2 f E_s} \frac{d}{w^2} \phi_c \left(\frac{E_c}{E_s} + \frac{E_s}{E_c}\right) \qquad (1.9)$$

where E_s and E_c are the substrate, and multilayer coating Young's modulus, d is the total thickness of the coating, and w is the beam spot size. Assumptions for this formula encompass a homogenous mechanical loss, equal mechanical loss for shear and bulk displacements. Also, a small incident beam spot size compared to the mirror diameter. Overall, assuming the Poisson's ratio to be negligible, and coating properties to be isotropic. [54] One can deduce that reducing Brownian noise on the coating encompasses reducing the coating thickness, reducing mechanical loss, decreasing the Young's modulus differences between coating and substrate, and increasing beam spot size.

1.2.4 Current Status of Coating Research on Coatings for Gravitational Wave Detectors.

Ion beam sputtered (IBS) amorphous oxides have been the preferred coating material for multilayered stacks in highly reflective mirrors designed for gravitational

wave detectors for 1064 nm wavelengths. This preference is primarily attributed to their ability to achieve exceptionally low levels of optical absorption at 1064 nm wavelength and mechanical loss. In the initial interferometer configuration, multilayer mirror coatings comprised of IBS amorphous SiO_2 and Ta_2O_5, resulting in optical absorption plus scattering levels of approximately 1 ppm [57]. Notably, the high index layer, represented by Ta_2O_5 in this case, was identified as the primary contributor to mechanical loss (~3.2 x 10^{-4}, from 60 to 1100 Hz), surpassing the mechanical loss of the low index layer SiO_2 (~4.5 x 10^{-5}, from 50 to 900 Hz).[58] Subsequent investigations focused on mitigating the mechanical loss from the high index layer, leading to the selection of a TiO_2:Ta_2O_5 mixture coating with approximately 22.5% Ti content. Post-treatment annealing at 600°C resulted in a significant ~40% reduction in mechanical loss from Ta_2O_5 [47]. This particular mixture coating is presently employed as the high index coating in laser interferometers, such as the Advanced LIGO.

A study aimed at comprehending the atomic structure in relation to the mechanical loss [59] of IBS TiO_2:Ta_2O_5 mixture thin films revealed that a 27% Ti cation content corresponds to a thermodynamically stable structure characterized by a ternary phase ($TiTa_{18}O_{47}$) occurring after annealing. In contrast, a Ti cation content of 53% resulted in a phase-segregated structure. The mixture with the lower Ti percentage exhibited a greater reduction in mechanical loss (~2.8 x 10^{-4}, at 1kHz) after annealing to 600C, and a higher onset of crystallization, indicating a more stable amorphous structure. Other materials were combined with Ta_2O_5, and the lowest mechanical loss after annealing was observed in parallel with the formation of a ternary phase. This phenomenon was evident in the case of ZnO: Ta_2O_5 (~20% Zn) and TiO_2:Ta_2O_5 (~27% Ti). [15]

It has been widely observed that thermal annealing in amorphous oxides

contribute to a reduction in room temperature mechanical loss. To gain a deeper understanding of the structural reorganization occurring post-annealing, a combination of molecular model simulations and experimental studies has been undertaken. In the case of amorphous ZrO_2:Ta_2O_5 mixtures, X-ray scattering techniques, coupled with modeling, revealed alterations in medium-range connectivity followed after annealing up to 800°C. This modification involved a shift from corner-sharing to edge-sharing polyhedra, contributing to the reduction in mechanical loss. [60] Similarly, IBS amorphous Ta_2O_5 has demonstrated an increase in medium-range order, as determined by Fluctuation Electron Microscopy (FEM), after annealing at 600°C, concurrently leading to a decrease in mechanical loss. [61] Furthermore, Raman spectroscopy measurements conducted on amorphous GeO_2 indicated an elevated ratio of six-membered rings after annealing at 400°C. A greater population increase for as-deposited and after annealing prior to ~400°C was observed with the deposition occurring at elevated substrate temperatures (0.83 Tg). This mechanical loss was found to correlate with a higher population of six-membered rings, which also signifies an increase in medium-range order. [34]

Additional research has been conducted on binary amorphous oxide candidates with the aim of achieving lower mechanical loss values in the high-index layer and minimizing optical absorption. The next detector upgrade, referred to as Advanced LIGO A+, targets a 2-fold reduction in total coating Brownian noise, translating to a 4-fold reduction in mechanical loss measurements. In the course of this investigation, the incorporation of TiO_2 into GeO_2 was explored at various cation percentages. This addition to GeO_2 was employed to elevate the refractive index, enhancing contrast with SiO_2 in a multilayer stack and consequently reducing the overall multilayer coating thickness. Subsequent examinations revealed that a 44% Ti content in a single layer (141nm thick)

led to a decrease in mechanical loss to approximately $1.17x10^{-4}$, between 1kHz to 30 kHz, after annealing at 600°C for 10 hours, further reducing to about $0.96x10^{-4}$ for 108 hours, while remaining in an amorphous state. Additionally, the absorption was close to 2 ppm [30]. This TiO_2:GeO_2 mixture underwent further refinement to diminish absorption and integrate into a multilayer high reflector of TiO_2:GeO_2 /SiO_2, striving to meet the specified benchmark for thermal noise. As of December 2023, work conducted by Davenport et al. demonstrated that initial challenges related to blister defect formation in the multilayer stacks after annealing were mitigated through the reduction of water partial pressure and the control of coating stress using process parameters such as base pressure and deposition temperature. Stack designs exhibit a coating Brownian noise measured at 0.67-0.69 of aLIGO, with ongoing designs focusing on reducing the influence of TiO_2:GeO_2 thickness on thermal noise in the stack [62]. Other potential binary amorphous oxide candidates encompass a TiO_2:SiO_2 mixture with a Ti content of 69.5%, demonstrating a coating Brownian noise reduction of 0.76 of aLIGO after annealing at 850°C. Nevertheless, crystallization occurs at approximately 550°C [63], and there is an emergence of blisters and cracking, which may be contingent on the specific process utilized for deposition. [64]

Other alternatives to binary amorphous oxides are nanolaminate structures. This approach involves the incorporation of nanometer-thick layers (<50nm) comprising two or more intercalated amorphous oxides. Particularly, nanolaminate stacks have demonstrated the ability to postpone crystallization when compared to single layers. [68] Moreover, they exhibit potential for mitigating mechanical loss at cryogenic temperatures, a critical consideration for the advancement of cryogenic GWD aimed at further minimizing noise. [69]

Another noteworthy alternative is single-crystalline materials such as AlGaAs,

with a mechanical loss hovering around 4×10^{-5}, between 1 to 6 kHz, emerge as a competitive candidate. [71] However, upscaling production to 34 cm mirrors and birefringence is of technological concern.

1.3 Scope of the Work

In this thesis I investigate the atomic modifications in amorphous oxides and their impact on the structural, mechanical, and optical properties during post-deposition annealing for low CTN coatings for upgrades of upcoming gravitational wave detectors. I have shown that post-annealing in close proximity to the glass transition temperature influences structural changes, such as interdiffusion between two amorphous metal oxides. Additionally, I explore in this thesis, ternary oxide single layers, an area less studied compared to binary oxides, as potential high-index layers for mirrors in gravitational wave detectors. The optical, structural, and mechanical properties of different compositions are evaluated after annealing.

Thus, I organized the thesis as follows, Chapter 2 contains the description of the techniques used to characterize and deposit the amorphous oxide thin films. In chapter 3, it involves two nanolaminates consisting of intercalating layers of stoichiometric amorphous GeO_2/TiO_2 and TiO_2/SiO_2 deposited by IBS. The cation content for TiO_2, GeO_2, and SiO_2 acting as the top nanolayer was assessed for different post-annealing conditions. The onset of crystallization and crystal structure evolution with annealing was evaluated. In chapter 4, the study involves the deposition of ternary oxide mixtures by IBS, consisting of TiO_2-SiO_2-doped GeO_2, TiO_2-ZrO_2-doped GeO_2, and TiO_2-ZrO_2-doped SiO_2. The residual stress, optical absorption, thickness, refractive index, and crystallization onset were explored for the different compositions after annealing to different temperatures. Finally, Chapter 5 provides a summary of the work and outlines research needed to comprehend the applicability of these films in advancing next-GWD.

Chapter 2

Experimental Method

This chapter, section 2.1 provides a detailed description of the ion beam sputtering deposition system used to grow the amorphous oxide thin films. Section 2.2 describes the thin film characterization techniques to obtain the morphology, structure, composition, and optical properties.

2.1 Ion Beam Sputtering Deposition

Thin films were produced in this work using ion beam sputtering. The process involves accelerating energetic noble gas ions and directing them towards the surface of a solid metal target. This collision induces the sputtering effect, wherein energy transfer from ions much larger than the atomic bond energy, causes the dislodgment of target atoms from the surface. The resulting sputtered atoms or atom groups travel to the substrate in a vapor phase where it condenses. The substrate is strategically positioned in close proximity and path of the sputtered species. The ability of physisorbed atoms to diffuse beyond the point of impact is constrained and relies on the substrate temperature and energy of the adatoms. Metal oxide formation occurs with an oversaturation of oxygen. These reactive species combine with metal atoms at the target and on the substrate, culminating in the creation of metal oxide thin films onto the substrate.

2.1.1 Biased Target Ion Beam Sputtering

Laboratory Alloy Nanolayer System (LANS) manufactured by 4Wave Inc. was used to deposit the amorphous metal oxide thin films mentioned in this thesis. This system utilizes a negatively biased target to attract the positively charged noble gas ions for sputtering. The theory of operation is the following:

The plasma employed for sputtering is generated through the utilization of a Hollow Cathode Electron Source (HCES) and a gridless End-Hall Ion Source, leveraging the Hall effect as described below. The HCES primarily supplies electrons for the ionization of the working gas, Argon (Ar), for plasma discharge. The ion source is designed to confine electrons for impact ionization, subsequently accelerating the ions (Ar+) towards the chamber which are then attracted by the biasing of the target for sputtering.

The HCES comprises a cathode tip and a keeper (see Figure 2.1). Argon gas is introduced into the HCES to enhance free electron discharge. Current is applied and regulated by the bias controller, which is current-controlled, determining the voltage between the cathode tip (-) and ground (+). This regulates the electron emission from the hot filament. Additionally, current is applied and regulated by the keeper controller, also current-controlled, determining the voltage between the cathode tip (-) and the keeper (+). This controls the electron discharge towards the chamber and ion source. The table below shows the HCES, and ion source parameters used to enable a stable plasma for sputtering:

Table 2.1. HCES and ion source operation parameters for plasma generation

Operation step	Filament Bias (A)	Cathode Bias (A)	Anode Vo	Anode Current (A)
Enabling HCES	1.5	8	--	--
Enabling Ion Source	1.5	8	100	7.5
Deposition Step	1.5	6.2	60	5.7

Furthermore, the ion source serves as an anode with a truncated cone opening, and a magnetic field is generated by a magnet positioned behind the smaller base of the cone, situated behind the backing plate. The electrons discharged from the electron source flow towards the anode while interacting with the magnetic field. The anode (+) attracts these electrons, and the magnetic field increases their residence time, causing collisions with the Ar gas, resulting in sufficient impact ionization. The interaction of electrons with the magnetic field dictates the plasma discharge due to the voltage between the anode and

cathode, subsequently determining the electric field used to accelerate the low-energy ions for sputtering.

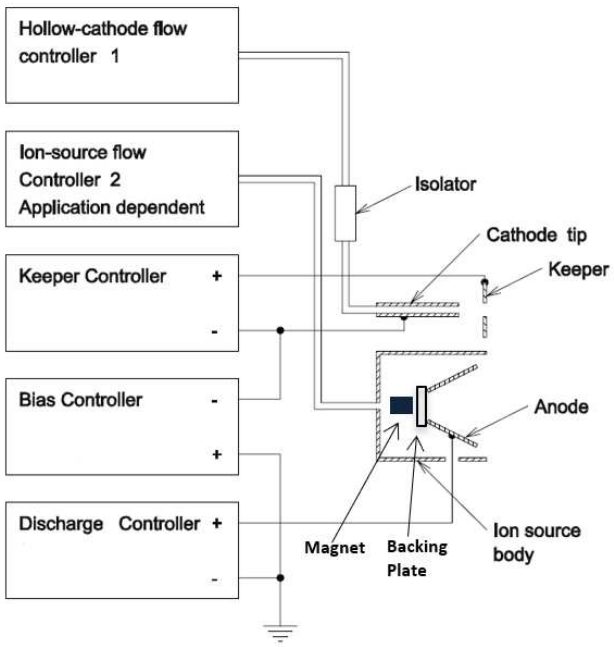

Figure 2.1: Electrical diagram of the Hollow Cathode Electron Source and Ion Source for the LANS.

The positively charged Ar flux is broad enough to reach the metal targets which are positioned in a six-sided inverted carousel geometry in between the ion source and substrate stage (see Figure 2.2). The ions reach the target at near normal incidence based on the plasma divergence. Each target is electrically isolated to avoid cross contamination and can undergo an asymmetric bi-polar pulsed DC bias or DC for sputtering of conductive or semi-conductive targets. The target's duty cycle can be controlled by providing sufficient positive bias, typically 10V, to remove any dielectric build up, also to attract electrons for etching. Target negative voltages ranging from -10 to -1000V are selected to alter the energy distribution of the sputtered adatoms. Moreover, the pulsed DC frequency is adjustable, with a maximum value of 71.4kHz. In

this system, up to 3 targets can be sputtered simultaneously, and the duty cycle and frequency are independent of each other. Table 2.2 shows the gas and target parameters to deposit different compositions of TiO_2 doped GeO_2.

Table 2.2. Deposition parameters for different compositions of TiO_2 doped GeO_2. Two metal targets were used of Ti and Ge.

Material	Dep time (s)	Ion Source Ar (sccm)	HCES Ar (sccm)	Oxygen (sccm)	Voltage (V)	Pulse width (positive) (us)
GeO2	4200	51	20	6	-800	Ge: 50
TiO2:GeO2 (~10% Ti)	5210	48	20	12	-800	Ge:63/Ti:2
TiO2:GeO2 (~33% Ti)	16430	48	20	12	-800	Ge:80/Ti:2
TiO2:GeO2 (~44% Ti)	27000	51	20	12	-800	Ge:89/Ti:2
TiO2:GeO2 (~63% Ti)	42000	48	20	12	-800	Ge:96/Ti:2

Nevertheless, a plasma sheath (~2mm) is developed at the surface of the negatively biased targets which accelerates positive ions entering the sheath. This provides no effect from the target voltage variations on the plasma trajectories between source and targets. In addition, the typical deposition substrate temperature is at an average of 100°C.

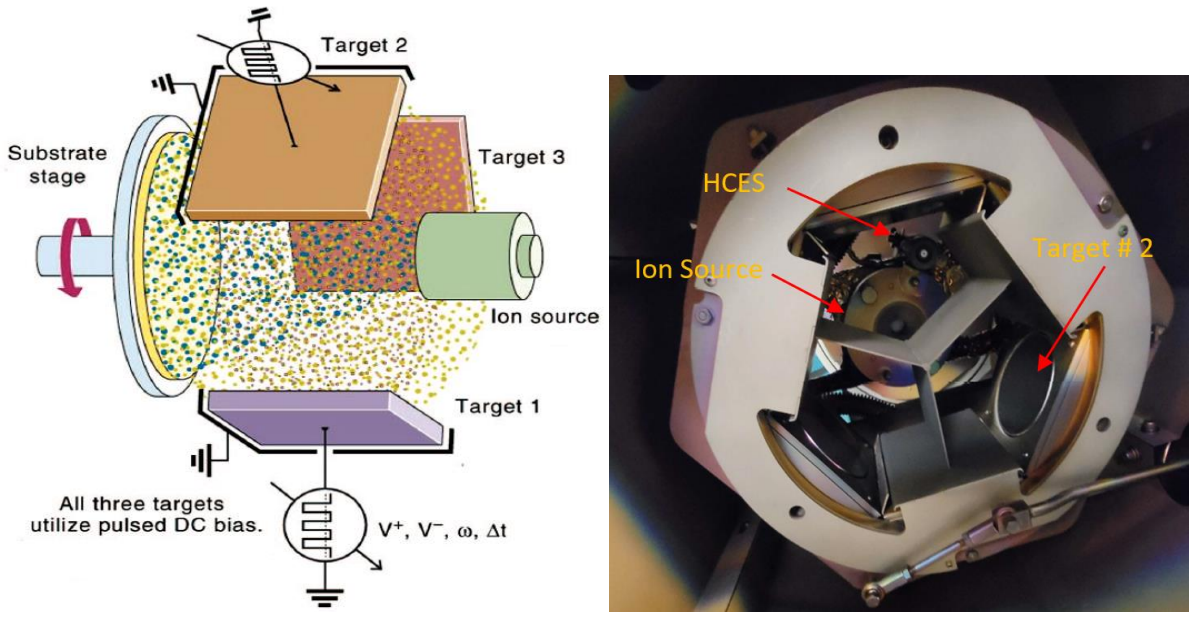

Figure 2.2: Schematic of the target, substrate stage, and ion source configuration of the LANS. (Right), Picture showing the same without the stage. (Left)

In order to minimize ion scattering in the plasma, the pressure in the chamber needs to be low enough to increase the mean free path of the particles in the plasma allowing for a more efficient travel of sputtered atoms. A base pressure of less than $9x10^{-8}$ Torr and operating pressure of ~ $4x10^{-4}$ Torr are common. In order to produce metal oxide thin films, ultra-pure oxygen gas is flowed into the chamber in between the ion source and substrate stage, but closer to the substrate stage in order for the metallic adatoms to react with the oxygen on the substrate surface. In addition, the uniformity of the film is enhanced by rotating the substrate stage, but its area is limited by the sputtered plume hitting the stage dependent on the deposition system. A load-lock component allows the extension and retraction of the stage to and from the main chamber, which uses a high vacuum isolation valve located in between for the purpose of pressure conditioning (see Figure 2.3).

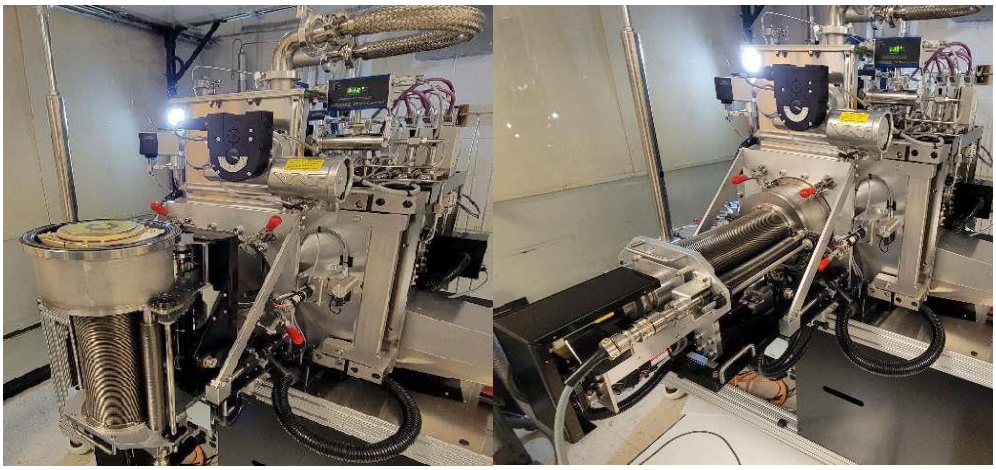

Figure 2.3: Loadlock in substrate loading mode. (Right). Loadlock in mode of extension of substrate stage into chamber. (Left)

2.2 Thin Film Characterization

2.2.1 Ellipsometry

The thickness, refractive index and extinction coefficient of thin films can be determined through Spectroscopic Ellipsometry. In this technique, a light beam with a known polarization is directed onto a sample. The reflected light becomes elliptically polarized (see Figure 2.4) due to the interaction of the electric field with interfaces of varying plane parallel material layers. This measurement is continuous as a function of wavelength over a spectral range of interest. The sensitivity of ellipticity is enhanced when the incident angle is close to Brewster's angle of the substrate. Subsequently, the elliptically polarized reflected light is detected, and the ellipsometric angles, consisting of the ratio of amplitude diminutions (Ψ) and the phase difference (Δ), are measured. These parameters can be correlated with the complex Fresnel coefficients of reflection ratio (ρ) which involves the s and p components of the decomposed electric field vectors (Es and Ep). For an isotropic material the following relationship holds:

$$\rho = \frac{r_p}{r_s} = \left| \frac{\frac{E_p^r}{E_p^i}}{\frac{E_s^r}{E_s^i}} \right| e^{i(\delta_P - \delta_S)} = \tan\psi e^{i\Delta} \qquad 0 \le \psi \le 90° \;\; \& \;\; 0 \le \Delta \le 360° \qquad (2.1)$$

The E symbolizes the electric field vector and the subscripts/superscripts "i", "r", "s", and "p" denote the incidence, reflection, s-polarization, and p-polarization, respectively. The phase change between p and s polarization is the '$\delta_P - \delta_S$' term.

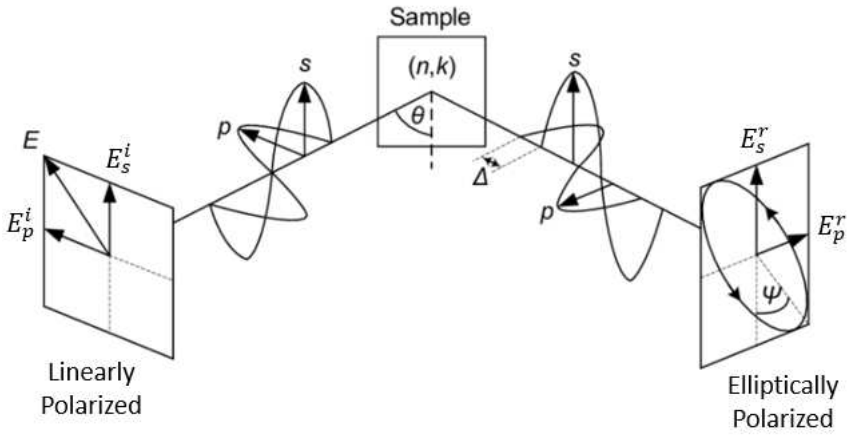

Figure 2.4: Schematic representation of ellipsometry technique.

It is also important to mention that the dielectric function (ε) and optical constant dependence on wavelength/photon energy is called dispersion. For an optically homogeneous and isotropic nonmagnetic optical material the following formula shows the relation:

$$\sqrt{\varepsilon(\lambda)} = \tilde{n}(\lambda) = n(\lambda) + jk(\lambda) \qquad (2.2)$$

Spectroscopic ellipsometry captures Ψ and Δ values throughout different wavelengths. In this study, we utilized a Horiba UVISEL spectroscopy ellipsometer. The instrument employs parameterization techniques based on dispersion formulas to determine optical constants. This involves fitting either an empirically derived model or a classical oscillator model, which can have one or multiple oscillators, to align with the experimental acquisitions of Ψ and Δ. The latter model is derived from equations of motion that represent a material, such as a bound charge interaction with light, and may include parameters with physical significance, such as bandgap. The fitting model finds a solution to n and k directly (e.g Cauchy) or solves for the dielectric function (e.g. Tauc Lorentz).

Each model is tailored to the specific characteristics of the material, whether it be a metal, dielectric, polymer, etc. Additionally, the models are designed to

accommodate specific spectral regions, in this instance, the total range that can be measured is from 0.59 eV to 6.5 eV. The relationship between the thickness of the thin film and the optical constants n and k is established through the Fresnel coefficients of reflection (r). Furthermore, these parameters are interconnected with Ψ and Δ, as illustrated in equation 2.1. Specifically, the equation outlines the relationship for an air/film/substrate design.

$$r_{p,total} = \frac{r_{af,p} + r_{fst,p}e^{-i2\beta}}{1 + r_{af,p}r_{fst,p}e^{-i2\beta}},\ r_{s,total} = \frac{r_{af,s} + r_{fst,s}e^{-i2\beta}}{1 + r_{af,s}r_{fst,s}e^{-i2\beta}} \qquad (2.3)$$

where,

$$r_{af,p} = \frac{\tilde{n}_f \cos(\theta_a) - \tilde{n}_a \cos(\theta_f)}{\tilde{n}_f \cos(\theta_f) + \tilde{n}_a \cos(\theta_a)},\ r_{fst,p} =. \ . \qquad (2.4)$$

$$r_{af,s} = \frac{\tilde{n}_a \cos(\theta_a) - \tilde{n}_f \cos(\theta_f)}{\tilde{n}_a \cos(\theta_a) + \tilde{n}_f \cos(\theta_f)},\ r_{fst,s} =. \ . \qquad (2.5)$$

the phase change (β) from top to bottom of the film contains the thickness (d),

$$\beta = 2\pi \frac{d}{\lambda} \sqrt{\tilde{n}_f^2 - \tilde{n}_a^2 \sin^2(\theta_a)} \qquad (2.6)$$

The subscripts "a," "f," and "st" correspond to the ambient, film, and substrate, respectively. θ represents the angle of incidence or refraction. The integrated software Delta2Psi provides a user interface for modeling thin films. The modeling process involves stacking blocks to represent the experimental design as closely as possible. Each block may contain a dispersion reference or a dispersion model specific to each layer/multilayer and substrate material. Before fitting, the parameters provided typically encompass the substrate's dispersion, number of layers, angle of incidence (AOI), and thickness estimate. The unknown parameters mainly consist of the optical constants of the film and its thickness. Introducing a roughness layer on the surface may be necessary to achieve a more accurate goodness of fit. If the thickness is already

known, it can serve as a fixed initial parameter, accelerating the fitting process. Once a realistic model is established, the fitting process employs a numerical optimization method, such as the Levenberg-Marquardt algorithm, for curve fitting through model parameter estimation of the nonlinear function. This algorithm iteratively adjusts the model's parameters to minimize the sum of squared differences between the experimental and calculated values of Ψ and Δ. Nevertheless, the algorithm utilizes the dispersion model to obtain the n and k values, which are iteratively adjusted along with the thickness to ideally converge on a global minimum. The precision of thickness, n, and k depends on the amount of information provided. In this case, it relies on the spectral range being fitted. The ideal fitting range for various materials and models can be discovered in literature. Additionally, besides noting a high Chi-square value indicating failure, other indicators include negative thickness values, negative dispersion values, and for transparent materials, an index of refraction that increases with larger wavelengths. Moreover, by employing an AOI of 60 degrees, a spectral range between 1 to 5 eV, and utilizing a multi-oscillator model known as the Tauc-Lorentz model with 3 oscillators, one can derive the optical constants of a TiO_2:GeO_2 single-layer mixture, as illustrated below:

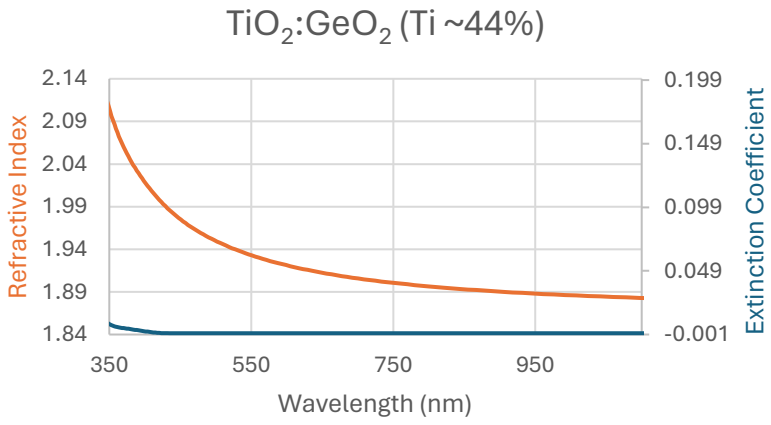

Figure 2.5: Refractive index and extinction coefficient of a single layer of TiO_2:GeO_2 (~44%Ti).

2.2.2 X-ray Photoelectron Spectroscopy (XPS)

X-ray photoelectron spectroscopy (XPS) is employed for the examination of the atomic composition and chemical state of amorphous oxide thin films. The focus is on understanding their oxidation states and the bonding environment of elements present at the material's surface. This technique relies on the photoelectric effect, wherein high-energy X-ray photons bombard the surface, leading to the emission of photoelectrons from atomic inner shells. The energy of the incident X-ray photon ($h\nu$) needs to be high enough to overcome the binding energy of the inner-shell electrons (E_B), sample or spectrometer work function (ϕ_{sa}, ϕ_{sp}), and provide enough kinetic energy (E_K), to the emitted photoelectron for travel to the detector. The following relationship applies:

$$E_k^{sa} = h\nu - E_B - \phi_{sa} \quad (2.7)$$

where E_k^{sa} is the photoelectron's kinetic energy after leaving the surface. In addition, the following work function relations are considered:

$$E_k^{sa} + \phi_{sa} = E_k^{sp} + \phi_{sp} \quad (2.8)$$

where E_k^{sp} is the photoelectron's kinetic energy detected by the spectrometer. Thus, eq 2.7 can be rewritten as:

$$E_k^{sp} = h\nu - E_B - \phi_{sp} \quad (2.9)$$

The detected kinetic energy of the photoelectrons is shown to be independent of the sample's work function, representing the energy difference between the material's Fermi energy level and vacuum level. On the other hand, the binding energy depends on the atomic number of the material and can be calculated since $h\nu$ is a stable energy value, and ϕ_{sp} is a known calibration constant for energy measurements, specific to the instrument. While different X-ray sources may alter the measured kinetic energy, the binding energy remains the same per material. Consequently, XPS enables the

identification of elements due to their unique atomic number.

Moreover, XPS facilitates the examination of oxidation states, as each state contributes to distinct binding energy positions, influenced by changing barriers arising from the electronegativity of neighboring atoms. Thus, a discernible trend of higher cation binding energy emerges as the oxidation state of the atom increases. Generally, it is useful to study the changes in the atomic environment by comparing spectra with those found in literature. Furthermore, the area of the peaks correlates with the quantity of specific elements present in the sample. Quantification of atomic percentage can be achieved by dividing each element's peak area with their corresponding relative sensitivity factor, a calibration factor.

Angle-resolved XPS enables the non-destructive probing of the sample at various take-off angles, thereby increasing/decreasing the information depth (D). This depth serves as an approximation of the sample's probing thickness, from which 95% of the detected photoelectron signal originates. (See Figure 2.6) The following formula can be used for this approximation:

$$D \cong 3\lambda_i \sin(\theta) \quad (2.10)$$

where λ_i is the inelastic mean free path, and θ is the take-off angle, with respect to the surface of the sample. Eq. 2.10 is derived from the Beer-Lambert relationship for a 1400 eV X-ray source. The λ_i can be calculated from the TPP-2M formula [72], using the QUASES-IMFP-TPP2M software. This formula requires the bulk density and bandgap of the material.

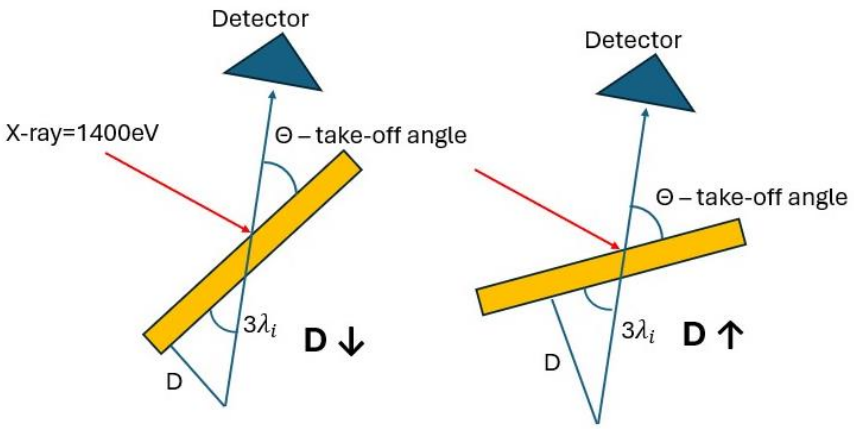

Figure 2.6: Schematic representation of varying angles effect on the information depth (D).

The efficiency of the photoelectron collection relates to the sensitivity of the instrument, expressed as counts per second. Electronic core-levels within an element will have different photoionization cross sections, reason why empirical relative sensitivity factors are used to obtain estimates of atomic composition with varying orbitals in mixtures. The shift in binding energy due to charging effects in the sample requires a correction by referencing an undisturbed energy peak such as C 1s. However, errors may arise due to improper deconvolution of the peaks. In terms of quantification, uncertainties can be calculated using the Monte Carlo procedure in CasaXPS, which is used to estimate the uncertainties associated with the parameters obtained from the peak fitting process. It involves randomly sampling the fitting parameters within their uncertainty ranges and recalculating the peak fitting for each set of sampled parameters. By analyzing the distribution of the fitted parameters obtained from the Monte Carlo simulation, statistical measures such as standard deviation or confidence intervals can be calculated. These measures provide estimates of the uncertainties associated with the fitted parameters, reflecting the variability introduced by measurement noise and fitting algorithms. As an example, the Si 2p photoelectron signal is shown, which corresponds to the electrons emitted from the 2p orbital of silicon

within a silica network. Assuming a bulk density of 2.2 g/cm^3 and a bandgap of 9.1 eV for silica. The following figure shows the approximation of the information depth at different take-off angles, as well as the intensity signal of the peak:

Take-off angle (degrees)	Information depth approx. (nm) of SiO2
30	~6.2
45	~8.7
60	~10.7

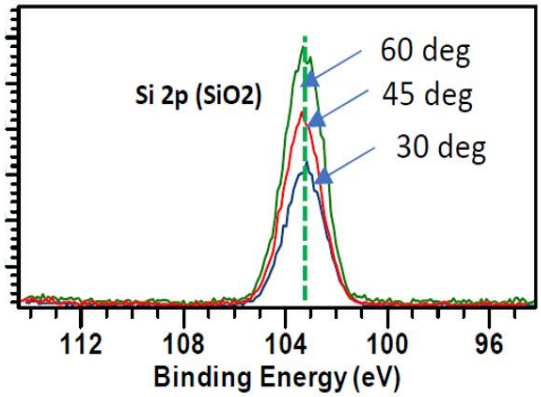

Figure 2.7: High-resolution Si 2p spectra using angle resolved XPS.

In this work, XPS measurements were carried out with a Physical Electronics PE 5800 ESCA/ASE system equipped with a monochromatic Al Kα X-ray source. Depositions for XPS purposes were done on p-type Si (100) wafers. A take-off angle of 45° was used for all scans. The neutralizer operated at 20 μA to counteract the charging effect on the surface. High-resolution scans were obtained from the sample's surface. The instrument's base pressure was around 3×10^{-9} Torr. The C 1s peak position at 284.8 eV was used to calibrate the binding energy scale of the spectra. CasaXPS software (version 2.3.24) was used to analyze the spectra.

2.2.3 Photo-thermal Commonpath Interferometry (PCI)

The optical absorption of amorphous oxide thin films was determined through Photo-thermal Commonpath Interferometry (PCI), employing a pump/probe technique, as shown in Figure. 2.8, based on the thermal lensing effect. The examination of optical absorption occurred at the wavelength of the pump beam, set at 1064 nm, with powers

in the range of 5 to 8 W detecting absorptions down to ~1 ppm. A red He-Ne laser served as the probe beam, detecting the absorption effect induced by the pump on the material. The probe beam is characterized by a larger beam diameter and low power to avoid absorption contributions. Nevertheless, the pump beam is focused to interact with the material of interest, resulting in localized heating and a consequent alteration in the refractive index at the center of the probe beam. Subsequently, the heated region of the material acts as a small thermal lens at the center while in contact with the probe beam. As a result, the probe beam diffracts from the center of the probe beam and acquires an on-axis phase shift, distinct from the undistorted region of the probe. The resulting phase distortion ($\Delta\varphi$) term shown below can be multiplied to the complex amplitude of the probe wave:

$$\exp(-i\Delta\varphi) \sim 1 - i\Delta\varphi \quad (2.11)$$

Thus, the probe consists of two waves, where the undistorted probe wave is represented by unity and the weaker distorted wave is represented by $-i\Delta\varphi$. At the waist region (w) of the probe beam, interference patterns are not formed by the two waves due to being out of phase by $-\pi/2$. The diverging wave from the distorted region interferes with the undistorted region, with the point of maximum intensity contrast occurring at the Rayleigh distance (z_R) of the weak distorted wave from the origin (z=0), where $z_R = \pi w_{z=0}^2 / \lambda$,. Here, Δφ=ΔI/I, where ΔI represents the difference between maximum and minimum intensity, and I denotes the intensity of the undistorted probe wave, assuming a Gaussian wavefront. The maximum signal can be probed at this point using a photodiode. [73]

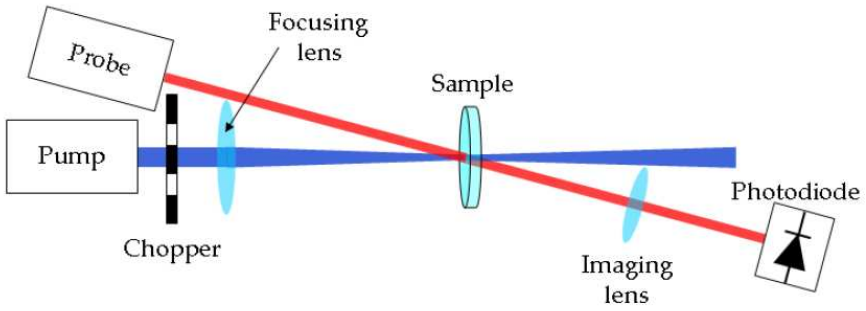

Figure 2.8: Schematic representation of the Photothermal Commonpath Interferometer used. [74]

Moreover, sensitivity is maximized by employing a chopped pump beam at a specific frequency, inducing periodic heating. This periodic heating leads to a periodic distortion of the probe beam wavefront. The signal is detected by the photodetector, and the signal-to-noise ratio is enhanced by the lock-in amplifier synchronized with the chopping frequency. Consequently, the sensitivity of PCI relies on the amplitude of the AC signal acquired as the pump power increases and is absorbed by the material without reaching the damage threshold. Also, in this technique, the transverse resolution depends on the pump spot size, while the longitudinal resolution is influenced by the pump/probe crossing angle and changes in the index of refraction. The measured signal is converted into voltage, with peak voltages compared to a calibrated sample of known voltages which is proportional to absorption, through a linear relation. In practice, depositing thin films on fused silica enhances the contribution solely from the film due to the much lower coefficient of thermal expansion of fused silica. Optical absorption measurements as low as 1 ppm can be measured. [73]

2.2.4 Carrier Frequency Interferometry (CFI)

The radius of curvature (RoC) of the amorphous oxide thin films were obtained through Carrier Frequency Interferometry (CFI) technique. The RoC can be used to obtain the residual stress of the coating after deposition and/or annealing. The technique uses a Michelson interferometer set up, as seen in Figure 2.9, a He-Ne collimated beam is expanded to form a planar wavefront, this wavefront is directed onto a beam splitter which reflects and transmits the beams to a flat ($\leq \lambda/4$) reference sample and the sample of interest. The beam reflects from each of these samples and recombine at the beam splitter which then travels to the CCD detector. With equal arm lengths, between beam splitter and samples, interference fringes are created when recombined and detected.

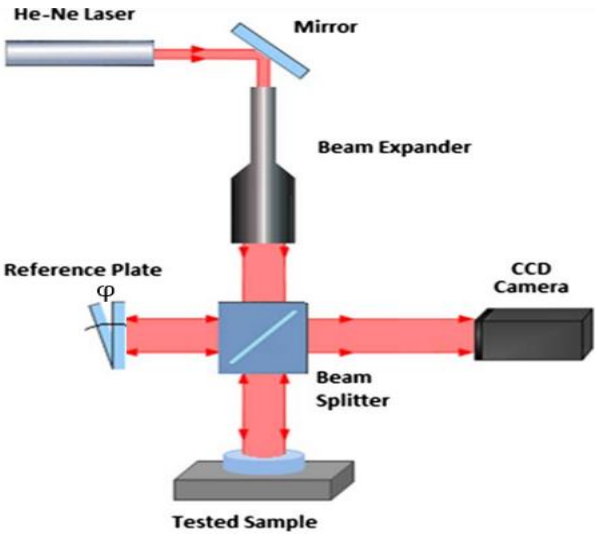

Figure 2.9: Schematic representation of Carrier Frequency Interferometry used. Modified from [75]

Due to the curvature of the test sample, a deformed wavefront reflects off which

causes a modulation of the phase. The following formula represents the intensity field of the interference signal, if a tilt (ϕ) about the y-axis is implemented between the two wavefronts:

$$g(x,y) = a(x,y) + b(x,y)\cos\big(2\pi f_o x + W(x,y)\big) \quad (2.12)$$

where $a(x,y)$ and $b(x,y)$ represents variations in the background intensity, and fringe visibility, respectively. $f_o = \sin(\phi)/\lambda$ is the carrier frequency on the x-axis. $W(x,y)$ is the phase modulation due to the test sample wavefront deformation. In order to obtain the RoC, the Fourier transform of the interference fringe patterns are taken, as shown in Figure 2.10, the frequency domain shows the $a(x,y)$ term at the center, and $b(x,y)$ term would be shifted from the center at a distance determined by f_o which is the dominant contributor to the modulated signal. The shifted signal of interest would then be filtered out, clearing any noise contributions, and then implementing an inverse Fourier transformation. Ideally, the imaginary and real part of the result would then need to be computed using an *arctan* operation to obtain the phase of the interference fringe pattern. Thus, the phase distribution of the deformed wavefront is given, which represents the 3-dimensional image of the RoC, in a wrapped form between -π to +π. The 3D image then follows an unwrapping procedure which aims to reconstruct the true, continuous phase from the wrapped phase values. It involves identifying the discontinuities in the phase and adding or subtracting multiples of 2π to ensure a smooth, continuous phase profile. The reconstructed 3D surface can then be fitted using a Zernike polynomial, to calculate the RoC, such as the z_2^0 (however, limited to the defocus wavefront type). The residual stress of the film (σ_f) is obtained from the RoC, which uses the Stoney equation:

$$\sigma_f = \frac{E_s h_s^2}{6h_f(1-\nu_s)}\left(\frac{1}{R_p} + \frac{1}{R_b}\right) \quad (2.13)$$

where R_p and R_b are the RoC after and before deposition. h_s and h_f are the thickness of the substrate and film, respectively. E_s and ν_s are the Young's modulus and Poisson's ratio of the substrate, respectively. The Stoney equation is based on several assumptions, including uniform film and substrate thickness, infinitesimal strains and rotations, homogeneous and isotropic materials, and other specific stress and curvature conditions. It is widely used but has limitations, particularly when the curvatures are high or when the assumptions are violated. [78] Errors in the measurement of ROC originate when the sample is very flat, due to the fitting of a Zernike polynomial (curved hypersurface) to a flat surface. Thus, a very flat surface may generate high amounts of errors to be usable.

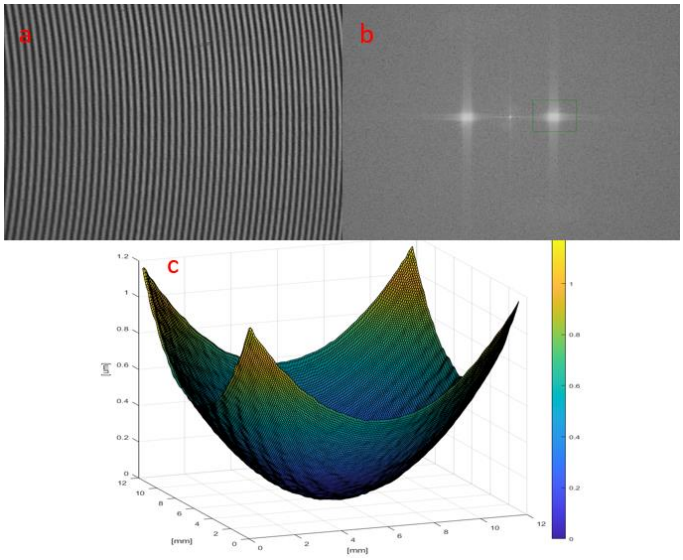

Figure 2.10: a) Interferogram of 30 m RoC calibration sample, b) Fourier transform domain, and c) RoC 3D representation after phase unwrapping.

2.2.5 X-ray Diffraction (XRD)

In this study, X-ray diffraction (XRD) is employed to investigate the onset of crystallization in amorphous oxide thin films following annealing. Additionally, the evolution of the crystalline structure is examined. The technique utilizes X-rays with wavelengths on the order of angstroms, comparable with the spacing between atomic

lattices. Consequently, the incident X-rays interact with the electron clouds surrounding the atoms, resulting in elastic scattering of the X-rays in directions dictated by the periodic arrangement of the crystal lattice. XRD operates in accordance with Bragg's law, where X-rays incident upon the crystal lattice at a specific angle undergo constructive interference if the path length difference between two adjacent lattice planes is zero or a multiple of the X-ray wavelength. This event produces a reflected scattering pattern referred to as the diffraction pattern. Therefore, Bragg's law articulates the conditions necessary for constructive interference to manifest, contingent upon the angle of incidence (θ) between the incident X-ray and the crystal lattice plane, the X-ray wavelength (λ), and the interplanar spacing (d). The expression is detailed below:

$$\sin\theta = \frac{n\lambda}{2d} \quad (2.14)$$

where n is the diffraction order. Therefore, the angular positions, and intensities of the diffraction peaks identifies the crystal lattice structure and orientation present. In terms of data collection, the sample is rotated at various angles while being bombarded by X-rays. The rotation of the sample allows the different crystal (hkl) planes to align with the incident X-ray beam for diffraction pattern creation. A detector measures the intensity of the diffracted X-rays at different angles. The diffraction pattern intensity peaks as a function of 2θ, which helps to determine the crystalline phase of the forming crystal. The broadening of the peaks, for instance, hints to smaller crystallite size because the diffracted X-rays sample a distribution of lattice planes with different orientations.

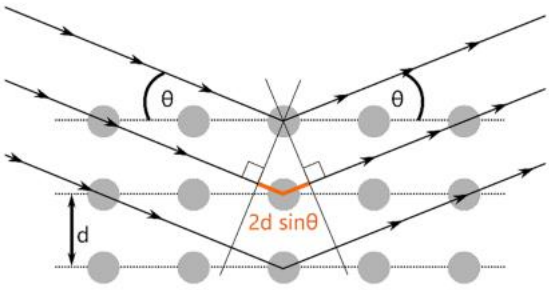

Figure 2.11: Schematic representation of Bragg diffraction in a crystal [76]

In ordinary XRD, the diffraction pattern is typically collected at a wide range of angles (2θ) around the sample, covering both low-angle and high-angle diffraction. However, in this work, Grazing Incidence XRD is used which involves the detector typically positioned at low incidence angles (~0.5° to 4°) from the surface. This is conveniently above the critical angle for which below total internal reflection occurs. While the detector is moved on the normal 2θ circle. This configuration maximizes the sensitivity to surface scattering and enhances the detection of diffraction signals arising from thin surface layers. Typically, for GIXRD, a Bruker D8 Discover diffractometer with a Cu Kα source at grazing incidence angle is used to examine the amorphous states of amorphous thin films. The diffracted beam was collected by a scintillation detector as a function of 2θ in the range between 10° to 50°.

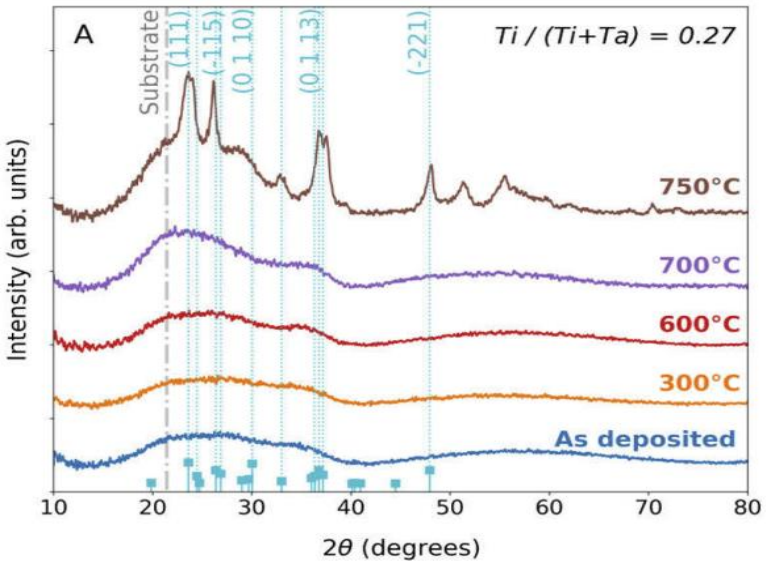

Figure 2.12: GIXRD results for a TiO_2:Ta_2O_5 (27% Ti) single layer film after annealing to different temperatures. [59]

2.2.6 Spectrophotometry

This study employs spectrophotometry to acquire transmission spectra of amorphous optical coatings. These spectra aid in discerning the presence of absorbing species in the sample, such as a non-stoichiometric oxide exhibiting defects like oxygen vacancies or contributions from metallic free electron transitions. Additionally, the optical bandgap for amorphous structures can be approximated using the Tauc plot, which relies on the proportionality expressed as, $((\alpha(E)h\nu)^{1/n} \propto h\nu - E_g)$ where α is the absorption coefficient, $h\nu$ is the photon energy, and E_g is the bandgap. The parameter n is contingent upon the type of electronic transition and the band structure of the material [77]. Fundamentally, the technique involves directing photons within the UV-IR wavelengths towards a sample, where the light can either be absorbed, transmitted, reflected or scattered. Transmittance is subsequently measured as $T = I/I_0$, where I is the intensity of the transmitted beam, and I_0 is the reference intensity of the beam before interacting with the sample. For this investigation, a Perkin Elmer Lambda 1050 Spectrophotometer is employed. This instrument features three detectors, enabling the

measurement of spectra within the range of 175 nm to 3300 nm. Specifically, a photomultiplier, a cooled InGaAs detector, and a PbS detector are utilized for the respective wavelength ranges of 175-186 nm, 860-2500 nm, and 1800-3300 nm. This spectrophotometry utilizes a double monochromator to improve the measurement linearity by reducing the stray light. In addition, it uses a double beam configuration, where a single light source is split into equal intensities, one beam goes to the reference side, and the other beam goes to the sample side. This allows simultaneous comparison in real time between sample and reference beam, reducing measurement error due to source fluctuations. Below shows the transmission of a SiO_2 (top layer) and HfO_2 antireflective coating for 1030 nm target with an incidence of 0°.

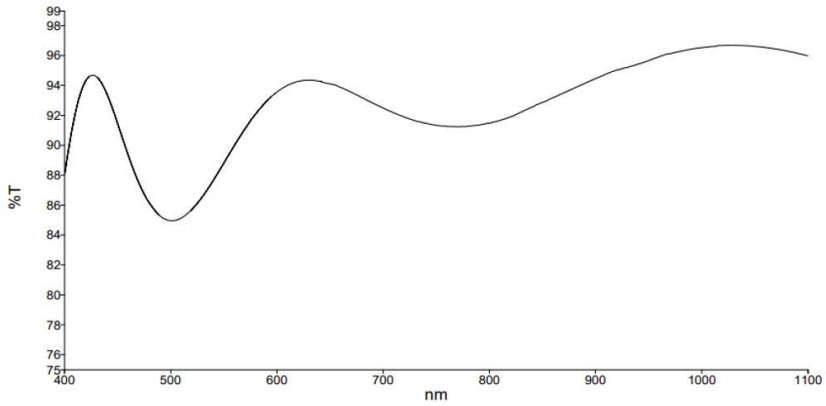

Figure 2.12: Transmission spectra of a 1030nm AR one sided coating using SiO_2 and HfO_2.

Chapter 3

Cation Interdiffusion Between Amorphous Oxide TiO_2 with GeO_2 and with SiO_2

This research is motivated by the need to identify key processes that occur in thin film metal oxides of TiO_2:GeO_2 and SiO_2 which are the components of multilayer dielectric stacks being investigated for coatings of the end and intermediate test masses of aLIGO interferometer. The combination of TiO_2:GeO_2/SiO_2 in the engineering of multilayer dielectric stacks has the potential to reach a coating thermal noise approaching 0.5 that of aLIGO, a goal of the O5 plans for the Hanford and Livingston detectors. [130] Assessment of cation interdiffusion with annealing is important because the process can lead to changes in coating thermal noise.

3.1 Introduction

Cation interdiffusion has been observed in amorphous oxides. In an experiment that used a nanolaminate structure consisting of a 1.6 nm thick layer of TiO_2 and SiO_2 and 6 nm of Ta_2O_5, Le et.al showed that annealing to 650°C causes the Ti to diffuse into the Ta_2O_5 layer and vice versa. The use of a nanometer thick bilayer sample is necessary to be able to probe the variations in the bonding network using X-ray Photoelectron Spectroscopy. [94] Interestingly, post-annealing to 650°C for 10 hours did not cause Ti to diffuse into SiO_2 and vice versa. The implications of these results are twofold: the Ta and Ti cation diffusion that occurs at around 650°C is key for the network to organize into a state that favors the reduction of mechanical loss, seen for TiO_2:Ta_2O_5 (27% Ti).

[59, 94] The lack of diffusion of Ti into SiO_2 upon annealing to 650°C ensures the reflectivity of the multilayer dielectric stacks to remain constant throughout the annealing process, as interfaces remain atomically sharp. Also, the lack of diffusion did not contribute to lowering the mechanical loss. Using the same strategy as seen in [94], the experiment consisted of identifying cation diffusion on TiO_2 with GeO_2 and TiO_2 with SiO_2. Nanolaminate stacks were deposited by ion beam sputtering and annealed to different temperatures. X-ray photoelectron spectroscopy was used to identify any diffusion while probing the topmost nanolaminate. The results indicate cation interdiffusion between TiO_2 and GeO_2 occurs after annealing at 600°C, and similarly between TiO_2 and SiO_2 after annealing between 900°C and 1000°C. The onset of cation interdiffusion takes place at an average of 0.8 of the glass transition temperature (Tg) corresponding to the glass network formers, GeO_2 and SiO_2. The onset of crystallization of TiO_2 in anatase form is observed after annealing to 700°C and 600°C for the TiO_2/GeO_2 and TiO_2/SiO_2 nanolaminates, respectively. The differences in ionic radius and known modifications in the atomic range-order occurring close to the Tg could activate the interdiffusion.

3.2 Experimental Methods

Nanolaminates of TiO_2/SiO_2, and GeO_2/TiO_2 were prepared by reactive biased target ion beam deposition technique using a LANS system manufactured by 4Wave.Inc.[103] and described in section 2.1.1. The operational parameters for deposition are described in Table 3.1.

Table 3.1: Deposition parameters for each TiO_2, GeO_2 and SiO_2 nanolaminate

Material	Deposition rate(nm/s)	Oxygen (sccm)	Target Voltage (V)	Duty Cycle
TiO2	0.0033	3	-800	2%
GeO2	0.02	6	-800	11%
SiO2	0.008	3	-800	25%

The initial chamber base pressure of ~5×10^{-8} Torr. Figures 3.1 and 3.4 show four designs consisting of TiO_2/SiO_2 and GeO_2/TiO_2 nanolaminates of 2 pairs grown on top of sapphire and a Si (100) wafer, respectively. The thickness of the top nanolayer was chosen due to its capacity to significantly inhibit the detected photoelectron signal from the bottom nanolayer. Moreover, the top nanolayer was switched between both oxides found in the stack. TiO_2 as the top nanolayer was deposited with an approximate thickness of 30 nm. The bottom layer contained either SiO_2 or GeO_2 with a thickness of around 9 nm, this is equivalent to a Ge and Si cation ratio of ~30 atom%. GeO_2 and SiO_2 as the top nanolayer were deposited with an approximate thickness of 13 nm and 15 nm, respectively. In the same order, the bottom TiO_2 nanolayer was roughly 3 nm and 7 nm. Each sample represented two pairs of TiO_2/SiO_2 and GeO_2/TiO_2 nanolaminates. These stacks were post-annealed in air by ramping up the annealing temperature at 1.5 °C/min and soaking at a set temperature for 10 hours with a Fisher Scientific Isotemp programmable furnace.

Moreover, diffusion studies at increased annealing temperatures were performed by obtaining a high resolution XPS spectra of each relevant element of the nanolaminate. XPS measurements were done on 4 layered amorphous oxide nanolaminates of TiO_2 alternating with GeO_2 and SiO_2. For the GeO_2/TiO_2 nanolaminates, the Ge 3d, O 1s, and Ti 2p orbitals were measured. Conversely, for the TiO_2/SiO_2 nanolaminates, it involved the Si 2p, O 1s, and Ti 2p orbitals. X-ray

Photoelectron Spectrocopy parameters are described in section 2.2.2.

Grazing Incidence X-ray Diffraction (GIXRD) measurements were performed utilizing an X-ray Diffractometer PANalytical X'Pert system equipped with a Cu-Kα X-ray tube source. A fixed incidence angle (θ) of ~3° from the surface was maintained, with scanning regions between 10 to 50° of 2θ, where θ represents the angle between the incident beam and the diffracted beam. The XRD samples were designed to have 15 pairs of the same thickness as the GeO_2/TiO_2 XPS sample, however, the TiO_2/SiO_2 sample had a thickness of 11nm for TiO_2 and 7 nm for SiO_2. This was done to obtain a better diffraction signal from the nanolaminates.

Spectrophotometry was done for the GeO_2/TiO_2 nanolaminates XRD design, between 200 nm and 1200 nm spectral range, after consecutive anneals to 500C and 600C for 10 hours.

3.3 Results and Discussion

In a general scope, metal-oxide nanolaminate stacks have the ability to enhance material properties compared to thicker single oxides. Consequently, these nanolaminates enter a broad number of fields. [82,83,84,85,86] The presented study optimizes the design of nanolaminates to examine the diffusion of cations within the top nanolayer. The X-ray Photoelectron Spectroscopy (XPS) technique, known for its shallow probing depth, was used for this purpose. This approach builds upon the methodology employed in previous study with identical deposition processes [94]. Moreover, the study involves two nanolaminates consisting of intercalating layers of stoichiometric amorphous GeO_2/TiO_2 and TiO_2/SiO_2 deposited by ion beam sputtering. The cation

content for TiO_2, GeO_2, and SiO_2 acting as the top nanolayer was assessed for different post-annealing conditions. The onset of crystallization and crystal structure evolution with annealing was determined from Grazing incidence X-ray diffraction (GIXRD). In the GeO_2/TiO_2 and TiO_2/SiO_2 nanolaminates, Ti cation diffusing into the GeO_2 and SiO_2 nanolayer is identified after annealing for 10 hours at temperatures of 600°C, and 1000°C, respectively. Additionally, Ge and Si cations diffusing into the TiO_2 nanolayer are identified after annealing at temperatures of 600°C and 900°C for 10 hours, respectively. The intermixing for both nanolaminates occurs at an average of 0.8 of reported glass transition temperature (T_g) of the glass network formers (GNF) in the stack. The initiation of interdiffusion is discussed in relation to modifications in the range order of the GNF upon annealing.

Figure 3.1 shows the XPS spectra of the GeO_2/TiO_2 nanolaminate designs for the as-deposited sample and after annealing at 600°C for 10 hours. The spectra obtained from the sample in which GeO_2 is on top, is shown on the left of the figure. On the right of the figure, the XPS spectra obtained from the sample in which TiO_2 is the top layer is shown. For both designs, the top nanolayer is fully oxidized and remains the same after annealing (Fig. 3.2 & 3.3); a Ge 3d orbital with oxidation state of Ge^{4+} (binding energy of 33.1±0.1 eV) and Ti 2p with oxidation state of Ti^{4+} (binding energy of 458.7±0.1 eV for Ti $2p_{3/2}$ and 464.5±0.1 eV for Ti $2p_{1/2}$). The contribution from Ge^{3+} is negligible for the as-deposited sample and disappears completely after high temperature annealing. The Ti 2p doublet peak remains stoichiometric through all the annealing runs with a constant doublet energy separation of 5.7±0.02 eV. For the left section, the Ti 2p doublet

peak in the as-deposited GeO_2/TiO_2 nanolaminates is attenuated from the XPS analysis depth. Similarly, for the right section, the Ge 3d peak in the as-deposited sample is insignificant.

Annealing shows a pronounced influence in the XPS spectra of the GeO_2/TiO_2 nanolaminates. For the left section, the Ti 2p and O 1s signal remains similar to the as-deposited sample at annealing temperatures up to 500°C. After annealing at 600°C, the Ti 2p doublet peak (Ti $2p_{3/2}$ and Ti $2p_{1/2}$) emerges, which indicates Ti cation diffusion into the top GeO_2 nanolayer. The O 1s peak fitting supports the contribution from emerging Ti^{4+} species. The Ti $^{4+}$ species contribution to the Ti 2p and O 1s orbital increases after annealing at 700°C. (Fig. 3.2). The Ti cation percentage, shown in Figure. 3.10, shows an additional increase of ~4% after annealing to 700°C. For the right section, the Ge 3d and O 1s peak remains similar to the as-deposited sample at annealing temperatures up to 500°C. After annealing at 600°C, the Ge 3d peak emerges, which indicates Ge cation diffusion into the top TiO_2 nanolayer. The O 1s peak reveals the contribution from emerging GeOx and Ge^{4+} species. (Fig. 3.3) Similarly, after annealing to 700°C, the Ge 3d and O 1s peaks reveal a ~6% additional increase of Ge cation diffusion. The cation percentage is plotted in Figure.3.10.

Figure 3.4 shows the XPS spectra for two designs of the SiO_2/TiO_2 nanolaminates for the as-deposited sample and after annealing at 900°C for 10 hours. The spectra obtained from the sample in which SiO_2 is on top, is shown on the left of the figure. On the right of the figure, the XPS spectra obtained from the sample in which TiO_2 is the top layer is shown. For both designs, the top nanolayer is fully oxidized before and after

annealing; a Si 2p orbital with oxidation state of Si^{4+} (binding energy of 103.4±0.1 eV) and Ti 2p with oxidation state of Ti^{4+}. The Ti 2p doublet peak remains stoichiometric through all the annealing runs with a constant doublet energy separation of 5.7±0.02 eV. For the left section, the Ti 2p doublet peak in the as-deposited SiO_2/TiO_2 nanolaminates is removed from the XPS analysis depth. Likewise, for the right section, the Si 2p peak in the as-deposited sample is insignificant.

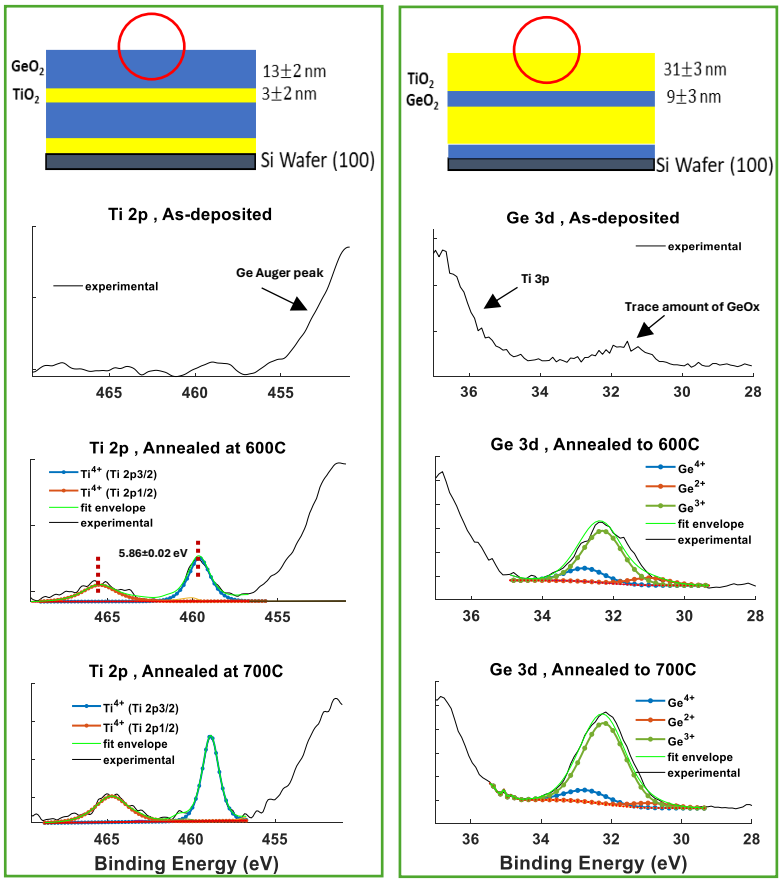

Figure 3.1. XPS spectra for Ti 2p and Ge 3d signatures of the GeO_2/TiO_2 nanolaminate's top nanolayer for as deposited, and after annealing for a soaking period of 10 hours at 600°C and 700°C. (Red dotted line is the fitting baseline).

As seen in the GeO_2/TiO_2 nanolaminates, annealing shows changes in the XPS spectra of the top nanolayer in the TiO_2/SiO_2 nanolaminates. For the left section, the Ti 2p and O 1s signal remains similar to the as-deposited sample at annealing

temperatures up to 900°C. The Ti 2p doublet peak emerges after annealing at 1000°C for 10 hours, which indicates Ti cation diffusion into the top SiO_2 nanolayer. The O 1s peak fitting supports the contribution from emerging Ti^{4+} species (Fig. 3.5). For the right section, the Si 2p and O 1s signal remains similar to the as-deposited sample at annealing temperatures up to 800°C. The Si 2p peak emerges after annealing to 900°C for 10 hours, which indicates Si cation diffusion into the top TiO_2 nanolayer. Annealing to 1000°C, shows an additional ~8 % increase in Si cation content within the TiO_2 nanolayer and an increase in Si^{4+} species. The cation content can be seen in Figure. 3.10.

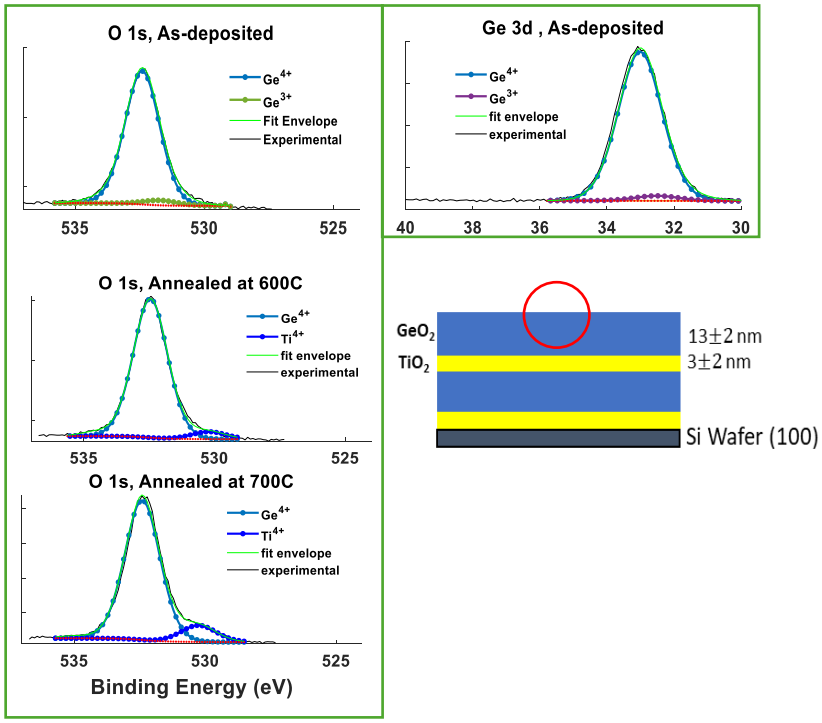

Figure 3.2: XPS spectra for O 1s and Ge 3d signatures of the GeO2/TiO2 nanolaminate's top nanolayer for as deposited, and after annealing for a soaking period of 10 hours at 600°C and 700°C. Ge 3d remained fully oxidized after annealing (Red dotted line is the fitting baseline).

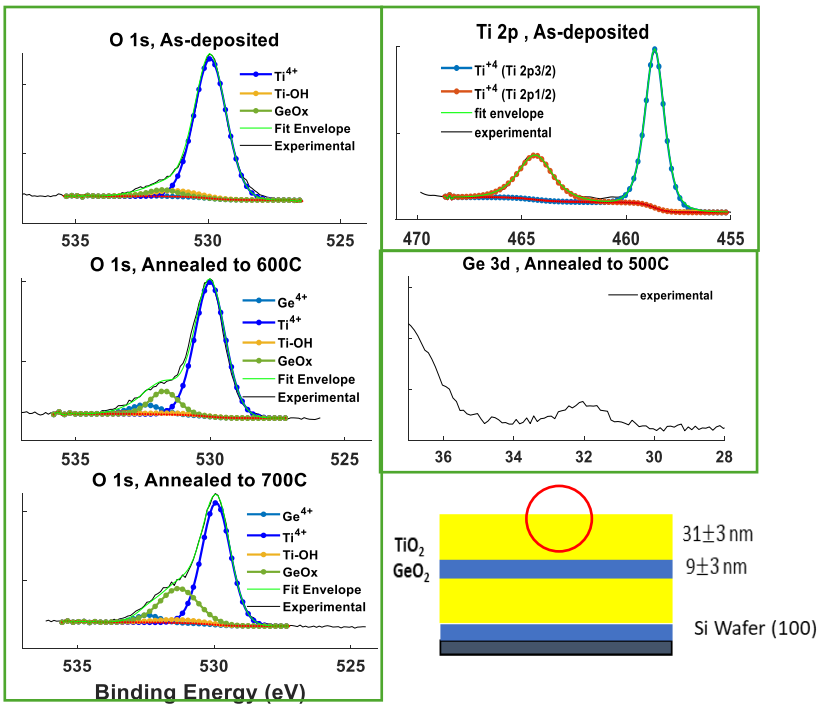

Figure 3.3: XPS spectra for O 1s, and Ti 2p of the GeO2/TiO2 nanolaminate's top nanolayer for as deposited, and after annealing for a soaking period of 10 hours at 600°C and 700°C. Ge 3d for annealing temperature of 500°C is shown. Ti 2p remained fully oxidized after annealing. (Red dotted line is the fitting baseline).

X-ray diffraction patterns of the GeO_2/TiO_2 nanolaminates are shown in Figure. 3.7, for as deposited and after annealing at 500°C, 600°C and 700°C for 10 hours. Similarly, the X-ray diffraction patterns for the TiO_2/SiO_2 nanolaminates are shown in Figure. 3.8, for as deposited and after annealing at 600°C, 800°C, 900°C, and 1000°C for 10 hours. For the GeO_2/TiO_2 nanolaminates, onset of crystallization in the TiO_2 anatase phase is detected after annealing at 700°C and corresponds to the (112) plane.

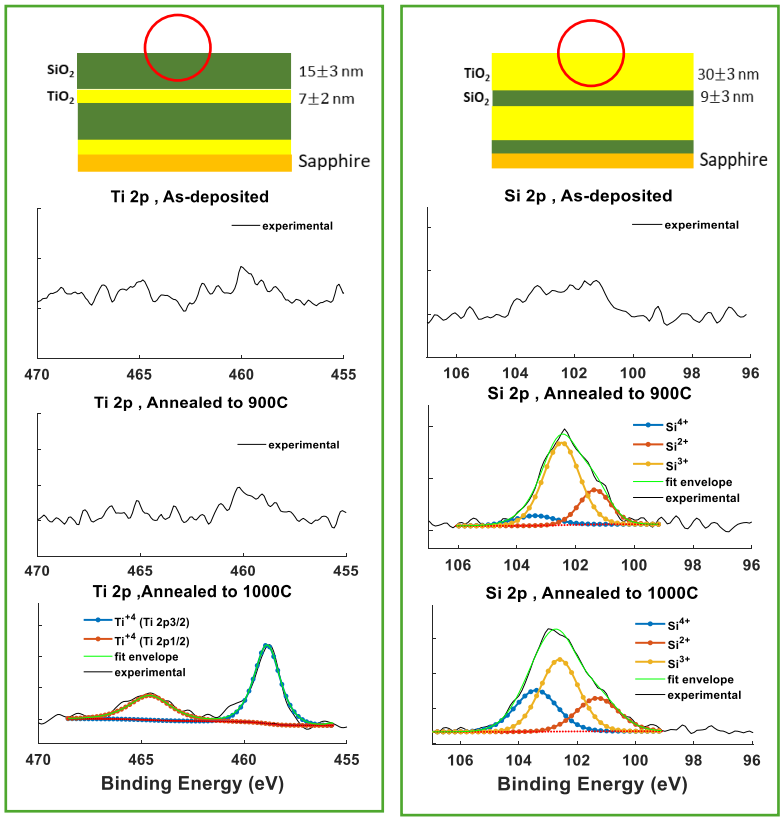

Figure 3.4. XPS measurements of Ti 2p and Si 2p peaks of the SiO_2/TiO_2 nanolaminate's top nanolayer annealed for a soaking period of 10 hours at 900C and 1000C.

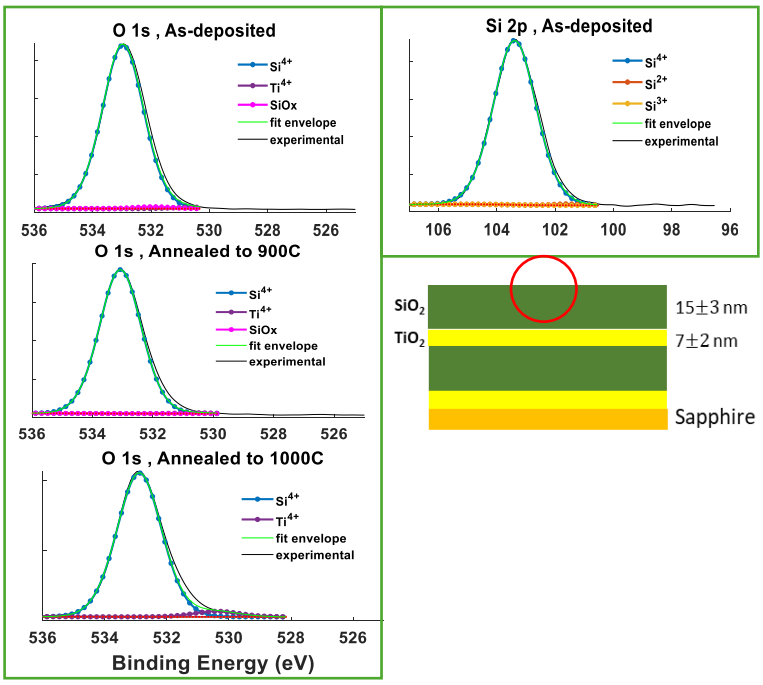

Figure 3.5: XPS spectra for O 1s, and Si 2p of the SiO2/TiO2 nanolaminate's top nanolayer for as deposited, and after annealing for a soaking period of 10 hours at 900°C and 1000°C. Si 2p remained fully oxidized after annealing (Red dotted line is the fitting baseline)

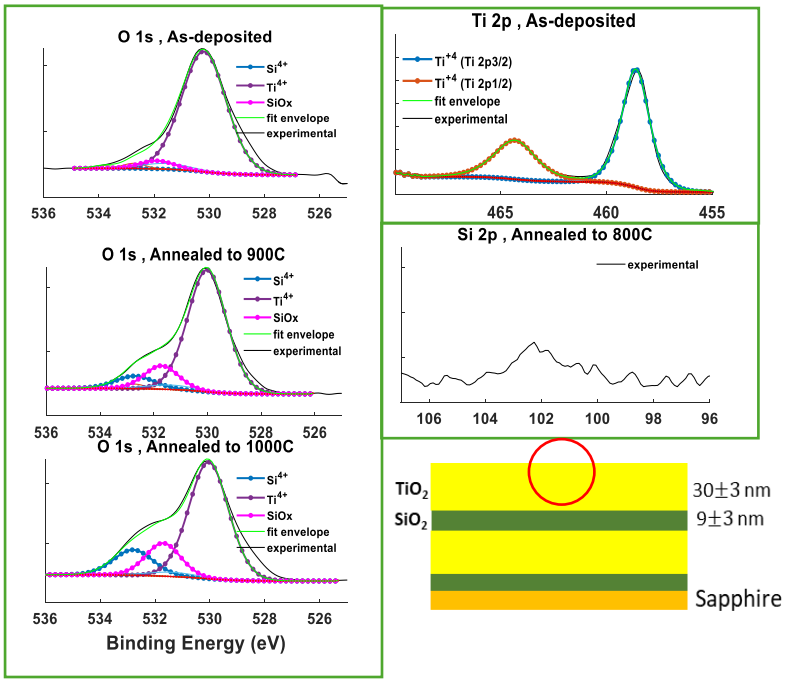

Figure 3.6: XPS spectra for O 1s, and Ti 2p of the SiO2/TiO2 nanolaminate's top nanolayer for as deposited, and after annealing for a soaking period of 10 hours at 900°C and 1000°C. Si 2p for annealing temperature of 800°C is shown. Ti 2p remained fully oxidized after annealing. (Red dotted line is the fitting baseline).

The temperature for incipient crystallization of the TiO_2 nanolaminate is delayed to a higher annealing temperature between 600°C and 700°C in comparison to the TiO_2/SiO_2 nanolaminates that show diffraction peaks after annealing at 600°C. This is because the reduced TiO_2 thickness in the GeO_2/TiO_2 nanolaminates affects the crystallization threshold as a result of a higher surface-area-to-volume-ratio contribution to the Gibbs free energy. [88,95] The TiO_2/SiO_2 nanolaminates show onset of crystallization after annealing at 600°C. The (101), (112), and (200) planes corresponding to the TiO_2 anatase phase are detected after annealing at 600°C, and 800°C. In addition, the (110), and (210) planes corresponding to the TiO_2 rutile phase appear after annealing at 900°C. This structural change in TiO_2 has been reported in TiO_2/SiO_2 alternating layered films with equal thicknesses of 6.5 nm.[96] Using

Scherrer's equation [97], the crystallite size obtained from the full width half maximum of the (112) plane anatase diffraction peak of the TiO_2/SiO_2 nanolaminates after annealing at 900°C is calculated to be ~10.6 nm, which is the same as the thickness of the as-deposited TiO_2. After annealing to 1000°C the thickness is calculated to be ~ 15 nm. This exceeds the initial nanolaminate thickness and suggests that the interface has been destroyed as a result of TiO_2 diffusion to form a larger crystal. This agrees with the results obtained by Le et.al using TiO_2/Ta_2O_5 nanolaminates. [94] Moreover, spectrophotometry was conducted on the TiO_2/GeO_2 nanolaminates with the same design as the XRD samples. The measurements revealed a change after annealing to 600°C, providing additional evidence of structural alteration in the film due to interdiffusion. This is illustrated in Figure 3.9.

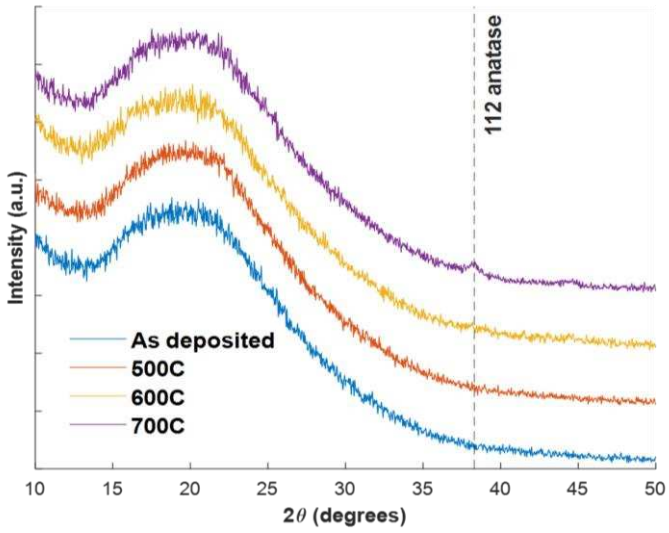

Figure 3.7. X-ray diffraction patterns of the GeO_2/TiO_2 nanolaminates, for as deposited and annealed at 500°C, 600°C and 700°C for 10 hours.

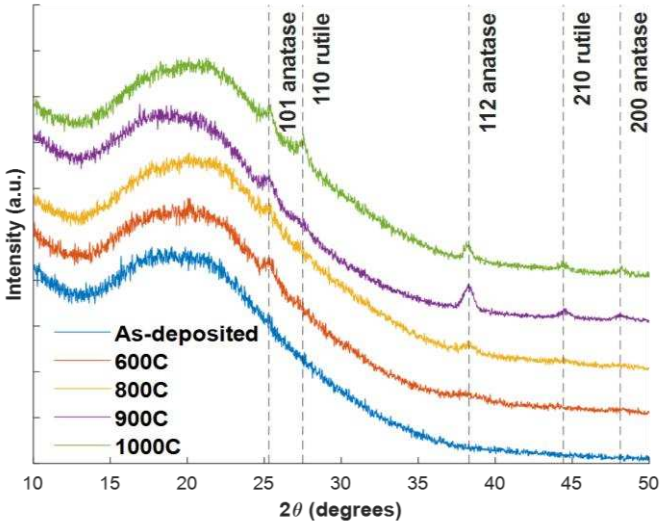

Figure 3.8. X-ray diffraction patterns of the TiO_2/SiO_2 nanolaminates, for as deposited and annealed at 600°C, 800°C and 900°C and 1000°C for 10 hours.

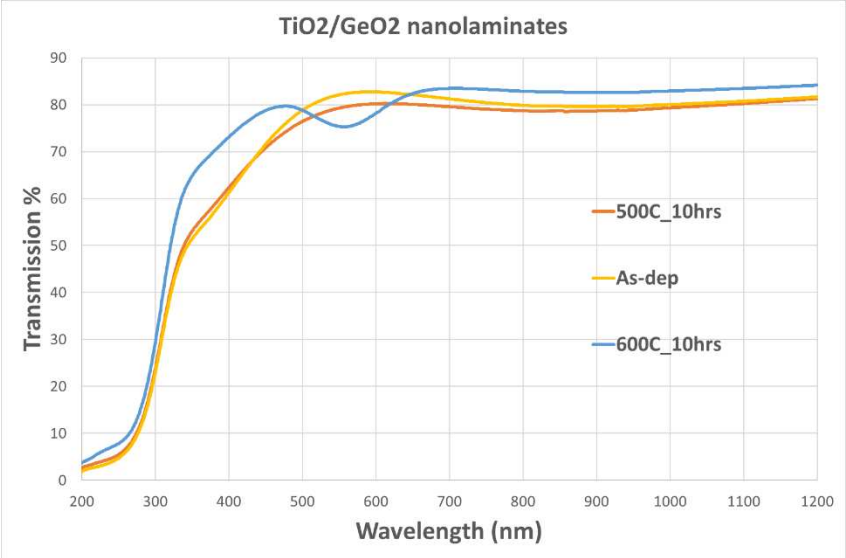

Figure 3.9. Spectrophotometry of TiO_2/GeO_2 nanolaminates (XRD sample design) after annealing to 500°C and 600°C.

These results show that for the GeO_2/TiO_2 nanolaminates, onset of cation interdiffusion occurs somewhere between an annealing temperature of 500°C and 600°C. Additional takeaways for diffusion are observed. As seen in Figure 3.1, on the left section, Ti cation diffusing into the GeO_2 network shows a peak energy separation of the emerged Ti 2p doublet as 5.86±0.02 eV which is greater than 5.7 eV

corresponding to a Ti $^{4+}$ species in pure TiO_2.[92] Similarly, a shift in the Ti $2p_{3/2}$ peak of 458.7 eV [92] in pure TiO_2 to about 459.6 eV is observed, which affirms a decrease in electron density. This can be attributed to the bonding interaction surrounding the titanium atom as a representation of an atomic mixture. These modifications to the XPS spectra result indicate atomic mixing, that is Ti-O-Ge bonds are forming. A similar energy separation in the Ti 2p doublet peak has also been observed after intermixing occurred between Ta_2O_5/TiO_2 nanolaminates upon annealing at 650°C. [94] and in a Ta_2O_5:TiO_2 single layer mixture upon annealing at a lower temperature of 300°C. [93] In contrast, the Ge cation diffuses within the TiO_2 nanolayer in a reduced oxidation state, as seen in the emerged Ge 3d peak (Fig. 3.1, right), which can be attributed to the large negative Gibbs free energy of formation for TiO_2 in comparison to GeO_2. [104] Nevertheless, the diffraction patterns show that the nanolaminates retain their amorphous structure due to a thinner TiO_2 and are also in a mixed state after annealing at 600°C.

For the TiO_2/SiO_2 nanolaminates, cation interdiffusion is not symmetrical, Si cation diffusion into the TiO_2 nanolayer occurs somewhere between 800°C and 900°C. As seen in the GeO_2/TiO_2 nanolaminates, the Si cation diffuses in a reduced oxidation state of Si^{4+}, and SiO_x as shown in the Si 2p (Fig. 3.4, right) and O 1s peaks (See Fig. 3.6) This can also be attributed to TiO_2 having a large negative Gibbs free energy of formation compared to SiO_2. [104] The onset of Ti cation diffusion into the SiO_2 nanolayer occurs between 900°C and 1000°C. In this case, the Ti 2p doublet peak energy separation is 5.7 eV which shows that the titanium is diffused but not interacting with the Si atoms. This can be credited to phase segregation due to a semi-crystallized TiO_2 nanolayer [93]. The diffraction patterns show that the nanolaminates start to crystallize after annealing at 600°C in the anatase phase. The asymmetry of

diffusion in the TiO_2/SiO_2 nanolaminate stack could be attributed to the larger ionic radius of Ti^{4+} (0.0605 nm, [106]) compared to Si^{4+}(0.04 nm, [106]). Instead, a more symmetrical diffusion can be seen in the GeO_2/TiO_2 nanolaminate stack due to a closer ionic radius between Ti^{4+} and Ge^{4+}(0.053 nm, [105]). Differences in ionic radius between metal oxides have been shown to play a role in the enabling/disabling of cation diffusion. [79,80] It is interesting to note that the onset of interdiffusion occurs in the annealing temperature range where TiO_2:GeO_2 (Ti 44%) and TiO_2:SiO_2 (Ti 69.5%) single layer mixtures in HR stacks were found to have the lowest mechanical loss [107, 108], in this case, after annealing at 600°C and 850°C for ~100 hours, respectively. This follows the same trend between a TiO_2:Ta_2O_5 single layer mixture and TiO_2/Ta_2O_5 nanolaminates. [94]

Amorphous SiO_2 and GeO_2 lack long-range order and are characterized by an atomic bonding network that follows a continuous random network with interconnected rings distributed throughout [109]. Ring size statistics have served as a metric for quantifying the degree of medium range order [99, 110, 111]. It has been noted that annealing closer to the Tg leads to a favorable thermodynamic reorganization in the range order for both amorphous GeO_2 and SiO_2. It is instructive to plot the results of this work in terms of the ratio of the annealing temperature (T_{an}) with Tg, where Tg is taken equal to 606 °C for a-GeO_2 and 1187°C for a-SiO_2. [91] In Figure.3.10, cation interdiffusion takes place just before the temperature range corresponding to the glass transition (Tg) of the network-forming oxides in the nanolaminates. This corresponds on average to 0.81 of the Tg. Additionally, it has been noted that annealing closer to the Tg leads to a favorable thermodynamic reorganization in the range order for both amorphous GeO_2 and SiO_2. In a study [98], annealing amorphous GeO_2 close to 500°C for 10 hours results in a 72% increase in

the population of six-membered rings within the film. This indicates an enhancement in the medium-range order for amorphous GeO_2.

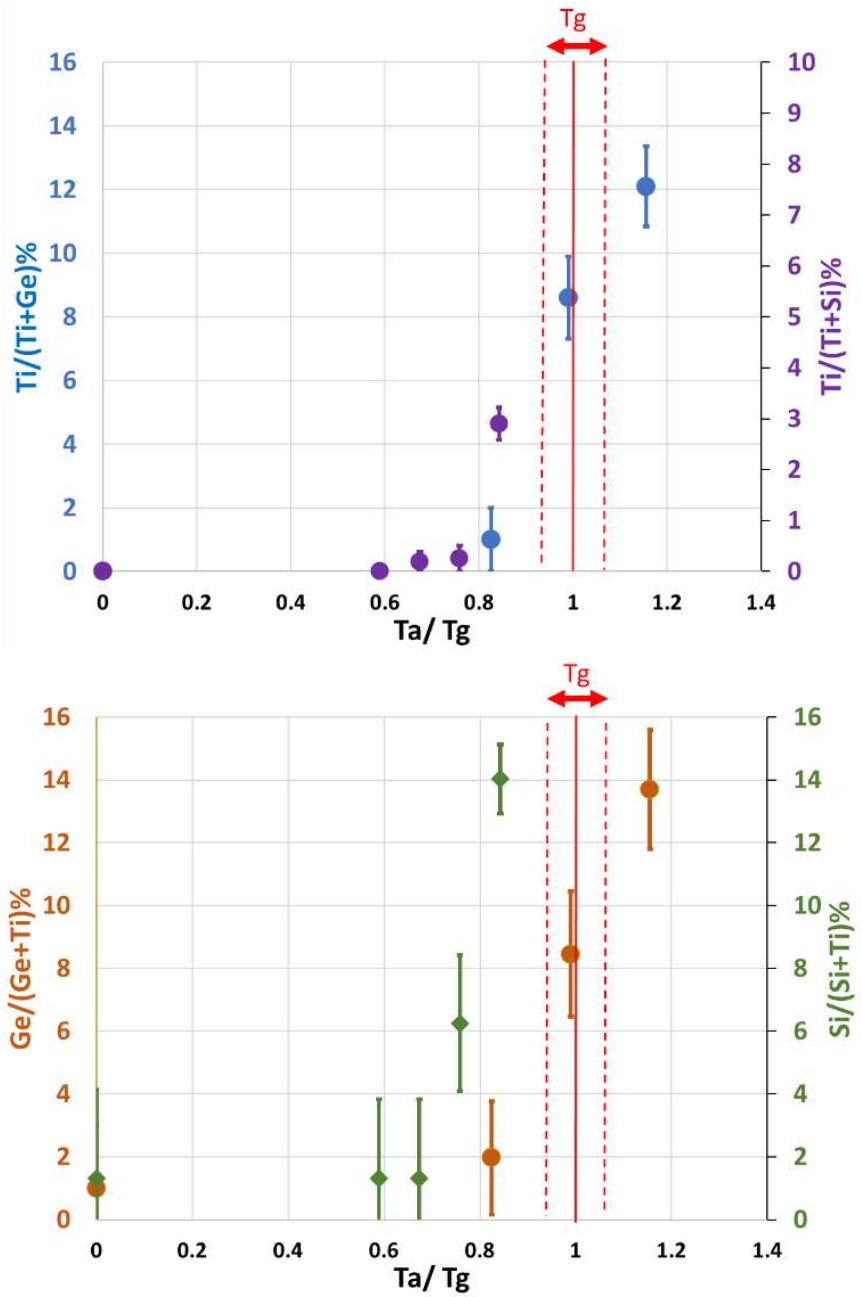

Figure 3.10 Ti cation % of the GeO_2/TiO_2 and TiO_2/SiO_2 nanolaminates and Ge/Si cation % of the GeO_2/TiO_2 and TiO_2/SiO_2 nanolaminates as a function of annealing temperature (Ta) divided by the glass transition temperature (Tg) of GeO_2 and SiO_2.

Similarly, research on SiO_2 glass in [100] from IR reflectance measurements reveal structural relaxations after annealing close to 900°C indicating an increase in bond

angle for Si-O-Si. Molecular dynamic simulations validate the experimental results, shown as 50% reduction in 3 and 4-membered rings following rapid annealing at around 1027°C, contributing to an increase in the medium-range order. [99] Similarly, in-situ neutron total scattering measurements unveil a decrease in ring size of 4 or fewer for fused silica highlighted after annealing at 950°C [112]. Interestingly, experimental, and simulated data shows growth in ring size as a means to enhance atomic integration into the amorphous silica network [101, 102, 113, 114, 117]. Nonetheless, the dissociation of bonds that drives the reorganization towards larger ring size distributions within the GNF could potentially activate the interdiffusion mechanism with TiO_2 at the interface. Hence, the structural relaxations as transitions from short to medium range order close to the Tg of the glass network former, as well as influences from varying ionic radius from the different oxides could conceivably exert an influence on the interdiffusion mechanism.

3.4 Conclusion

This study demonstrates that cation interdiffusion takes place between amorphous oxides of TiO_2 with GeO_2, and SiO_2 near the glass transition temperature (Tg) of the GNF in the nanolaminate stack. The observed increase in the ring size of the GNF upon annealing, as documented in literature, along with differences in ionic radii, may have a potential influence on the initiation of interdiffusion. Interestingly, the temperature range within which interdiffusion occurs aligns with previously reported low mechanical loss values observed in single-layer TiO_2 films mixed with GeO_2 or SiO_2 used in mirrors for gravitational wave detection. This observation is consistent with mechanical loss findings involving TiO_2/Ta_2O_5 nanolaminates and its mixed form upon annealing.

Chapter 4

Investigation on the structural, mechanical and optical properties of ternary amorphous oxides of TiO_2:GeO_2 with SiO_2 and ZrO_2 and TiO_2:SiO_2:ZrO_2

Present and future laser interferometric gravitational wave detectors require increased sensitivity in the mid-frequency range (~50 – 400 Hz), as the cavity suspended test mass mirrors are fundamentally affected by noise contributions arising from thermally driven fluctuations in the amorphous coatings, known as Brownian motion. Reducing Brownian thermal noise is crucial for achieving higher sensitivity, and this has been demonstrated to occur after annealing. Towards the goal of reducing coating thermal noise in TiO_2:GeO_2 (44% Ti) below its present low record of 0.67 aLIGO, ternary alloys of TiO_2:GeO_2:SiO_2, TiO_2:GeO_2:ZrO_2, and TiO_2:SiO_2:ZrO_2 with ~12% SiO_2 or ZrO_2 were deposited by ion beam sputtering. TiO_2:SiO_2 (69.5% Ti) is also another candidate with low thermal noise after annealing. The residual stress, optical absorption, and crystallization behavior with annealing were evaluated. The addition of ~12% of SiO_2 or ZrO_2 is demonstrated to enhance the stability of the amorphous structure of the ternary oxides to higher annealing temperatures when compared to its binary counterpart. Furthermore, adding ZrO_2 leads to higher residual tensile stress when compared to adding SiO_2.

4.1 Introduction

Detecting gravitational waves provides unique insight into extreme astrophysical phenomena, such as black hole mergers [118], neutron star collisions [119], and much

more. However, the gravitational waves as spacetime distortions felt on earth are extremely small (~10^{-18} m or less, [44]) and thus, require highly sensitive detectors. State-of-the-art detectors, such as the Advance Laser Interferometer Gravitational Wave Observatory (a-LIGO) consisting of 4-km arm length Michelson interferometer with Fabry-Perot cavities were built to capture these minute displacements. Still, current limitations for a more frequent and sensitive detection are partly due to noise contributions in the mid-frequency range (~50 – 400 Hz), where quantum and thermal noises are present. [45] Thermal noise can be predominantly attributed to the thermally driven random displacement fluctuations, referred to as Brownian motion, within the suspended mirror amorphous optical coatings in the interferometer. This motion associates with a damping effect as internal friction, acting as an anelastic relaxation mechanism by dissipating energy after each cycle of oscillation. The internal friction can be quantified by the mechanical loss angle (Q^{-1}). [52] Extensive research has been conducted to reduce mechanical loss. Currently, Ta_2O_5:TiO_2 (27% Ti) acts as the high index layer and is known to contribute more to thermal noise, with a single layer mechanical loss of ~2.4 x 10^{-4}. Other binary amorphous oxide mixtures, such as TiO_2:GeO_2 (44% Ti) and TiO_2:SiO_2 (69.5% Ti), represent promising candidates for the high-index coating layer for the next LIGO detector upgrade (Advanced LIGO A+) for its reduced contribution of coating thermal noise (CTN). This consists of 0.67-0.69 of aLIGO (~6.3x10^{-21} m/$Hz^{-1/2}$) after annealing to 600°C for TiO2:GeO2 with SiO2 HR stack [62], and 0.76 of aLIGO after annealing to 850°C for TiO2/SiO2 with SiO2 HR stack. Nonetheless, crystallization occurs at approximately 550°C [63], and there is an

emergence of blisters and cracking, which may be contingent on the specific process utilized for deposition. [64]

Following the observation that in TiO_2:GeO_2, and TiO_2:SiO_2 , the mechanical loss for a high index material reduces with the addition of Ti to a-GeO_2 and a-SiO_2, I synthesized thin film amorphous oxide samples containing a third cation. Exploring the individual contributions, such as of pure SiO_2, known to have the lowest mechanical loss with a low index of 1.47 at a wavelength of 1064 nm. Similarly, the other attractive candidate is ZrO_2, known to have a low mechanical loss ($3x10^{-4}$, at 1kHz) among the high index materials with an index of 2.2. However, ZrO_2 has around 4 times the Young's modulus of SiO_2, a large mismatch would increase coating thermal noise. (See Eq. 1.9) Adding both SiO_2 and ZrO_2 have shown improvements in the crystallization threshold from 600°C up to 750°C and 800°C, respectively, when mixed with Ta_2O_5. [15] Annealing has also shown a network reorganization when adding ZrO_2 to Ta_2O_5, attributed to a majority of corner-shared polyhedral bonds. [129]Moreover, incorporation of ZrO_2 into Ta_2O_5:TiO_2 has been investigated with different compositions, main results showed an increase in the crystallization temperature by more than 150°C from a binary mixture of Ta_2O_5:TiO_2 (~27% Ti), and a reduction of mechanical loss by a factor of 1.5 of Advanced LIGO. However, cracking issues appear before crystallization. [120]

In this study, the structural properties of ternary amorphous oxide mixtures comprising TiO_2:GeO_2:SiO_2, TiO_2:GeO_2:ZrO_2, and TiO_2:SiO_2:ZrO_2 grown through ion beam sputtering were investigated. Annealing was conducted at soaking temperatures of 600°C, 700°C, and 800°C for 10 hours in air. Subsequently, investigation of the

thickness, refractive index, residual stress, optical absorption, and crystallization were performed post-annealing. The results indicate a delayed onset of crystallization for all four ternary samples compared to the binary oxides. TiO_2:GeO_2:SiO_2 and TiO_2:GeO_2:ZrO_2 exhibit a weak diffraction intensity, with incipient crystallization observed after annealing to 800°C. On the other hand, TiO_2:SiO_2:ZrO_2 remains amorphous up to 800°C. However, this alloy experiences tensile stress failure, evidenced by coating cracking after annealing at 700°C.

The quarter-wavelength optical absorption at λ=1064 nm remains approximately 3.7 +/- 0.7 ppm after annealing at 700°C for all ternary oxides. A 1.6 reduction is seen for TiO_2:GeO_2 based ternaries after annealing at 800°C. Furthermore, all ternary oxides exhibit a shift in residual stress towards tensile behavior. TiO_2:GeO_2:SiO_2 demonstrates the lowest shift in residual stress, achieving a 467 MPa stress increment after annealing at 700°C, while TiO_2:SiO_2:ZrO_2 with higher Ti content exhibits the maximum residual stress, reaching around 870 MPa increments after annealing at 700°C. In addition, residual stress is studied for pure ZrO_2, SiO_2, as well as binary oxide mixtures consisting of TiO_2:GeO_2 and TiO_2:SiO_2.

4.2 Experimental Methods

Amorphous ternary oxide mixtures were synthesized through the reactive biased target ion beam deposition technique utilizing a LANS system manufactured by 4Wave.Inc.[103], process shown in section 2.1.1. -900 V used for sputtering. High-purity grade oxygen at a flow rate of 16 sccm was introduced into the chamber close to the substrate to promote the growth of ternary oxides, maintaining an initial chamber base pressure of approximately ~5×10^{-8} Torr. The deposition temperature for each sample

was maintained at around 100°C.

The design criteria for the ternary oxide single-layer mixture encompassed achieving a high index at 1064 nm (n>1.87) similar to that of TiO_2:GeO_2 which demonstrated the lowest mechanical loss. [30] Furthermore, specifications included ensuring low absorption in as-deposited films (<10 ppm), a thickness exceeding 170 nm, and restricting the added percentages of Si and Zr to below 14%.

X-ray Photoelectron Spectroscopy (XPS) was performed on the as-deposited samples to determine the cation composition estimates. XPS technique shown in section 2.2.2. The cation compositions were estimated using the Si 2p, Ge 3d, Ti 2p, and Zr 3d orbitals. Table 4.1 presents the pulse width (positive bias time) and deposition rate, corresponding to the displayed composition average estimation of different samples grown.

Table 4.1. Deposition conditions on each metal target operated simultaneously. The pulse period used was of 100 µs for the Si and Ge targets, 20 µs was used for the Ti target. Binary oxides and ZrO_2 used 12 sccm of O_2. SiO_2 used 4sccm of O_2.
d.p stands for different target positions.

Mixture	Target	Pulse Width (µs)	Deposition Rate (nm/s)	Average cation % estimate (as deposited)
TiO_2:GeO_2:ZrO_2 (**1**)	Ti/Ge/Zr	3/94/99	0.0066±0.0002	44.2±0.5/ 44±1.4/ 11.8±0.9
TiO_2:GeO_2:SiO_2 (**2**)	Ti/Ge/Si	3/95/94	0.0076±0.0002	50.2±1.4/ 37.8±0.9/ 12±0.6
TiO_2:SiO_2:ZrO_2 (**3**)	Ti/Si/Zr	3/91/96	0.0061±0.0002	59±0.9/ 27.7±0.8/ 13.3±0.4
TiO_2:SiO_2:ZrO_2 (**4**)	Ti/Si/Zr	2/92/96	0.006±0.0002	62±1/ 25.2±1.6/ 12.7±0.5
TiO_2:GeO_2 (**5**)	Ti/Ge	2/89	0.0096±0.0002	~42/58
TiO_2:GeO_2 (**6**)	Ti/Ge	2/88 (d.p)	0.0087±0.0002	~45/55

TiO_2:SiO_2 (**7**)	Ti/Si	2/85	0.0072±0.0002	~62/38
SiO_2 (**8**)	Si	50	0.024±0.0002	100
ZrO_2 (**9**)	Zr	2	0.01±0.0002	100

In general, the oxides would be deposited on a Si (100) wafer for Grazing Incidence X-ray Diffraction (GIXRD) and XPS measurements. A 25.4 mm diameter, 1 mm thick UV fused silica substrate is utilized for stress measurements, while a 6.35 mm thick UV fused silica substrate is employed for optical absorption measurements. Furthermore, consecutive annealing steps were conducted on each sample in air at temperatures of 600°C, 700°C, and 800°C for 10 hours for the ternary oxides, with a ramp rate of 0.8°C/min using a Fisher Scientific Isotemp programmable furnace. The same procedure done for the binary and single material oxides at 400°C, 500°C, 600°C, and 700°C with a ramp rate of 1°C/min. Grazing Incidence X-ray Diffraction measurements were performed utilizing an X-ray Diffractometer PANalytical X'Pert system equipped with a Cu-Kα X-ray tube source. A fixed incidence angle (θ) of 3.5° from the surface was maintained, with scanning regions between 10 to 50° of 2θ, where θ represents the angle between the incident beam and the diffracted beam.

The optical absorption loss at 1064 nm for each ternary sample before and after annealing was measured using photothermal common-path interferometry. [73] The radius of curvature was measured using the carrier frequency interferometry [75] technique before, after deposition, and after annealing. Stoney's equation (See Eq. 2.13) was then applied to calculate the residual stress. Thickness and refractive index were

determined using UVISEL Horiba spectroscopy ellipsometry with an incidence angle of 60° in the spectral range of 1eV to 5 eV. The fitting of ellipsometric data was performed using the DeltaPsi software employing a Tauc-Lorentz three oscillator dispersion model for the ternary and binary oxides. A Cauchy and classical oscillator dispersion model were used for SiO_2 and ZrO_2, respectively.

4.3 Results and Discussions

The crystallization onset was investigated after annealing at 700°C and 800°C, as illustrated in Figure 4.1. In TiO_2:GeO_2 based ternary mixtures, the addition of both SiO_2 and ZrO_2 enhances the amorphous structure up to annealing at 700°C. This is higher than a single layer of TiO_2:GeO_2 (~44% Ti) grown (see Fig 4.2.), as well as, reported [123] After annealing to 800°C, a weak diffraction peak corresponding to the (101) plane for TiO_2 anatase was observed in both samples. The peak area was more pronounced in the ZrO_2-doped sample (1), potentially indicating an earlier incipient crystallization between annealing temperatures of 700°C and 800°C, compared to the SiO2-doped sample (2). Conversely, for both TiO_2:SiO_2:ZrO_2 mixtures, no diffraction peaks were observed even after annealing to 800°C. Sputtered TiO_2:SiO_2 with around 60% Ti crystallizes at 600°C (see Fig 4.3). Nevertheless, the ternary mixtures presented in this study were selected from a group demonstrating a high crystallization onset. The latter was observed to decrease as a result of minor increments in Ti content, highlighting a high sensitivity to such alterations.

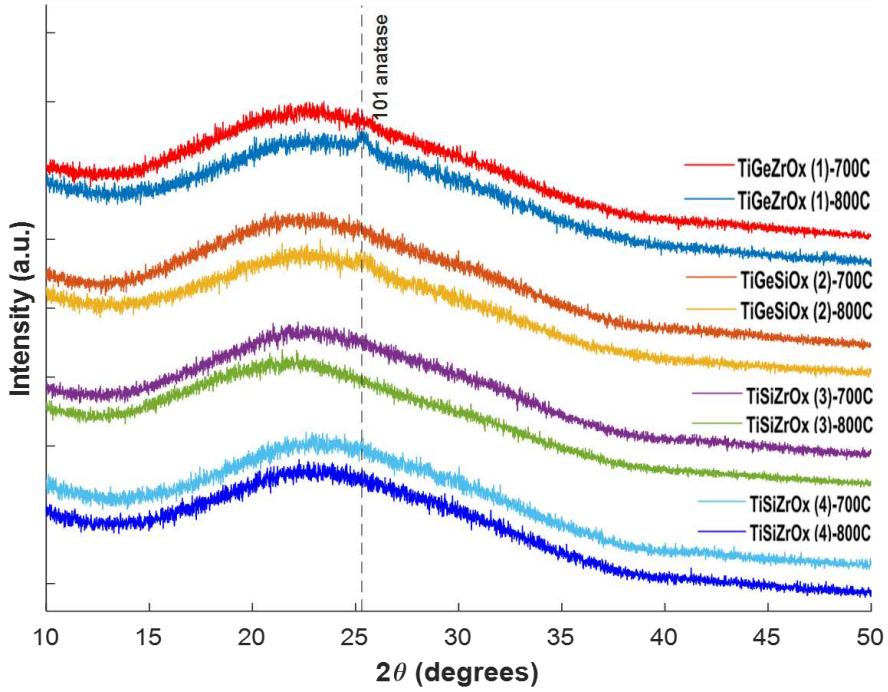

Figure 4.1. GIXRD measurements for ternary mixtures of TiO_2:GeO_2:SiO_2, TiO_2:GeO_2:ZrO_2, and TiO_2:SiO_2:ZrO_2

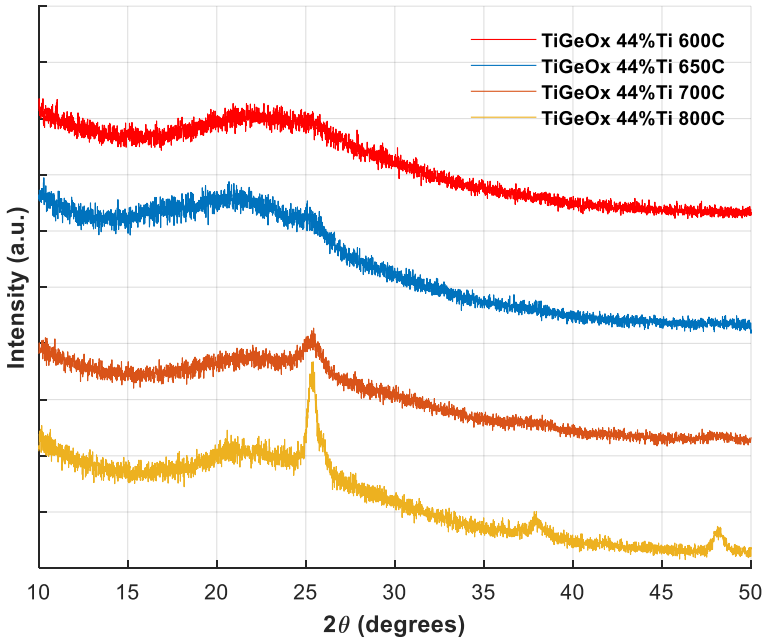

Figure 4.2: XRD of a single layer of TiO_2:GeO_2 with 44% Ti grown in the LANS. Crystallization visible after annealing to 700C.

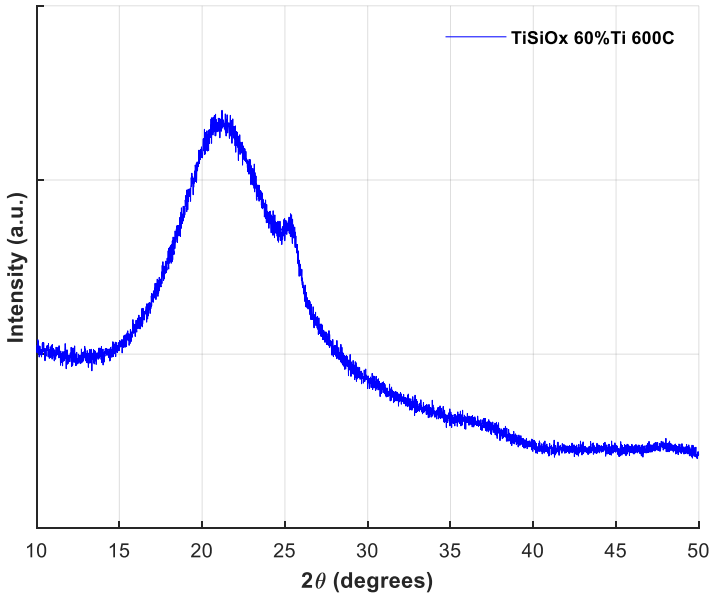

Figure 4.3: XRD measurement of a single layer of TiO_2:SiO_2 with around 60% Ti grown in the LANS, crystallized after annealing to 600C.

Figure 4.4 illustrates the residual stress contributions of TiO_2:GeO_2-based ternary compositions after annealing at 600°C, 700°C, and 800°C. Additionally, binary oxide mixtures are presented for 600°C and 700°C annealing temperatures. Furthermore, a TiO_2:GeO_2 single-layer mixture, comprising approximately 44% Ti, deposited at 60°C, is shown. It is evident that TiO_2:GeO_2:SiO_2 (2) exhibits the lowest tensile stress increment among all ternaries after annealing at 700°C and 800°C. In comparison to the binary oxides, the lower Ti content TiO_2:GeO_2 with approximately 42% Ti displays reduced tensile stress increments. Increasing the Ti content to approximately 45% achieves similar residual stress increments to TiO_2:GeO_2-based ternaries at 600°C; however, the binaries are known to crystallize at 700°C (see Fig 4.2). The reported value of TiO_2:GeO_2 with 44% Ti indicates higher stress increments at 600°C. Following stress relaxation after annealing at 800°C, the surface of the TiO_2:GeO_2:ZrO_2 sample exhibits a "roughened" texture. (see Fig 4.7), not seen for TiO_2:GeO_2:SiO_2 after stress relaxation (see Fig. 4.8).

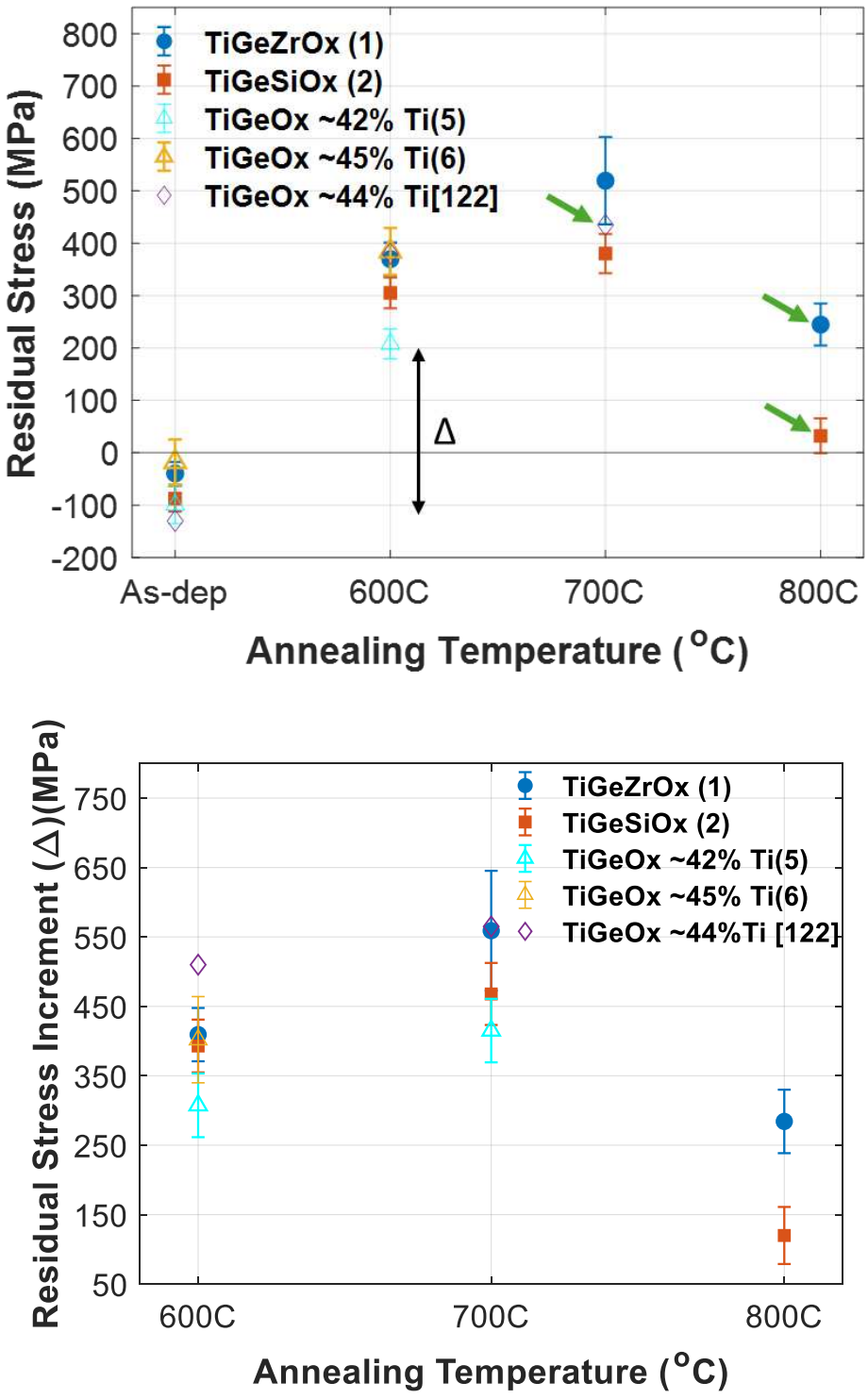

Figure 4.4: (Top)-Residual Stress with annealing of TiO_2:GeO_2 based ternaries and binaries. (Bottom)- Residual Stress increment (Δ) with annealing. Green Arrow indicates X-ray diffraction peak is observed.

Figure 4.5 illustrates the residual stress contributions of the TiO_2:SiO_2-based ternary mixtures annealed at 600°C, 700°C, and 800°C. A TiO_2:SiO_2 binary mixture containing approximately 62% Ti is shown. Additionally, reported TiO_2:SiO_2 single-layer mixture with approximately 69.5% Ti, grown at Laboratoire des Matériaux Avancés (LMA) is presented. The film has a thickness of approximately 500 nm, with an annealing ramp rate of about 0.83°C/min and a soak time of 10 hours [121]. Both TiO_2:SiO_2-based ternary oxides (3 and 4) exhibit lower stress increments after annealing at 600°C compared to the grown TiO_2:SiO_2 (7) and the reported single-layer TiO_2:SiO_2 [121]. Further annealing to 700°C, the TiO_2:SiO_2 ternaries increase by about 400 MPa of tensile residual stress. Despite these films displaying no incipient crystallization after annealing at 800°C, tensile failure is observed in the coating as propagated cracks after annealing at 700°C. (see Fig.4.6)

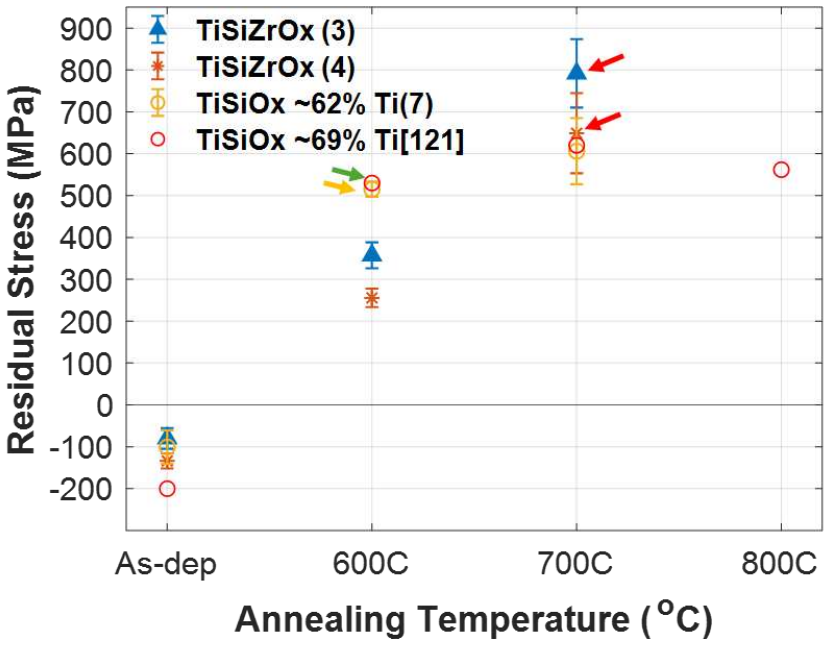

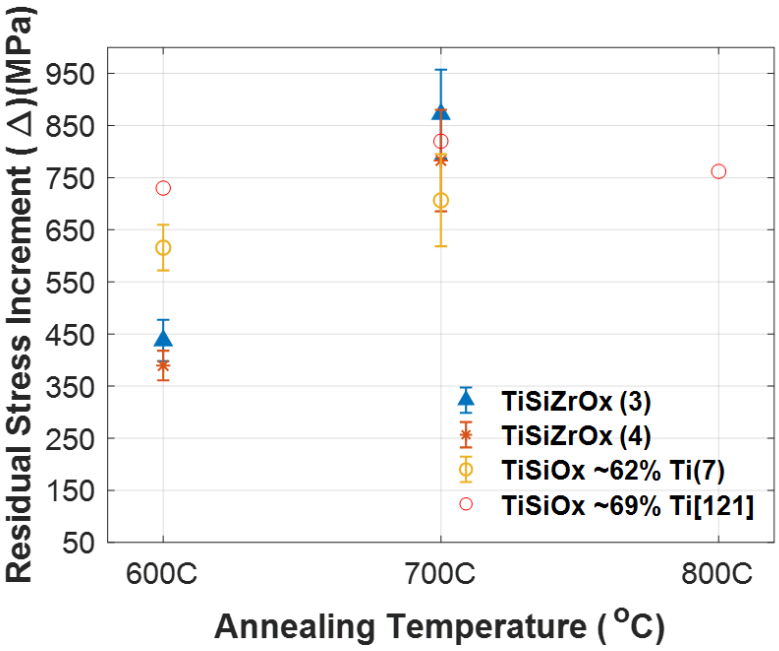

Figure 4.5: (Top)-Residual Stress with annealing of TiO_2:SiO_2 based ternaries and binaries. (Bottom)- Residual Stress increment (Δ) with annealing. Green Arrow indicates X-ray diffraction peak is observed. Red arrow indicates cracked film. Yellow arrow indicates known crystallized film.

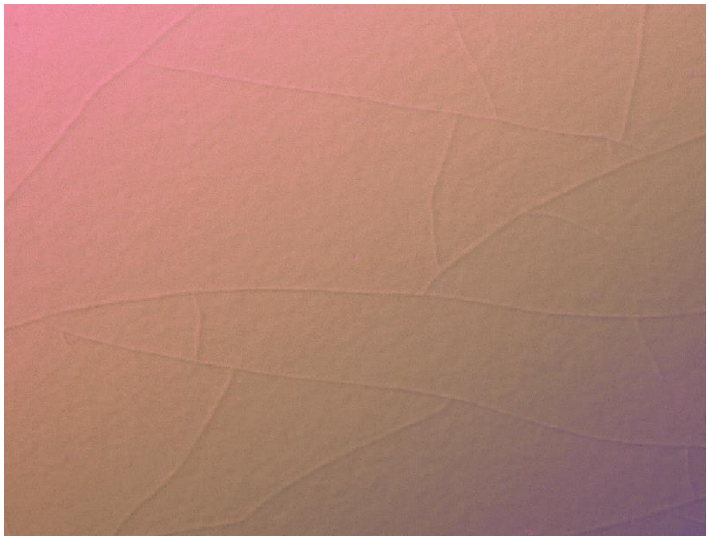

Figure 4.6: Surface image of TiO_2:SiO_2:ZrO_2 after annealing to 700C. Cracking is visible.

Figure 4.7: Surface image of TiO_2:GeO_2:ZrO_2 after annealing to 800C. Roughened surface is visible.

Figure 4.8: Surface image of TiO_2:GeO_2:SiO_2 after annealing to 800C. Pristine surface

Figure 4.9 presents the residual stress contributions for the binary mixtures of TiO_2:GeO_2, TiO_2:SiO_2, and pure materials of SiO_2 and ZrO_2 annealed at 400°C, 500°C, 600°C, and 700°C. Both SiO_2 and ZrO_2 exhibit compressive stress after deposition, as observed in all the ternary and binary mixtures. ZrO_2, however, demonstrates a notably

high compressive stress of approximately -1.7 GPa up to 600°C annealing, whereas SiO_2 registers around -100 MPa. Following annealing at 700°C, ZrO_2 experiences a shift of approximately 500 MPa towards more tensile stress, yet remains in compressive mode; similarly, SiO_2 undergoes a shift of approximately 75 MPa towards tensile stress while also remaining in compressive mode. Regarding the binary mixtures, as noted, TiO_2:GeO_2 with approximately 42% Ti exhibits lower tensile stress contributions compared to a higher content of 45% Ti at 600°C. A higher stress contribution is observed for TiO_2:SiO_2 (7) with 62% Ti.

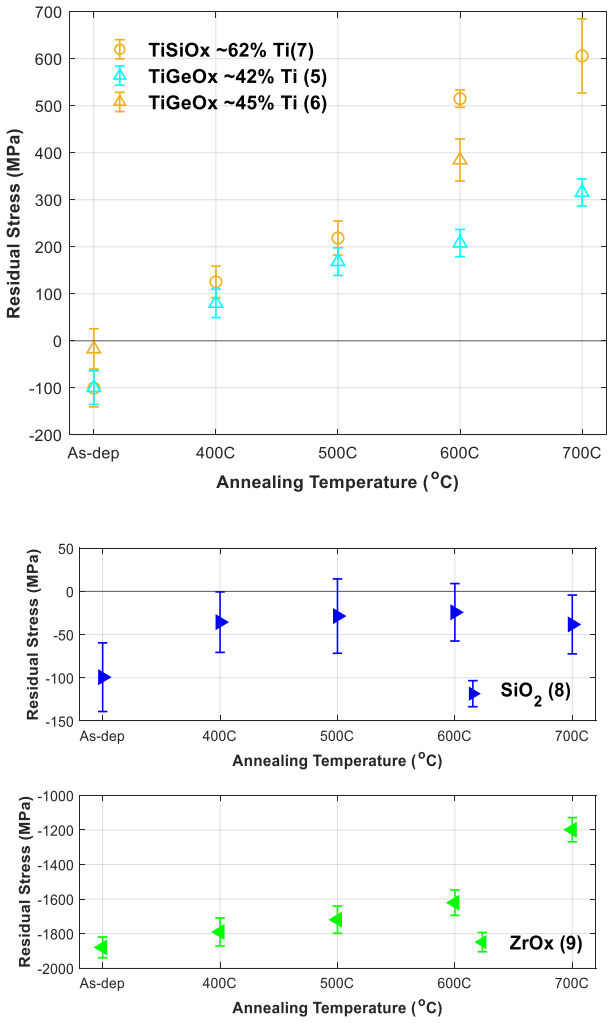

Figure. 4.9: (Top)- Residual Stress with annealing of TiO_2:GeO_2 and TiO_2:SiO_2 based binaries. (Bottom)- Residual stress with annealing of pure SiO_2 and ZrO_2.

Figure 4.10 depicts the optical absorption measurements normalized to quarter-wave thicknesses at 1064 nm for each ternary oxide single layer. Following annealing at 700°C, the optical absorption remains approximately at 3.7+/-0.7 ppm for all ternary oxides. For the TiO_2:GeO_2-based ternaries (1 and 2), the absorption reduces by a factor of 1.5 after annealing at 800°C to 2.45 +/- 0.5 ppm. A reported value of a single layer of TiO_2:GeO_2 with 44% Ti deposited in the LANS is plotted after 600°C annealing for ~10 hours [123]. Furthermore, an absorption spike is observed for the TiO_2:GeO_2:ZrO_2 sample (1) after annealing to 600°C, reaching 23 ppm and then dropping to around 4.2 ppm after annealing at 700°C. Deposition parameters such as oxygen flow may be adjusted to avoid the origin of defects or vacancies in this temperature region, leading to the spike.

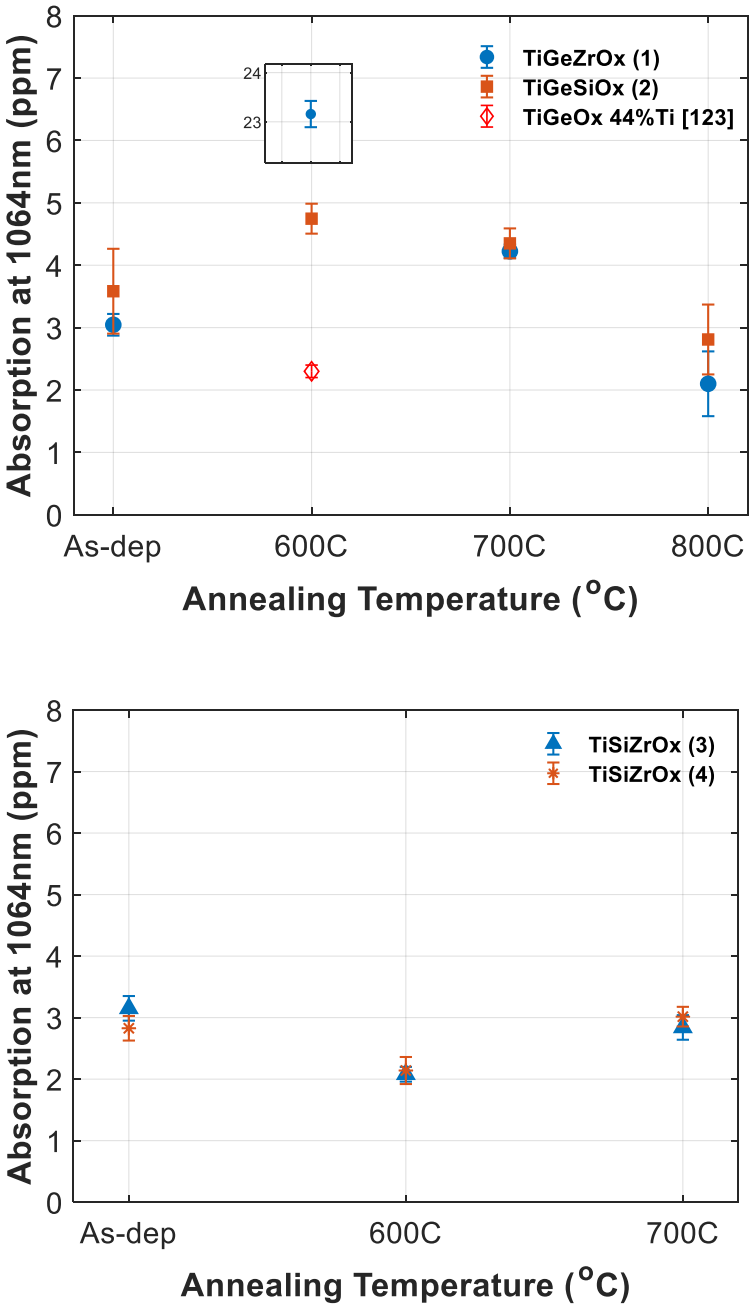

Figure 4.10. Absorption loss at 1064 nm with annealing for all ternaries.

Figure 4.11 presents normalized thicknesses and refractive indices at wavelength of 1064 nm for the ternary mixtures. The thickness for all samples in this study is approximately 198 +/- 10 nm. A reduction of 3% and 4.5% is observed in the thickness after 600°C of post-annealing for TiO_2:GeO_2:SiO_2 and TiO_2:GeO_2:ZrO_2, respectively.

Conversely, a 2.5% reduction is noted for the thickness after 600°C of post-annealing for both the TiO_2:SiO_2:ZrO_2 samples (3 and 4). In general, regarding the refractive index, a slight decrease is observed at 600°C followed by an increasing trend after annealing at 700°C.

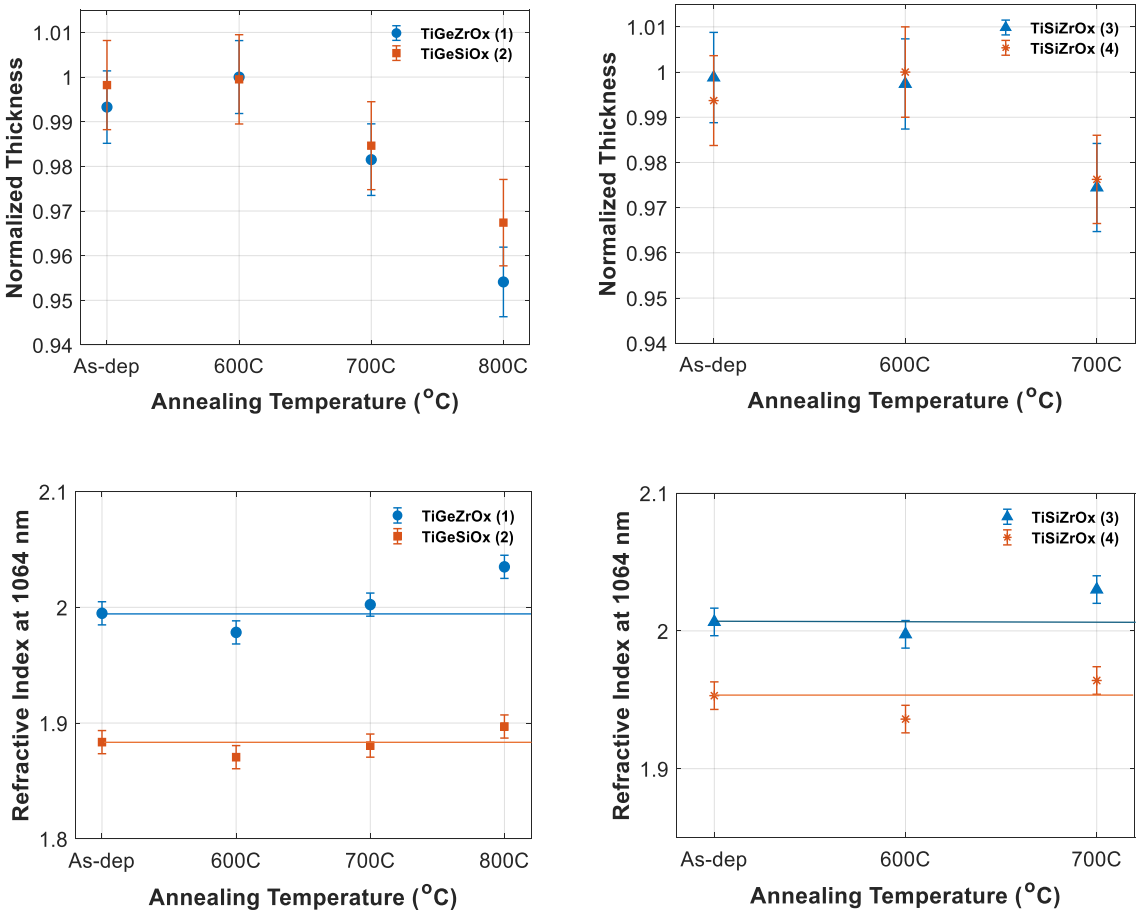

Figure 4.11. (Top)-Normalized thickness of ternaries with annealing. (Bottom)-Refractive index at 1064nm of ternaries.

Figure 4.12 depicts the changes in binary mixture thicknesses and refractive indices at 1064 nm with annealing. A notable decrease is observed for TiO_2:GeO_2 with 42% Ti (5), showing a reduction of 2.7% after 600°C of post-annealing, accompanied by an increase in the refractive index within the same temperature range. TiO_2:SiO_2 (7) remains unchanged in terms of both thickness and refractive index. As for the pure

materials, the thicknesses and refractive indices remain relatively constant after annealing to 600°C, with a refractive index of 1.47 for SiO_2 and 2.2 for ZrO_2 at a wavelength of 1064 nm. (not shown)

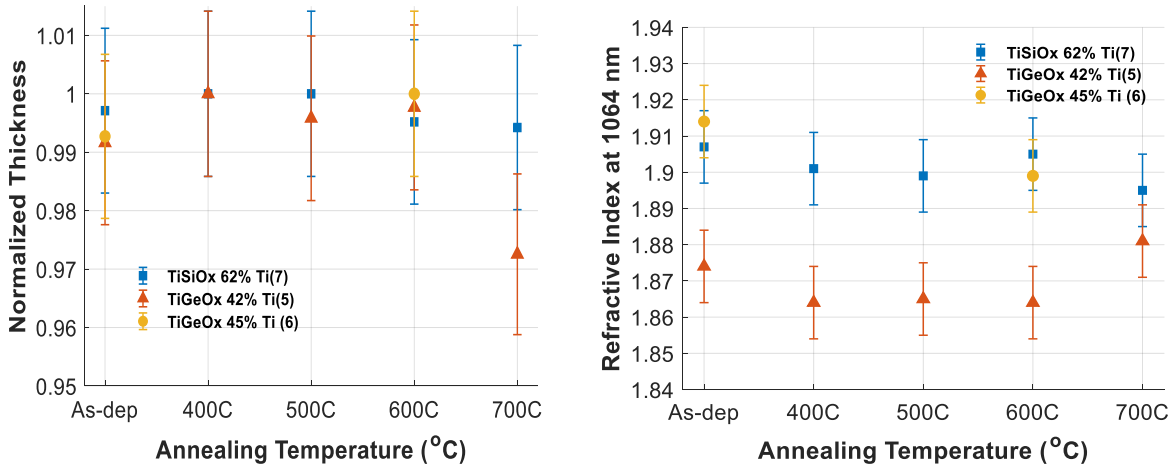

Figure 4.12. (Left)- Normalized thickness with thickness of binary mixtures. (Right)- Refractive index at 1064nm with annealing of binary mixtures.

These findings demonstrate that the addition of approximately 12% of SiO_2 or ZrO_2 stabilizes the amorphous structure of TiO_2:GeO_2 and TiO_2:SiO_2 up to annealing temperatures of 700°C and 800°C, respectively. Incipient crystallization in the anatase phase is observed after annealing to 800°C for TiO_2:GeO_2-based ternaries, further suggesting an earlier onset for the TiO_2:GeO_2:ZrO_2 sample between 700°C and 800°C, due to a more developed diffraction peak. The addition of Zr, which possesses the largest ionic radius in this study, is known to impede crystal growth by obstructing the amorphous base network due to its size and low mobility [124,125]. Conversely, SiO_2 is recognized as a 'strong glass' due to its strong chemical bonding with oxygen. Studies have shown that adding SiO_2 into Ta_2O_5 increases the crystallization temperature, attributed to the formation of a more rigid and stable network, thereby increasing the

coordination number of Ta-O while also reducing oxygen vacancies [126].

The residual stress increments for the TiO_2:GeO_2-based ternaries are observed to be lower when mixed with SiO_2 than with ZrO_2, a more pronounced difference after annealing to 700°C and above. Furthermore, the binary oxide mixture of TiO_2:GeO_2 with approximately 45% Ti shows similar residual stress contributions after annealing to 600°C as the ternaries, whereas the 42% Ti sample exhibits lower stress increments, even at 700°C. It appears that a higher Ti content leads to a greater tensile stress increment. Sputtered TiO_2 has been reported to have tensile stress and to further increase after annealing; attributed to phase transformation. [127] However, it is important to note that the TiO_2:GeO_2:SiO_2 ternary has lower residual stress contributions with higher Ti % than TiO_2:GeO_2:ZrO_2, which could indicate a greater individual contribution of SiO_2 to the coefficient of thermal expansion of the ternary film. Nevertheless, the TiO_2:GeO_2 with 44% Ti, grown in a different deposition system (Veeco Spector), shows greater tensile stress increments, attributed to being deposited at a lower deposition temperature of 60°C [122] After annealing to 800°C, the tensile stress reduces by ~274MPa for the TiO_2:GeO_2:ZrO_2 film, and ~347MPa for the TiO_2:GeO_2:ZrO_2 film. Stress relaxation is known to occur due to film failure such as cracking for a film that has excessive tensile stress. In this study, TiO_2:GeO_2:ZrO_2 exhibited a roughened surface after annealing to 800°C, suggesting a dislocation mechanism in the film resulting in relaxation. [21] Interestingly, TiO_2:GeO_2:SiO_2 showed no alteration in surface morphology, indicating that the latter was able to withstand deformation and followed a different pathway of relaxation.

For the TiO_2:SiO_2-based ternaries mixed with ZrO_2, increasing the TiO_2 content results in a greater tensile stress contribution, with the effect becoming more pronounced after annealing to 700°C. Both ternary films undergo tensile stress failure

as cracking after annealing to 800°C, which could be attributed to the high Ti content. Comparing between TiO_2:SiO_2-based ternaries and binaries, adding ZrO_2 seems to exert an influence on lowering the residual stresses at 600°C post annealing. On the other hand, between the binary mixtures, the same trend is seen where the sample with lower Ti content (62% vs 69% Ti) demonstrates lower tensile stress increment at 600°C and 700°C post-annealing. Overall, the TiO_2:SiO_2 ternaries and binaries demonstrate greater residual stress increments compared to the TiO_2:GeO_2-based ternaries at 700°C, with a higher Ti content in the TiO_2:SiO_2-based mixtures emerging as a potential factor. However, TiO_2:SiO_2 based ternaries at 600°C show similar stress behavior as TiO_2:GeO_2-based ternaries.

The measurements of thickness and refractive index suggest a densification restructuring occurring in all the ternaries after annealing between 600°C and 700°C. This densification, whether caused by vacancy annihilation or phase transformation, can be attributed to the generation of tensile stress. This stress arises from the attempt of the laterally constrained changing film to conform to the fused silica substrate. [21].

Regarding optical absorption, for the TiO_2:GeO_2-based ternaries, the absorption as deposited is approximately 3.2 ppm, indicating good stoichiometry. Through the annealing runs at 600°C and 700°C, the absorption increases to around 4.5 ppm, which remains consistent for TiO_2:GeO_2:SiO_2. However, for TiO_2:GeO_2:ZrO_2, a spike to around 23 ppm occurs at 600°C of annealing. Similarly, it can be observed that the film is less dense due to a reduction in refractive index and a slight increase in thickness. This suggests a state containing vacancy defects causing higher absorption. Adjusting

deposition parameters, such as oxygen flow or employing different annealing procedures, may be necessary to reduce the absorption spike.

For selection purposes, TiO_2:GeO_2:SiO_2 is the alloy that has the most prospects, as it does not crystallize to 800°C of annealing . It shows a lower rate of increase in tensile residual stress and did not exhibit signs of stress failure or surface morphology roughening after stress relaxation. However, one drawback of this sample is its low refractive index at 1064nm compared to the other films, which would hinder further reduction of the number of layers if implemented onto a Bragg reflector. TiO_2:GeO_2:ZrO_2 appears to be effective up to annealing temperatures ranging from 700°C to 800°C, before the occurrence of stress relaxation.

4.4 Conclusions

Incorporating approximately 12% amorphous ZrO_2 and SiO_2 into amorphous TiO_2:GeO_2 and TiO_2:SiO_2 respectively enhanced the stability of the binary counterpart, as its crystallization is 600C and 550C, to higher annealing temperatures of, 700°C and 800°C respectively. Moreover, SiO_2 appears to reduce the tensile stress increments when added to TiO_2:GeO_2, in contrast to ZrO_2, particularly at annealing temperatures beyond 600°C. Introducing ZrO_2 to TiO_2:SiO_2 seems to decrease the tensile stress contributions compared to a binary oxide mixture with similar Ti content after annealing at 600°C. However, it rises to stress increments equal to or greater than the binary mixture after 700°C. The observed densification in the ternary films after 600°C post-annealing leads to tensile stress behavior. Optical absorption is at its lowest for the TiO_2:GeO_2-based ternaries after annealing at 800°C, whereas for the TiO_2:SiO_2-based ternaries, it occurs at 600°C. TiO_2:GeO_2:SiO_2 exhibits the least change in stress, thickness, and refractive

index, and achieves low absorption at 800°C with insignificant levels of incipient crystallization, motivating further examination for mechanical loss. Similarly, TiO_2:GeO_2:ZrO_2 proves useful in annealing temperatures between 700°C and 800°C, despite the failure modes observed after stress relaxation, which were not observed for TiO_2:GeO_2:SiO_2.

Chapter 5

Summary and Outlook

This study investigates the cation interdiffusion between two distinct amorphous oxides after post-annealing, specifically TiO_2 with GeO_2 and with SiO_2. The interdiffusion mechanism occurs within the temperature range of 500°C to 600°C for TiO_2 and GeO_2. Conversely, in the case of TiO_2 and SiO_2, an asymmetry in the diffusion process is observed, with Ti diffusing into the SiO_2 network between 900°C and 1000°C, and Si diffusing into the TiO_2 network between 800°C and 900°C. This finding expands upon previous research, which indicates structural relaxations altering the medium range order at annealing temperatures in the proximity of the reported glass transition temperature (Tg). In amorphous GeO_2 the network organization leads to an increase of the population of large rings at the expense of small rings. In 44% Ti doped GeO_2, a balance between Ge-O-Ti and Ge-O-Ge bonds with minimum Ti-O-Ti bonds. The similarity in the ionic radius of Ti and Ge, make it possible for the restructuring of the atomic network. This is not the case for SiO_2 and TiO_2. The ionic radius of Si in a Si-O bond is smaller than in Ti-O bonds which offers a larger barrier for the diffusion of Ti into SiO_2 as indicated by the higher annealing temperature required. The results of this work offer insights on the behavior of the mixtures of TiO_2:GeO_2 and TiO_2:SiO_2. For TiO_2:GeO_2, the cation interdiffusion enhances the formation of Ti-O-Ge bonds at a temperature that is accessible with the current annealing protocols of TiO_2:GeO_2/SiO_2 coatings. The prevalence of Ti-O-Ge and Ge-O-Ge bonds in annealed TiO_2:GeO_2 is key to reducing mechanical loss in the material. The inability of Ti to diffuse into SiO_2 at 600°C annealing ensures TiO_2 :GeO_2/SiO_2 multilayer stacks will not suffer degradation of their optical properties with annealing due to smearing of the composition at the TiO_2:GeO_2/SiO_2 interfaces.

The results obtained from the ternary materials open new opportunities to design high index layers of TiO_2:GeO_2-based mixtures with very good optical properties, with reduced tensile stress as is the case when adding Si and also higher crystallization temperature. Reduced residual tensile stress in TiO_2:GeO_2:SiO_2 provides flexibility in the design of the high reflector stacks. In work done by our group, it was shown that coating delamination can be prevented if the multilayer stack is compressively stressed after annealing to 600°C for 10 hrs. SiO_2 adds compressive stress, TiO_2:GeO_2 adds tensile stress to the stack. The higher crystallization temperature is advantageous from the standpoint of reducing mechanical loss, as the parameter space to post-anneal the coatings is expanded.

For future research, it would important to measure the mechanical loss specifically for TiO_2:GeO_2:SiO_2 or TiO_2:GeO_2:ZrO_2 after annealing between 700°C and 800°C, for consideration in future-generation gravitational wave detectors. Analysis of the bonding network in the ternary alloys will contribute to the understanding of the structural modifications occurring with the addition of Si or Zr to TiO_2:GeO_2. In particular, it will be very valuable to understand if the addition of a third cation contributes or not to reducing the density of Ti-O-Ti bonds that play a detrimental role in mechanical loss. In addition, obtaining the density and young's modulus which plays a role in thermal noise reduction is also important.

To further explore the minimization of mechanical loss in TiO_2:GeO_2 (44%Ti), it would be valuable to investigate high-temperature deposition, given recent findings on a more ordered structure deposited at high temperatures, which resulted in a 44% reduction of room temperature mechanical loss for GeO_2. [34]

Bibliography

[1] D. Yokoyama, “Molecular orientation in small-molecule organic light-emitting diodes,” *J. Mater. Chem.*, vol. 21, no. 48, p. 19187, 2011, doi: 10.1039/c1jm13417e.

[2] G. W. Shim, W. Hong, J. Cha, J. H. Park, K. J. Lee, and S. Choi, “TFT Channel Materials for Display Applications: From Amorphous Silicon to Transition Metal Dichalcogenides,” *Advanced Materials*, vol. 32, no. 35, p. 1907166, Sep. 2020, doi: 10.1002/adma.201907166.

[3] A. Miller, “An Overview of Optical Waveguide Coatings,” in *Fiber Optics*, B. Bendow and S. S. Mitra, Eds., Boston, MA: Springer US, 1979, pp. 77–103. doi: 10.1007/978-1-4684-3492-7_4.

[4] J. C. Dyre, P. Maass, B. Roling, and D. L. Sidebottom, “Fundamental questions relating to ion conduction in disordered solids,” *Rep. Prog. Phys.*, vol. 72, no. 4, p. 046501, Apr. 2009, doi: 10.1088/0034 4885/72/4/046501.

[5] G. S. Rohrer *et al.*, “Challenges in Ceramic Science: A Report from the Workshop on Emerging Research Areas in Ceramic Science,” *J. Am. Ceram. Soc.*, vol. 95, no. 12, pp. 3699–3712, Dec. 2012, doi: 10.1111/jace.12033.

[6] S. R. Elliott, “Medium-range structural order in covalent amorphous solids,” *Nature*, vol. 354, no. 6353, pp. 445–452, Dec. 1991, doi: 10.1038/354445a0.

[7] K.-H. Sun, “FUNDAMENTAL CONDITION OF GLASS FORMATION,” *J American Ceramic Society*, vol. 30, no. 9, pp. 277–281, Sep. 1947, doi: 10.1111/j.1151-2916.1947.tb19654.x.

[8] Y. Onodera *et al.*, “Origin of the mixed alkali effect in silicate glass,” *NPG Asia Mater*, vol. 11, no. 1, p. 75, Dec. 2019, doi: 10.1038/s41427-019-0180-4.

[9] W. H. Zachariasen, “THE ATOMIC ARRANGEMENT IN GLASS,” *J. Am. Chem. Soc.*, vol. 54, no. 10, pp. 3841–3851, Oct. 1932, doi: 10.1021/ja01349a006.

[10] S. V. King, “Ring Configurations in a Random Network Model of Vitreous Silica,” *Nature*, vol. 213, no. 5081, pp. 1112–1113, Mar. 1967, doi: 10.1038/2131112a0.

[11] D. J. Durben and G. H. Wolf, “Raman spectroscopic study of the pressure-induced coordination change in GeO 2 glass,” *Phys. Rev. B*, vol. 43, no. 3, pp. 2355–2363, Jan. 1991, doi: 10.1103/PhysRevB.43.2355.

[12] S. Kohara and K. Suzuya, “Intermediate-range order in vitreous SiO_2 and GeO_2,” *J. Phys.: Condens. Matter*, vol. 17, no. 5, pp. S77–S86, Feb. 2005, doi: 10.1088/0953-8984/17/5/009.

[13] B. Walker, C. C. Dharmawardhana, N. Dari, P. Rulis, and W.-Y. Ching, “Electronic structure and optical properties of amorphous GeO2 in comparison to amorphous SiO2,” *Journal of Non-Crystalline Solids*, vol. 428, pp. 176–183, Nov. 2015, doi:

10.1016/j.jnoncrysol.2015.08.018.

[14] D. A. Keen and M. T. Dove, “Local structures of amorphous and crystalline phases of silica, SiO_2, by neutron total scattering,” *J. Phys.: Condens. Matter*, vol. 11, no. 47, pp. 9263–9273, Nov. 1999, doi: 10.1088/0953-8984/11/47/311.

[15] M. A. Fazio, G. Vajente, L. Yang, A. Ananyeva, and C. S. Menoni, “Comprehensive study of amorphous metal oxide and Ta 2 O 5 -based mixed oxide coatings for gravitational-wave detectors,” *Phys. Rev. D*, vol. 105, no. 10, p. 102008, May 2022, doi: 10.1103/PhysRevD.105.102008.

[16] C. Rodriguez-Tinoco, M. Gonzalez-Silveira, M. A. Ramos, and J. Rodriguez-Viejo, “Ultrastable glasses: new perspectives for an old problem,” *Riv. Nuovo Cim.*, vol. 45, no. 5, pp. 325–406, May 2022, doi: 10.1007/s40766-022-00029-y.

[17] M. Bass, G. Li, and E. W. Van Stryland, *Handbook of optics*, 3rd ed. New York: McGraw- Hill,2010.

[18] S. R. Elliott, “Electronic Structures of Amorphous Solids,” in *Defects and Disorder in Crystalline and Amorphous Solids*, C. R. A. Catlow, Ed., Dordrecht: Springer Netherlands, 1994, pp. 245–260. doi: 10.1007/978-94-011-1942-9_11.

[19] K. Morigaki and C. Ogihara, “Amorphous Semiconductors: Structure, Optical, and Electrical Properties,” in *Springer Handbook of Electronic and Photonic Materials*, S. Kasap and P. Capper, Eds., Boston, MA: Springer US, 2006, pp. 565–580. doi: 10.1007/978-0-387-29185-7_25.

[20] B. Karmakar, Ed., *Glass nanocomposites: synthesis, properties and applications*. Amsterdam: Elsevier, 2016.

[21] G. Abadias *et al.*, “Review Article: Stress in thin films and coatings: Current status, challenges, and prospects,” *Journal of Vacuum Science & Technology A: Vacuum, Surfaces, and Films*, vol. 36, no. 2, p. 020801, Mar. 2018, doi: 10.1116/1.5011790.

[22] H.-C. Chen, C.-Y. Huang, and P.-W. Cheng, “Stress mechanisms of SiO2 and Nb2O5 thin films sputtered on flexible substrates investigated by finite element method,” *Surface and Coatings Technology*, vol. 344, pp. 449–457, Jun. 2018, doi: 10.1016/j.surfcoat.2018.03.051.

[23] R. Zallen, *The Physics of Amorphous Solids*, 1st ed. Wiley, 1998. doi: 10.1002/9783527617968.

[24] M. D. Ediger, “Perspective: Highly stable vapor-deposited glasses,” *The Journal of Chemical Physics*, vol. 147, no. 21, p. 210901, Dec. 2017, doi: 10.1063/1.5006265.

[25] S. M. Rossnagel, “Thin film deposition with physical vapor deposition and related technologies,” *Journal of Vacuum Science & Technology A: Vacuum, Surfaces, and Films*, vol. 21, no. 5, pp. S74–S87, Sep. 2003, doi: 10.1116/1.1600450.

[26] S. S. Dalal and M. D. Ediger, “Molecular Orientation in Stable Glasses of Indomethacin,” *J. Phys. Chem. Lett.*, vol. 3, no. 10, pp. 1229–1233, May 2012, doi: 10.1021/jz3003266.

[27] S. F. Swallen *et al.*, “Organic Glasses with Exceptional Thermodynamic and Kinetic Stability,” *Science*, vol. 315, no. 5810, pp. 353–356, Jan. 2007, doi: 10.1126/science.1135795.

[28] L. Yang *et al.*, “Modifications of ion beam sputtered tantala thin films by secondary argon and oxygen bombardment,” *Appl. Opt.*, vol. 59, no. 5, p. A150, Feb. 2020, doi: 10.1364/AO.59.00A150.

[29] A. Davenport, E. Randel, and C. S. Menoni, “Ultra-low stress SiO_2 coatings by ion beam sputtering deposition,” *Appl. Opt.*, vol. 59, no. 7, p. 1871, Mar. 2020, doi: 10.1364/AO.380844.

[30] G. Vajente *et al.*, “Low Mechanical Loss TiO 2 : GeO 2 Coatings for Reduced Thermal Noise in Gravitational Wave Interferometers,” *Phys. Rev. Lett.*, vol. 127, no. 7, p. 071101, Aug. 2021, doi: 10.1103/PhysRevLett.127.071101.

[31] Q. Sun, D. M. Miskovic, K. Laws, H. Kong, X. Geng, and M. Ferry, “Transition towards ultrastable metallic glasses in Zr-based thin films,” *Applied Surface Science*, vol. 533, p. 147453, Dec. 2020, doi: 10.1016/j.apsusc.2020.147453.

[32] P. Luo *et al.*, “Ultrastable metallic glasses formed on cold substrates,” *Nat Commun*, vol. 9, no. 1, p. 1389, Apr. 2018, doi: 10.1038/s41467-018-03656-4.

[33] D. R. Queen, X. Liu, J. Karel, H. C. Jacks, T. H. Metcalf, and F. Hellman, “Two-level systems in evaporated amorphous silicon,” *Journal of Non-Crystalline Solids*, vol. 426, pp. 19–24, Oct. 2015, doi: 10.1016/j.jnoncrysol.2015.06.020.

[34] L. Yang *et al.*, “Enhanced medium-range order in vapor-deposited germania glasses at elevated temperatures,” *Sci. Adv.*, vol. 7, no. 37, p. eabh1117, Sep. 2021, doi: 10.1126/sciadv.abh1117.

[35] M. Abernathy *et al.*, “Exploration of co-sputtered Ta_2O_5–ZrO_2 thin films for gravitational-wave detectors,” *Class. Quantum Grav.*, vol. 38, no. 19, p. 195021, Oct. 2021, doi: 10.1088/1361-6382/ac1b06.

[36] R. Birney *et al.*, “Amorphous Silicon with Extremely Low Absorption: Beating Thermal Noise in Gravitational Astronomy,” *Phys. Rev. Lett.*, vol. 121, no. 19, p. 191101, Nov. 2018, doi: 10.1103/PhysRevLett.121.191101.

[37] H. C. Jacks *et al.*, “Structural tunability and origin of two-level systems in amorphous silicon,” *Phys. Rev. Materials*, vol. 6, no. 4, p. 045604, Apr. 2022, doi: 10.1103/PhysRevMaterials.6.045604.

[38] P. Luo and Z. Fakhraai, “Surface-Mediated Formation of Stable Glasses,” *Annu. Rev. Phys. Chem.*, vol. 74, no. 1, pp. 361–389, Apr. 2023, doi: 10.1146/annurev-

physchem-042018-052708.

[39] G. Parisi and F. Sciortino, “Flying to the bottom,” *Nature Mater*, vol. 12, no. 2, pp. 94–95, Feb. 2013, doi: 10.1038/nmat3540.

[40] Yang. Le “A study of structural organization in amorphous oxide thin films for low mechanical loss mirror coatings in interferometric gravitational wave detectors” Ph.D Dissertation, Dep. Of Chemistry, Colorado State University, Colorado, 2021.

[41] A. Einstein, “Die Grundlage der allgemeinen Relativitätstheorie,” *Annalen der Physik*, vol. 354, no. 7, pp. 769–822, Jan. 1916, doi: 10.1002/andp.19163540702.

[42] É. É. Flanagan and S. A. Hughes, “The basics of gravitational wave theory,” *New J. Phys.*, vol. 7, pp. 204–204, Sep. 2005, doi: 10.1088/1367-2630/7/1/204.

[43] B. C. Barish, “The Science and Detection of Gravitational Waves,” *Braz. J. Phys.*, vol. 32, no. 4, pp. 831 837, Dec. 2002, doi: 10.1590/S0103-97332002000500003.

[44] M. Bailes *et al.*, “Gravitational-wave physics and astronomy in the 2020s and 2030s,” *Nat Rev Phys*, vol. 3, no. 5, pp. 344–366, Apr. 2021, doi: 10.1038/s42254-021-00303-8.

[45] C. Cahillane and G. Mansell, “Review of the Advanced LIGO Gravitational Wave Observatories Leading to Observing Run Four,” *Galaxies*, vol. 10, no. 1, p. 36, Feb. 2022, doi: 10.3390/galaxies10010036.

[46] B. P. Abbott *et al.*, “GW150914: The Advanced LIGO Detectors in the Era of First Discoveries,” *Phys. Rev. Lett.*, vol. 116, no. 13, p. 131103, Mar. 2016, doi: 10.1103/PhysRevLett.116.131103.

[47] G. M. Harry *et al.*, “Titania-doped tantala/silica coatings for gravitational-wave detection,” *Class. Quantum Grav.*, vol. 24, no. 2, pp. 405–415, Jan. 2007, doi: 10.1088/0264-9381/24/2/008.

[48] M. Granata *et al.*, “Mechanical loss in state-of-the-art amorphous optical coatings,” *Phys. Rev. D*, vol. 93, no. 1, p. 012007, Jan. 2016, doi: 10.1103/PhysRevD.93.012007.

[49] S. Papernov *et al.*, “Optical properties of oxygen vacancies in HfO_2 thin films studied by absorption and luminescence spectroscopy,” *Opt. Express*, vol. 26, no. 13, p. 17608, Jun. 2018, doi: 10.1364/OE.26.017608.

[50] H. B. Callen and R. F. Greene, “On a Theorem of Irreversible Thermodynamics,” *Phys. Rev.*, vol. 86, no. 5, pp. 702–710, Jun. 1952, doi: 10.1103/PhysRev.86.702.

[51] H.-H. Lai, H.-C. Cheng, S.-H. Su, C.-M. Lin, and W. Wu, “Evolution of internal friction in low-carbon steel during vibratory stress relief,” *Journal of Materials Research and Technology*, vol. 9, no. 3, pp. 5403–5409, May 2020, doi: 10.1016/j.jmrt.2020.03.066.

[52] G. Vajente *et al.*, “A high throughput instrument to measure mechanical losses in thin film coatings,” *Review of Scientific Instruments*, vol. 88, no. 7, p. 073901, Jul. 2017, doi: 10.1063/1.4990036.

[53] Yu. Levin, “Internal thermal noise in the LIGO test masses: A direct approach,” *Phys. Rev. D*, vol. 57, no. 2, pp. 659–663, Jan. 1998, doi: 10.1103/PhysRevD.57.659.

[54] [1] G. M. Harry, T. P. Bodiya, and R. DeSalvo, Eds., Optical coatings and thermal noise in precision measurement. Cambridge ; New York: Cambridge University Press, 2012.

[55] W. A. Phillips, “Two-level states in glasses,” *Rep. Prog. Phys.*, vol. 50, no. 12, pp. 1657–1708, Dec. 1987, doi: 10.1088/0034-4885/50/12/003.

[56] T. H. Metcalf *et al.*, “Internal friction measurements of low energy excitations in amorphous germanium thin films,” *Journal of Alloys and Compounds*, vol. 856, p. 157616, Mar. 2021, doi: 10.1016/j.jallcom.2020.157616.

[57] A. Ueda *et al.*, “Ultra-High Quality Cavity with 1.5 ppm Loss at 1064 nm,” *OPT REV*, vol. 3, no. 5, pp. 369–372, Sep. 1996, doi: 10.1007/s10043-996-0369-y.

[58] M. Granata *et al.*, “Amorphous optical coatings of present gravitational-wave interferometers*,” *Class. Quantum Grav.*, vol. 37, no. 9, p. 095004, May 2020, doi: 10.1088/1361-6382/ab77e9.

[59] M. A. Fazio *et al.*, “Structure and morphology of low mechanical loss TiO_2-doped Ta_2O_5,” *Opt. Mater. Express*, vol. 10, no. 7, p. 1687, Jul. 2020, doi: 10.1364/OME.395503.

[60] K. Prasai *et al.*, “High Precision Detection of Change in Intermediate Range Order of Amorphous Zirconia-Doped Tantala Thin Films Due to Annealing,” *Phys. Rev. Lett.*, vol. 123, no. 4, p. 045501, Jul. 2019, doi: 10.1103/PhysRevLett.123.045501.

[61] M. J. Hart *et al.*, “Medium range structural order in amorphous tantala spatially resolved with changes to atomic structure by thermal annealing,” *Journal of Non-Crystalline Solids*, vol. 438, pp. 10–17, Apr. 2016, doi: 10.1016/j.jnoncrysol.2016.02.005.

[62] Aaron Davenport, “Investigation of TiO2:GeO2 for High Reflector Stacks.” Nov. 01, 2023. [Online]. Available: https://dcc.ligo.org/LIGO-G2302140

[63] G. I. McGhee *et al.*, “Titania Mixed with Silica: A Low Thermal-Noise Coating Material for Gravitational-Wave Detectors,” *Phys. Rev. Lett.*, vol. 131, no. 17, p. 171401, Oct. 2023, doi: 10.1103/PhysRevLett.131.171401.

[64] Peter Murray, Alex Amato, Stuart Hilll, Jessica Steinlechner, and Iain Martin, “TiO2:SiO2 coatings for reducing thermal noise.” Sep. 14, 2023. [Online]. Available: https://dcc.ligo.org/LIGO-G2301953

[65] C. R. Billman, J. P. Trinastic, D. J. Davis, R. Hamdan, and H.-P. Cheng, "Origin of the second peak in the mechanical loss function of amorphous silica," *Phys. Rev. B*, vol. 95, no. 1, p. 014109, Jan. 2017, doi: 10.1103/PhysRevB.95.014109.

[66] R. Hamdan, J. P. Trinastic, and H. P. Cheng, "Molecular dynamics study of the mechanical loss in amorphous pure and doped silica," *The Journal of Chemical Physics*, vol. 141, no. 5, p. 054501, Aug. 2014, doi: 10.1063/1.4890958.

[67] J. Jiang *et al.*, "Analysis of two-level systems and mechanical loss in amorphous ZrO2-doped Ta2O5 by non-cage-breaking and cage-breaking transitions," *The Journal of Chemical Physics*, vol. 154, no. 17, p. 174502, May 2021, doi: 10.1063/5.0046332.

[68] H.-W. Pan *et al.*, "Thickness-dependent crystallization on thermal anneal for titania/silica nm-layer composites deposited by ion beam sputter method," *Opt. Express*, vol. 22, no. 24, p. 29847, Dec. 2014, doi: 10.1364/OE.22.029847.

[69] L.-C. Kuo, H.-W. Pan, C.-L. Chang, and S. Chao, "Low cryogenic mechanical loss composite silica thin film for low thermal noise dielectric mirror coatings," *Opt. Lett.*, vol. 44, no. 2, p. 247, Jan. 2019, doi: 10.1364/OL.44.000247.

[70] S. Khadka *et al.*, "Cryogenic mechanical loss of amorphous germania and titania-doped germania thin films," *Class. Quantum Grav.*, vol. 40, no. 20, p. 205002, Oct. 2023, doi: 10.1088/1361-6382/acf2dd.

[71] S. D. Penn *et al.*, "Mechanical ringdown studies of large-area substrate-transferred GaAs/AlGaAs crystalline coatings," *J. Opt. Soc. Am. B*, vol. 36, no. 4, p. C15, Apr. 2019, doi: 10.1364/JOSAB.36.000C15.

[72] S. Tanuma, C. J. Powell, and D. R. Penn, "Calculations of electron inelastic mean free paths. V. Data for 14 organic compounds over the 50–2000 eV range," *Surface & Interface Analysis*, vol. 21, no. 3, pp. 165–176, Mar. 1994, doi: 10.1002/sia.740210302.

[73] A. Alexandrovski, M. Fejer, A. Markosian, and R. Route, "Photothermal common-path interferometry(PCI): new developments," presented at the SPIE LASE: Lasers and Applications in Science and Engineering,W. A. Clarkson, N. Hodgson, and R. K. Shori, Eds., San Jose, CA, Feb. 2009, p. 71930D. doi: 10.1117/12.814813.

[74] Erik M. Krous, "Characterization of Scandium Oxide Thin Films for use in interference coatings for high-power lasers operating in the near-infrared.," Colorado State University, Fort Collins, CO, 2010.

[75] E. Jankowska, S. Drobczynski, and C. S. Menoni, "Analysis of surface deformation in thin-film coatings by carrier frequency interferometry," *Appl. Opt.*, vol. 56, no. 4, p. C60, Feb. 2017, doi: 10.1364/AO.56.000C60.

[76] G. F. Harrington and J. Santiso, "Back-to-Basics tutorial: X-ray diffraction of thin films," *J Electroceram*, vol. 47, no. 4, pp. 141–163, Dec. 2021, doi: 10.1007/s10832-

021-00263-6.

[77] J. Klein, L. Kampermann, B. Mockenhaupt, M. Behrens, J. Strunk, and G. Bacher, “Limitations of the Tauc Plot Method,” *Adv Funct Materials*, vol. 33, no. 47, p. 2304523, Nov. 2023, doi: 10.1002/adfm.202304523.

[78] L. B. Freund, J. A. Floro, and E. Chason, “Extensions of the Stoney formula for substrate curvature to configurations with thin substrates or large deformations,” *Applied Physics Letters*, vol. 74, no. 14, pp. 1987–1989, Apr. 1999, doi: 10.1063/1.123722.

(79) S.-P. Jeon, J. S. Heo, I. Kim, Y.-H. Kim, and S. K. Park, “Enhanced Interfacial Integrity of Amorphous Oxide Thin-Film Transistors by Elemental Diffusion of Ternary Oxide Semiconductors,” ACS Appl. Mater. Interfaces, vol. 12, no. 52, pp. 57996–58004, Dec. 2020, doi: 10.1021/acsami.0c16068.

(80) J. W. Na, Y. S. Rim, H. J. Kim, J. H. Lee, S. Hong, and H. J. Kim, “Silicon Cations Intermixed Indium Zinc Oxide Interface for High-Performance Thin-Film Transistors Using a Solution Process,” ACS Appl. Mater. Interfaces, vol. 9, no. 35, pp. 29849–29856, Sep. 2017, doi: 10.1021/acsami.7b06643.

(81) H.-W. Yeon et al., “Cu Diffusion-Driven Dynamic Modulation of the Electrical Properties of Amorphous Oxide Semiconductors,” Adv. Funct. Mater., vol. 27, no. 25, p. 1700336, Jul. 2017, doi: 10.1002/adfm.201700336.

(82) J.-P. Niemelä et al., “Mechanical Properties of Atomic-Layer-Deposited Al 2 O 3 /Y 2 O 3 Nanolaminate Films on Aluminum toward Protective Coatings,” ACS Appl. Nano Mater., vol. 5, no. 5, pp. 6285–6296, May 2022, doi: 10.1021/acsanm.2c00378.

(83) Y. Baek et al., “Al2O3/TiO2 nanolaminate gate dielectric films with enhanced electrical performances for organic field-effect transistors,” Organic Electronics, vol. 28, pp. 139–146, Jan. 2016, doi: 10.1016/j.orgel.2015.10.025.

(84) P. S. Padhi et al., “Process temperature-dependent interface quality and Maxwell–Wagner interfacial polarization in atomic layer deposited Al 2 O 3 /TiO 2 nanolaminates for energy storage applications,” Nanoscale, vol. 15, no. 18, pp. 8337–8355, 2023, doi: 10.1039/D3NR00909B.

(85) Y.-Q. Cao, S.-S. Wang, C. Liu, D. Wu, and A.-D. Li, “Atomic layer deposition of ZnO/TiO2 nanolaminates as ultra-long life anode material for lithium-ion batteries,” Sci Rep, vol. 9, no. 1, p. 11526, Aug. 2019, doi: 10.1038/s41598-019-48088-2.

(86) M. Zhu et al., “Nanolaminate-based design for UV laser mirror coatings,” Light Sci Appl, vol. 9, no. 1, p. 20, Feb. 2020, doi: 10.1038/s41377-020-0257-4.

(87) M. Principe, “Reflective coating optimization for interferometric detectors of gravitational waves,” Opt. Express, vol. 23, no. 9, p. 10938, May 2015, doi: 10.1364/OE.23.010938.

(88) H.-W. Pan et al., “Thickness-dependent crystallization on thermal anneal for titania/silica nm-layer composites deposited by ion beam sputter method,” Opt. Express, vol. 22, no. 24, p. 29847, Dec. 2014, doi: 10.1364/OE.22.029847.

(89) R. Berkowitz, “LIGO optical coatings pose new challenges in materials research,” MRS Bull., vol. 41, no. 10, pp. 719–722, Oct. 2016, doi: 10.1557/mrs.2016.218.

(90) B. P. Abbott et al., “LIGO: the Laser Interferometer Gravitational-Wave Observatory,” Rep. Prog. Phys., vol. 72, no. 7, p. 076901, Jul. 2009, doi: 10.1088/0034-4885/72/7/076901.

(91) K. Prasai, R. Bassiri, H.-P. Cheng, and M. M. Fejer, “Glass transition temperatures of binary oxides from ab initio simulations,” APL Materials, vol. 11, no. 8, p. 081113, Aug. 2023, doi: 10.1063/5.0156863.

(92) D. Barreca, A. Gasparotto, C. Maccato, C. Maragno, and E. Tondello, “TiO2 Thin Films by Chemical Vapor Deposition: An XPS Characterization,” Surface Science Spectra, vol. 14, no. 1, pp. 27–33, Dec. 2007, doi: 10.1116/11.20070902.

(93) M. A. Fazio et al., “Structure and morphology of low mechanical loss TiO 2 -doped Ta 2 O 5,” Opt. Mater. Express, vol. 10, no. 7, p. 1687, Jul. 2020, doi: 10.1364/OME.395503.

(94) L. Yang et al., “Structural Evolution that Affects the Room-Temperature Internal Friction of Binary Oxide Nanolaminates: Implications for Ultrastable Optical Cavities,” ACS Appl. Nano Mater., vol. 3, no. 12, pp. 12308–12313, Dec. 2020, doi: 10.1021/acsanm.0c02798.

(95) L. Zhang, J. Zhang, H. Jiao, G. Bao, Z. Wang, and X. Cheng, “Thickness-dependent surface morphology and crystallization of HfO2 coatings prepared with ion-assisted deposition,” Thin Solid Films, vol. 642, pp. 359–363, Nov. 2017, doi: 10.1016/j.tsf.2017.10.010.

(96) H. Sankur and W. Gunning, “Crystallization and diffusion in composite TiO2-SiO2 thin films,” Journal of Applied Physics, vol. 66, no. 10, pp. 4747–4751, Nov. 1989, doi: 10.1063/1.343784.

(97) J. I. Langford and A. J. C. Wilson, “Scherrer after sixty years: A survey and some new results in the determination of crystallite size,” J Appl Crystallogr, vol. 11, no. 2, pp. 102–113, Apr. 1978, doi: 10.1107/S0021889878012844.

(98) L. Yang et al., “Enhanced medium-range order in vapor-deposited germania glasses at elevated temperatures,” Sci. Adv., vol. 7, no. 37, p. eabh1117, Sep. 2021, doi: 10.1126/sciadv.abh1117.

(99) F. V. Grigoriev, E. V. Katkova, A. V. Sulimov, V. B. Sulimov, and A. V. Tikhonravov, “Annealing of deposited SiO_2 thin films: full-atomistic simulation results,” Opt. Mater. Express, vol. 6, no. 12, p. 3960, Dec. 2016, doi:

10.1364/OME.6.003960.

(100) T. Hirose, K. Saito, and A. J. Ikushima, “Structural relaxation in sputter-deposited silica glass,” Journal of Non-Crystalline Solids, vol. 352, no. 21–22, pp. 2198–2203, Jul. 2006, doi: 10.1016/j.jnoncrysol.2006.02.056.

(101) K. Patel, J. Cottom, M. Bosman, A. J. Kenyon, and A. L. Shluger, “An oxygen vacancy mediated Ag reduction and nucleation mechanism in SiO2 RRAM devices,” Microelectronics Reliability, vol. 98, pp. 144–152, Jul. 2019, doi: 10.1016/j.microrel.2019.05.005.

(102) Z. Wang, T. Du, N. M. Anoop Krishnan, M. M. Smedskjaer, and M. Bauchy, “On the equivalence of vapor-deposited and melt-quenched glasses,” The Journal of Chemical Physics, vol. 152, no. 16, p. 164504, Apr. 2020, doi: 10.1063/5.0006590.

(103) K. G. West et al., “Growth and characterization of vanadium dioxide thin films prepared by reactive-biased target ion beam deposition,” Journal of Vacuum Science & Technology A: Vacuum, Surfaces, and Films, vol. 26, no. 1, pp. 133–139, Jan. 2008, doi: 10.1116/1.2819268.

(104) W.M. Haynes, David R. Lide, and Thomas J. Bruno, Eds., CRC Handbook of Chemistry and Physics, 97th ed.

(105) K. Okada, K. Katsumata, Y. Kameshima, and A. Yasumori, “Effect of Germanium Oxide (GeO 2) Additive on the Anatase-to-Rutile Phase Transition,” Journal of the American Ceramic Society, vol. 85, no. 8, pp. 2078–2082, Aug. 2002, doi: 10.1111/j.1151-2916.2002.tb00407.x.

(106) K. Okada, N. Yamamoto, Y. Kameshima, A. Yasumori, and K. J. D. MacKenzie, “Effect of Silica Additive on the Anatase-to-Rutile Phase Transition,” Journal of the American Ceramic Society, vol. 84, no. 7, pp. 1591–1596, Dec. 2004, doi: 10.1111/j.1151-2916.2001.tb00882.x.

(107) McGhee, G; Spagnuolo, V; Demos, N; Tait, S; Murray P, et.al. Titania mixed with silica: A low thermal-noise coating material for gravitational-wave detectors; LIGO-P2300203-v3. https://dcc.ligo.org/LIGO-P2300203 (accessed 2023-08-01)

(108) G. Vajente et al., “Low Mechanical Loss TiO 2 : GeO 2 Coatings for Reduced Thermal Noise in Gravitational Wave Interferometers,” Phys. Rev. Lett., vol. 127, no. 7, p. 071101, Aug. 2021, doi: 10.1103/PhysRevLett.127.071101.

(109) S. V. King, “Ring Configurations in a Random Network Model of Vitreous Silica,” Nature, vol. 213, no. 5081, pp. 1112–1113, Mar. 1967, doi: 10.1038/2131112a0.

(110) Q. Zhou, Y. Shi, B. Deng, J. Neuefeind, and M. Bauchy, “Experimental method to quantify the ring size distribution in silicate glasses and simulation validation thereof,” Sci. Adv., vol. 7, no. 28, p. eabh1761, Jul. 2021, doi: 10.1126/sciadv.abh1761.

(111) Y. Shi et al., “Revealing the relationship between liquid fragility and medium-range order in silicate glasses,” Nat Commun, vol. 14, no. 1, p. 13, Jan. 2023, doi: 10.1038/s41467-022-35711-6.

(112) Y. Shi, D. Ma, A. P. Song, B. Wheaton, M. Bauchy, and S. R. Elliott, “Structural evolution of fused silica below the glass-transition temperature revealed by in-situ neutron total scattering,” Journal of Non-Crystalline Solids, vol. 528, p. 119760, Jan. 2020, doi: 10.1016/j.jnoncrysol.2019.119760.

(113) A. Malashevich, S. Ismail-Beigi, and E. I. Altman, “Directing the Structure of Two-Dimensional Silica and Silicates,” J. Phys. Chem. C, vol. 120, no. 47, pp. 26770–26781, Dec. 2016, doi: 10.1021/acs.jpcc.6b07008.

(114) Büchner et al., “Adsorption of Au and Pd on Ruthenium-Supported Bilayer Silica,” J. Phys. Chem. C, vol. 118, no. 36, pp. 20959–20969, Sep. 2014, doi: 10.1021/jp5055342.

(115) V. V. Hoang, “The glass transition and thermodynamics of liquid and amorphous TiO 2 nanoparticles,” Nanotechnology, vol. 19, no. 10, p. 105706, Mar. 2008, doi: 10.1088/0957-4484/19/10/105706.

(116) V. V. Hoang, “The glass transition and diffusion in simulated liquid TiO 2,” J. Phys.: Condens. Matter, vol. 19, no. 41, p. 416109, Oct. 2007, doi: 10.1088/0953-8984/19/41/416109.

(117) U. Martinez, L. Giordano, and G. Pacchioni, “Tuning the work function of ultrathin oxide films on metals by adsorption of alkali atoms,” The Journal of Chemical Physics, vol. 128, no. 16, p. 164707, Apr. 2008, doi: 10.1063/1.2905218.

(118) B. P. Abbott *et al.*, “Observation of Gravitational Waves from a Binary Black Hole Merger,” *Phys. Rev. Lett.*, vol. 116, no. 6, p. 061102, Feb. 2016, doi: 10.1103/PhysRevLett.116.061102.

(119) B. P. Abbott *et al.*, “GW170817: Observation of Gravitational Waves from a Binary Neutron Star Inspiral,” *Phys. Rev. Lett.*, vol. 119, no. 16, p. 161101, Oct. 2017, doi: 10.1103/PhysRevLett.119.161101.

(120) É. Lalande *et al.*, “Zirconia-titania-doped tantala optical coatings for low mechanical loss Bragg mirrors,” *Journal of Vacuum Science & Technology A: Vacuum, Surfaces, and Films*, vol. 39, no. 4, p. 043416, Jul. 2021, doi: 10.1116/6.0001074.

(121) Vajente. G, Davenport. A, et.al, AdV+/A+ coating working group call - 2023-11-08” Nov 08, 2023. [Online]. Available: https://dcc.ligo.org/LIGO-G2302177

(122) Randel et.al, “Effects of annealing on residual stress in TiO2:GeO2 mixtures deposited by ion beam sputtering” Jun, 19, 2023. [Online]. Available: https://dcc.ligo.org/LIGO-G2201012

(123) G. Vajente et al., “Low Mechanical Loss TiO 2 : GeO 2 Coatings for Reduced Thermal Noise in Gravitational Wave Interferometers,” Phys. Rev. Lett., vol. 127, no. 7, p. 071101, Aug. 2021, doi: 10.1103/PhysRevLett.127.071101.

(124) J.-Y. Tewg, Y. Kuo, and J. Lu, “Suppression of Crystallization of Tantalum Oxide Thin Film by Doping with Zirconium,” *Electrochem. Solid-State Lett.*, vol. 8, no. 1, p. G27, 2005, doi: 10.1149/1.1836122.

(125) M. Kord, V. K. Marghussian, B. Eftekhari-yekta, and A. Bahrami, “Effect of ZrO2 addition on crystallization behaviour, porosity and chemical–mechanical properties of a CaO–TiO2–P2O5 microporous glass ceramic,” *Materials Research Bulletin*, vol. 44, no. 8, pp. 1670–1675, Aug. 2009, doi: 10.1016/j.materresbull.2009.04.007.

(126) N. Banno *et al.*, “Structural characterization of amorphous Ta2O5 and SiO2–Ta2O5 used as solid electrolyte for nonvolatile switches,” *Applied Physics Letters*, vol. 97, no. 11, p. 113507, Sep. 2010, doi: 10.1063/1.3488830.

(127) R. Kužel, L. Nichtová, Z. Matěj, and J. Musil, “In-situ X-ray diffraction studies of time and thickness dependence of crystallization of amorphous TiO2 thin films and stress evolution,” *Thin Solid Films*, vol. 519, no. 5, pp. 1649–1654, Dec. 2010, doi: 10.1016/j.tsf.2010.08.122.

(128) Q. Dong et al., “Borosilicate-Based Framework: Synthesis, Single-Crystal Structure Study, and Physical Properties,” Inorg. Chem., vol. 63, no. 5, pp. 2663–2669, Feb. 2024, doi: 10.1021/acs.inorgchem.3c03964.

(129) R. Thapa, K. Prasai, R. Bassiri, M. M. Fejer, and D. A. Drabold, “Realistic computer models of amorphous ZrO 2 : Ta 2 O 5 : Structural, optical, and vibrational properties,” Phys. Rev. B, vol. 105, no. 22, p. 224207, Jun. 2022, doi: 10.1103/PhysRevB.105.224207.

(130) D. McClelland, M. Evans, R. Schnabel, B. Lantz, I. Martin, V. Quetschke., “Instrument Science White Paper.” DCC LIGO. [Online]. Available: https://dcc.ligo.org/LIGO-T1400316